

# **Radiative Energy Budget Estimates for the 1979 Southwest Summer Monsoon**

By

Steven A. Ackerman and Stephen K. Cox

Department of Atmospheric Science  
Colorado State University  
Fort Collins, Colorado



**Department of  
Atmospheric Science**

Paper No. 405

Radiative Energy Budget Estimates for the 1979 Southwest Summer Monsoon

by

Steven A. Ackerman

and

Stephen K. Cox

Department of Atmospheric Science

Colorado State University

Fort Collins Co 80523

November, 1986

Atmospheric Science Paper No. 405

## ABSTRACT

Observations of temperature, moisture, cloud amount, cloud height and soil derived aerosols are incorporated into radiative transfer models to yield estimates of the tropospheric and surface radiative energy budgets for the summer monsoon of 1979. Results are presented for six phases of the monsoon for the region  $30^{\circ}\text{S}$  to  $40^{\circ}\text{N}$  latitude and  $30^{\circ}\text{E}$  to  $100^{\circ}\text{E}$  longitude. The derived radiative fields are significantly different from climatological estimates. The evolution of the radiative energy budgets are discussed in relation to monsoon activity. Total tropospheric convergence (TTC) for the January and February phases, exhibits a minimum cooling over the southern Indian Ocean and a maximum tropospheric radiative energy loss over the Arabian Sea and Bay of Bengal. The early May, pre-onset, onset and post-onset periods exhibit cellular patterns in TTC with maximum cooling over the cloud free oceanic regions and minimum cooling associated with continental regions and areas with large amounts of cloud. This cellular structure is still evident when TTC is averaged over  $10^{\circ}$  regions. Large seasonal variations in TTC are observed over the deserts, due to the presence of dust in the summer. Regions with large seasonal variations in cloud cover (e.g. the Arabian Sea) also display large variations in TTC. Regionally averaged radiative heating profiles also change significantly with period. These variations result primarily from changes in the cloud distribution associated with the evolution of the monsoon.

The net surface radiative flux varies markedly from period to period, and within the same period. As expected, all six periods have a maximum surface radiative energy gain for the cloud free oceanic regions; while cloudy and continental regions tend to have relative minima. Large spatial and temporal variations exist in the net surface flux.

#### ACKNOWLEDGEMENTS

This research has been supported by the National Science Foundation under Grant ATM-8418472 and by the National Aeronautics and Space Administration under Grant NAG 1-554. Computer calculations were carried out using the computer facilities at the National Center for Atmospheric Research, which is supported by the National Science Foundation. We also extend our thanks to Ms. M. Tucker who assisted in the preparation of the manuscript.

## TABLE OF CONTENTS

	<u>PAGE</u>
ABSTRACT	ii
ACKNOWLEDGEMENTS	iii
TAELE OF CONTENTS	iv
LIST OF TABLES	v
LIST OF FIGURES	vi
1. INTRODUCTION	1
2. METHODOLOGY	3
2.1 Radiation calculation algorithms	4
2.2 Fields of state parameters	7
2.3 Cloud radiative properties	7
2.4 Aerosol radiative properties	21
2.5 Cloud distributions	23
2.6 Aerosol distribution	27
2.7 Spatial and temporal resolution of the radiative energy budgets	32
3. RESULTS	33
3.1 Radiative energy budgets	41
4. SUMMARY	82
5. REFERENCES	84
APPENDIX	A-1
A.1 Cloud cover analysis of TIROS-N AVHRR data	A-3
A.2 Cloud cover analysis of GOES-1 VISSR data	A-9
A.3 Summary	A-18
LIST OF APPENDIX FIGURES	A-21

LIST OF TABLES

	<u>PAGE</u>
TABLE 1. Periods of Radiative Energy Budget Estimates	39
TABLE 2. Coefficient of Variation for the Latitudinal Mean TTC	53
TABLE 3. Coefficient of Variation for the Longitudinal Mean TTC	53
TABLE 4. Net surface radiative energy budget for four geographic regions; Empty Quarter (20°N to 25°N and 45°E to 50°E); northern Arabian Sea (20°N to 25°N and 60°E to 65°E); central India (20°N to 25°N and 75°E to 70°E); and northern Bay of Bengal (15°N to 20°N and 85°E to 90°E). Units are $W m^{-2}$ . Values in parenthesis are the total cloud cover in percent.	82

## LIST OF FIGURES

	<u>PAGE</u>
Figure 1. Geographic region of study. Also shown are surface type based on the atlas of Edlin and Huxley (1973).	2
Figure 2a. Comparison between the present LW radiation model flux calculations with aircraft observations and model results from the higher spectral resolution models of Wiscombe and Smith.	5
Figure 2b. Comparison between the present SW radiation model flux calculations with aircraft observations and model results from the higher spectral resolution models of Wiscombe and Smith.	6
Figure 3. Measurements of cloud water content as a function of pressure. The thick dashed line depicts the relationship between assumed cloud water content and cloud top pressure.	9
Figure 4. Cloud emittance as a function of cloud water path for various parameterizations shown in the legend.	11
Figure 5a. The downward, upward and net ( $F_N$ ) longwave fluxes for an atmosphere containing an ice cloud. Results for two cloud radiative parameterizations are shown.	13
Figure 5b. The downward, upward and net ( $F_N$ ) longwave fluxes for an atmosphere containing a low level water cloud. Results for two cloud radiative parameterizations are shown.	14
Figure 6. Daily total SW energy absorbed by a 1 km thick cloud as a function of cloud top height for a zero surface albedo. Results from three different parameterization schemes are shown.	15
Figure 7. Cloud shortwave absorptance as a function of ice water path for a solar zenith angle of $0^\circ$ . The circles represent single calculations given by Welch et al. (1980), while the thick solid line represents a fit to their data. Results from parameterizations given by Stephens (1978b) and Liou and Wittman (1979) are also shown.	17
Figure 8.* Absorptance of a 460 m thick atmospheric layer as a function of cloud cover; the cloud was assumed to be 460 m thick and solar zenith angle of $0^\circ$ . The solid line represents the layer absorptance assuming the radiative properties of an infinite cloud, while the dashed line assumes those of a non-interacting cubic cloud. The circles represent layer absorptance assuming a 460 m thick cloud whose horizontal dimensions correspond to the appropriate cloud cover.	20

	<u>PAGE</u>
Figure 9. Intercomparison of GOES-1 VISSR and TIROS-N AVHRR derived 1°x1° mean temperatures at coincident time periods.	24
Figure 10. Satellite cloud top IR temperature correction as a function of total precipitable water above cloud top.	26
Figure 11a. Percent occurrence (see legend) of surface based observations that noted the suspension of dust in the atmosphere for the month of June 1979. Observations were averaged over a 1° grid.	28
Figure 11b. Mean surface estimated visibility (km) associated with the dust outbreaks of figure 11.	29
Figure 12. Number of days in which an observation of suspended dust was made as a function of month for the year 1979 for several stations in the southwest monsoon region. Also shown (heavy line) are the number of dust days in which the visibility was less than 5 km. The dashed line includes dust days and days with haze observations. Tic marks on the ordinate represent 10 day increments while those along the abscissa represent the months of January, April, August and December.	31
Figure 13. Total cloud cover derived from the GOES-1 (G), TIROS-N (T) and surface (solid line with +) observations for four different stations for June 1979. Present weather surface observations are depicted in the bottom of each figure.	34
Figure 14a. Monthly mean percent clear regions for June 1979 as derived from surface observations (dashed line) and the GOES-1 observations (solid line).	36
Figure 14b. Monthly mean percent clear regions for June 1979 as derived from surface observations (dashed line) and the TIROS-N satellite (solid line).	36
Figure 15. Comparison of the percent of high clouds (cloud tops < 400 mb) derived from the GOES-1 (solid line) and TIROS-N (dashed line) for the month of June 1979. Contour intervals are 25% coverage.	37
Figure 16. Comparison of total cloud amount for the month of June 1979 averaged over four geographic regions as derived by the GOES-1 (G), TIROS-N (thick line) and surface (thin line) analysis.	38
Figure 17. Comparison of high cloud amount for the month of June 1979 averaged over four geographic regions as derived by the GOES-1 (G) and TIROS-N (thick line) analysis.	40

- Figure 18. Comparison of the present results (solid lines) with the results of Dopplnick (1979) (dashed lines). Top: comparison of the Dopplnick December-February profiles with the mean of the January and February phases of the present study. Bottom: comparison of Dopplnick June-August results with the pre-onset, onset and post-onset mean of the present study Units of the radiative heating are °C/Day. 42
- Figure 19. Zonal cross-sections of radiative heating (°C/Day) for the equator (a) and 20°N (b). The results for the January case of Katayama (1967) are given as dashed lines, while the solid lines depict the results for the average of the January and February phases of the present study. 44
- Figure 20. The 24 hour mean total tropospheric convergence in  $W m^{-2}$  for the six phases of the 1979 monsoon. Regions of missing data are denoted with M. Contour interval is  $20 W m^{-2}$  45-50
- Figure 21. The 24 hour mean total tropospheric convergence in  $W m^{-2}$  for the Pre-onset phase with the different panels representing different spacial scales as indicated. 55
- Figure 22. Latitudinal mean (averaged over 5° longitude) total tropospheric convergence for the six periods. 56
- Figure 23. Vertically integrated radiative differential heating fields for the six periods, for the region 0° to 30°N and 30°E to 100°E. Units are  $W m^{-2} km^{-1}$ . 58-63
- Figure 24. Radiative heating profiles averaged over a 5° latitude by 5° longitude region for four areas; a) northwest Arabian Sea (25°N 60°E to 20°N 65°E), b) eastern Arabian Sea (15°N 70°E to 10°N 75°E), c) central India (25°N 75°E to 20°N 80°E) and d) northwest Bay of Bengal (20°N 85°E to 15°N 90°E). 65
- Figure 25. Regionally averaged cloud top pressure profiles for the four phases discussed in the text. The regions are; a) northwest Arabian Sea (25°N 60°E to 20°N 65°E), b) eastern Arabian Sea (15°N 70°E to 10°N 75°E), c) central India (25°N 75°E to 20°N 80°E) and d) northwest Bay of Bengal (20°N 85°E to 15°N 90°E). The periods are Early May (dotted line); Pre-onset (dash-dot line); onset (solid line); and Post-onset (dashed line). Values in parenthesis are the percentage of cloud free areas. 66

- Figure 26. Zonal cross-section of tropospheric radiative convergence along the latitude band  $10^{\circ}$ - $15^{\circ}$  N (left hand panels) for the a) pre-onset, b) onset and c) post-onset phases respectively. The right hand panels display a similar cross-section of the vertical distribution of cloud top pressure. 68-70
- Figure 27. Surface net radiative flux for the six phases of the 1979 summer monsoon. Contour intervals are  $50 \text{ Wm}^{-2}$  with positive values representing a net surface gain. 75-80

## 1. INTRODUCTION

A monsoon is generally defined as the seasonal reversal of a circulation system and is driven by a contrast in the thermal properties of adjacent surfaces, radiative and moist processes. The southwest monsoon is certainly one of the more spectacular monsoons of the globe. The summer monsoon experiment (SMONEX) was conducted over the Indian Ocean and adjacent land areas from May-August 1979. This time period overlapped with the second special observation period of the First GARP Global Experiment (FGGE). A combination of SMONEX and FGGE observations provides an unprecedented data set for the study of the southwest summer monsoon. The evolution of the monsoon is, to a large extent, an atmospheric response to a differential heating field; thus a primary goal of SMONEX was to identify the heat sources and sinks associated with the southwest summer monsoon (Fein and Kuettnner, 1980). This study presents estimates of two components of the diabatic fields; the tropospheric and surface radiative energy budgets. These budgets were derived from a variety of observations in conjunction with radiative transfer calculations. Due to the large impact of clouds on the radiative energy budgets (as well as other diabatic heating fields), vertical and horizontal distributions of cloud top are presented in the Appendix.

Diabatic heating fields span many space and time scales, from planetary to local and from seasonal to diurnal. Different studies will inevitably require different temporal and spatial scales of the diabatic heating fields. In an attempt to derive a useable data set, as well as an accurate one, radiative energy budgets were derived for the region  $30^{\circ}\text{S}$  to  $40^{\circ}\text{N}$  latitude and  $30^{\circ}\text{E}$  to  $100^{\circ}\text{E}$  longitude at a spatial resolution of  $1^{\circ}$  (figure 1), and a vertical resolution of 100 mb. Based on the work of Krishnamurti and Ramanathan

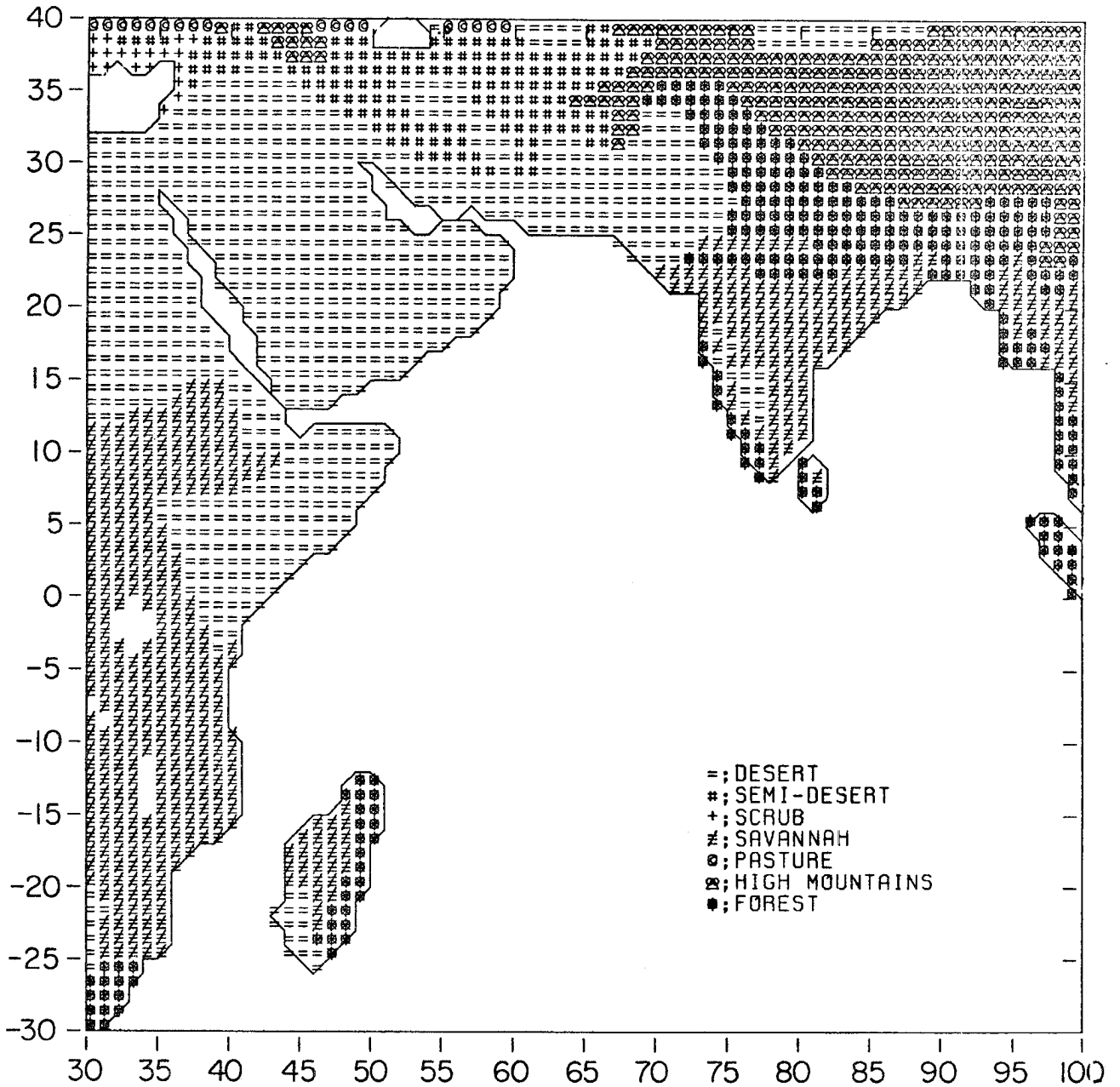


Figure 1. Geographic region of study. Also shown are surface type based on the atlas of Edlin and Huxley (1973).

(1982), six 10-day periods were chosen that represent the various stages of the monsoon of 1979.

Section 2 describes the data and analysis methods used in estimating the radiative energy budgets. Section 3 discusses the spatial and temporal variations of the derived radiative energy budgets during the various stages of monsoon development. Results of the study are summarized in section 4.

## 2. METHODOLOGY

The tropospheric radiative convergence profiles were derived in a manner analogous to the one employed by Cox and Griffith (1979). This methodology combines data representing the vertical and horizontal distributions of temperature, moisture, carbon dioxide, ozone, clouds and soil derived aerosols with radiative transfer calculations to yield estimates of the radiative divergence in the atmosphere. The surface radiative fluxes were determined in a similar manner, and are thus consistent with the radiative heating profiles. While it is difficult to quantitatively assess the accuracy of the derived radiative budgets, an estimation of the quality can be conveniently broken down into four components:

- i. Radiation calculation algorithms,
- ii. Fields of state parameters used as input to calculation algorithms,
- iii. Cloud and aerosol radiative properties used in the calculations,
- iv. Cloud and aerosol distributions.

In the discussion which follows, each of these components will be considered to illustrate the quality of the radiative budget fields.

## 2.1 Radiation calculation algorithms

The longwave (LW) radiative divergence profiles were computed using an integrated broadband emissivity model similar to Cox and Griffith (1979). The model has six spectral bands for the gaseous components of the atmosphere and one band for the treatment of clouds. An example of a comparison among the present model calculation, aircraft observations and results from the higher spectral resolution models of Wiscombe and of Smith (Smith et al., 1980) is shown in figure 2a. Aircraft radiative flux observations, as well as temperature and moisture profiles were collected as part of a SMONEX research flight conducted on 18 May 1979, over the eastern Arabian Sea. A stratocumulus cloud field with 1/8-2/8 areal coverage was present during the flight however the model calculations assumed cloud free conditions. The broadband model results are in excellent agreement with the spectral models as well as with the observed fluxes. Absolute differences are generally less than 3%.

The shortwave (SW) radiative convergence profiles were calculated using the broadband integrated absorptivity model of Cox and Griffith (1979). The model has one band for each of the three gases; water vapor, carbon dioxide and ozone. The fractional absorption data were taken from Manabe and Wetherald (1967). The treatment of non-gaseous atmospheric constituents are discussed in sections 2.3 and 2.4. A comparison of the downward irradiances computed using the broadband model with higher resolution spectral models and observations taken on 18 May 1979, is shown in figure 2b. Again, the broadband model compares well, with absolute errors less than 2%.

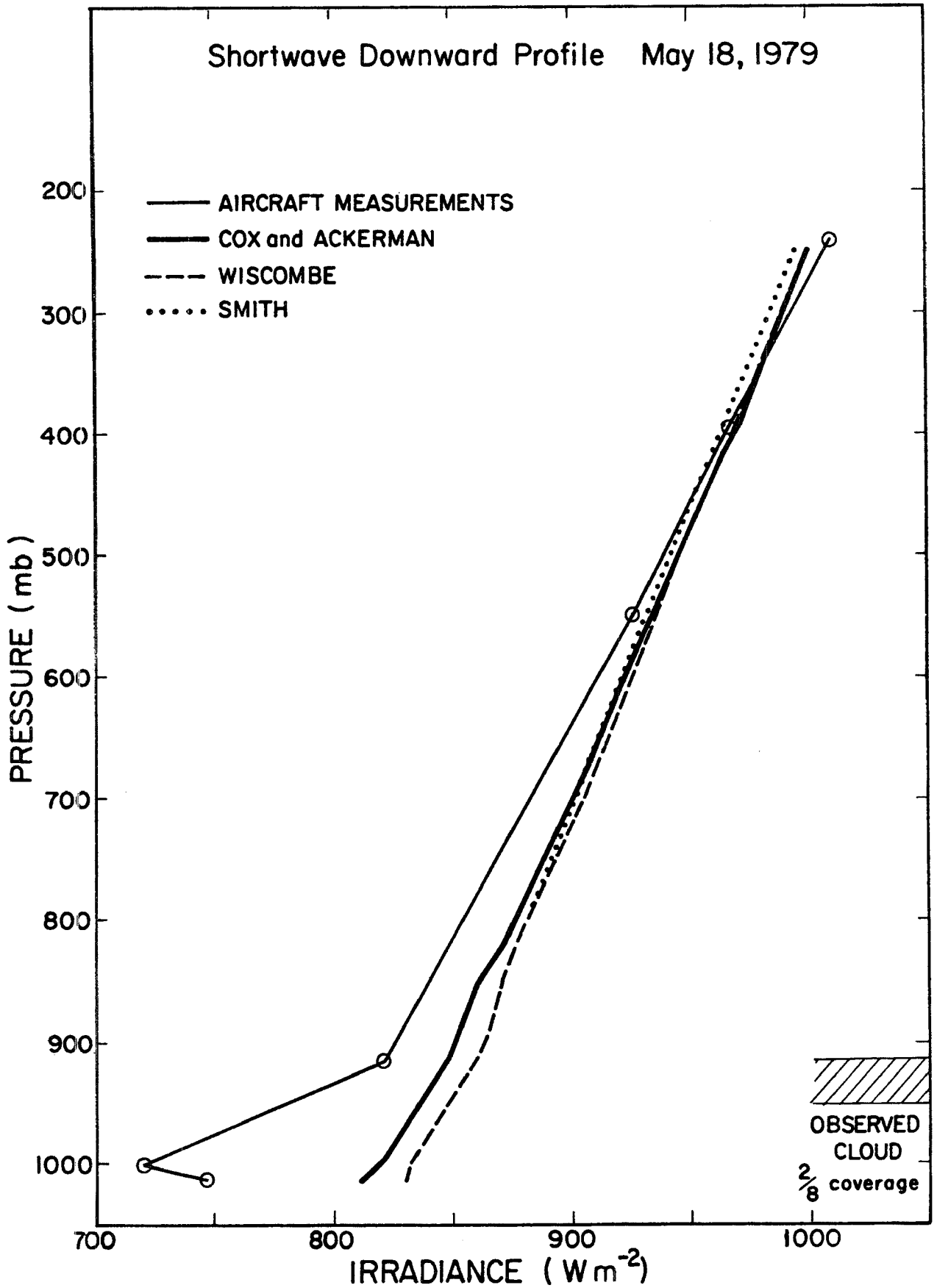


Figure 2a. Comparison between the present LW radiation model flux calculations with aircraft observations and model results from the higher spectral resolution models of Wiscombe and Smith.

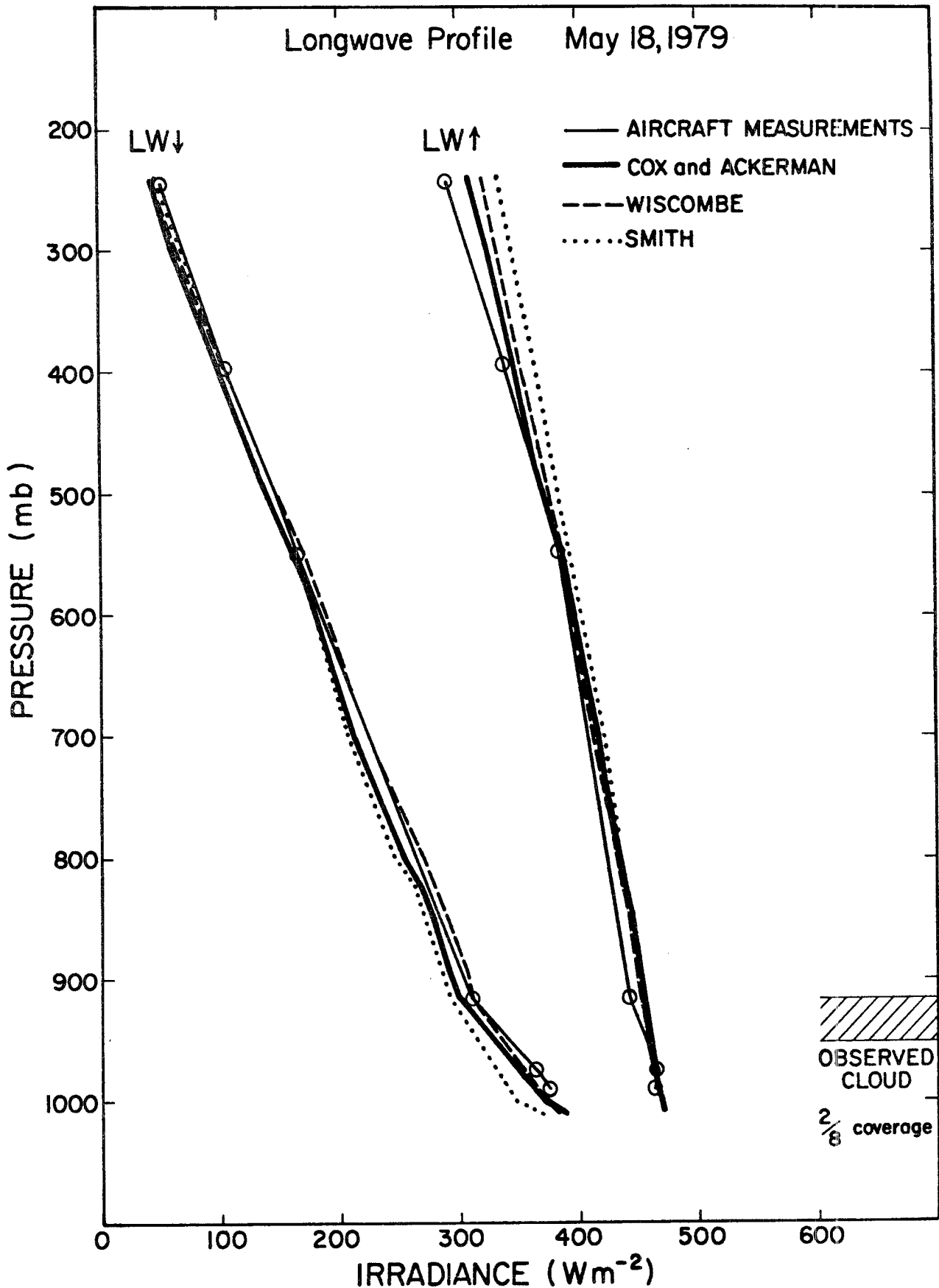


Figure 2b. Comparison between the present SW radiation model flux calculations with aircraft observations and model results from the higher spectral resolution models of Wiscombe and Smith.

## 2.2 Fields of state parameters

The FGGE level IIIb data set (Kaneshige,1980) was used in compositing atmospheric temperature and water vapor mixing ratios. Mean temperature and moisture values were determined for a 5° latitude by 5° longitude grid; separate composites for land, ocean and Himalaya subregions were computed for each grid. The ozone profiles of Doplick (1972) were used in the present study along with a constant carbon dioxide mixing ratio of .486 g/Kg.

Surface temperatures for the region were estimated from satellite observations using the neighbor-to-neighbor technique discussed by Cox et al. (1986)<sup>1</sup>. Mean daytime and nighttime surface temperatures were composited and used as input to the radiative transfer models. In the case of a cloudy atmosphere, the daily mean surface temperature was used. Surface albedoes were assigned based on the surface type (see figure 1) and the observations of Rockwood and Cox (1978), Mathews (1983) as well as SMONEX aircraft observations (Smith et al., 1980).

## 2.3 Cloud radiative properties

Clouds are the most important modulators of the earth's energy budget and, for this reason, it is important that they be parameterized as accurately as possible. The parameterization of the radiative properties of clouds was limited by the computation time required for deriving the energy budgets of such a large region as well as the uncertainties in assigning representative cloud macrophysical and microphysical properties. The following parameterization schemes were developed with these limitations in mind and are the best that our current knowledge can support.

The radiative characteristics of clouds are often represented as a function of cloud liquid (ice) water content (e.g. Stephens 1978b, Liou and

Wittman, 1979, Griffith et al., 1980 and Chylek and Ramaswamy 1982), such an approach was taken in the present study. Measurements of the water contents of various clouds penetrated during SMONEX are shown in figure 3, along with several other data sets, as indicated in the legend. As expected, there is a wide variability in cloud water content. Similarly, one would expect variations in particle size distributions and concentrations. These variations not only exist from cloud to cloud, but are often evident within a given cloud. Since there is no feasible way to determine cloud properties of specific systems as a function of time and space over the entire MONEX domain, mean cloud water contents were assigned for the radiation calculations. The relationship between cloud water content and cloud top pressure adopted in the present study is depicted by the thick dashed line in figure 3.

Measurements of the infrared (IR) radiative properties of water clouds (e.g. Platt 1972, 1976; and Platridge 1974) indicate that the cloud emissivity is primarily determined by the cloud liquid water content. In a theoretical study, Stephens (1978a) found the IR cooling within water clouds to depend primarily on the liquid water content (LWC) and its vertical distribution, and was more or less independent of the drop size distribution. Stephens (1978b) then went on to parameterize cloud emissivity in terms of the cloud liquid water path (LWP =  $\int_{Z_B}^{Z_T} \text{LWC} dz$ );

$$\epsilon = 1 - a \exp(-b \text{LWP}) \quad (1)$$

This simple parameterization scheme is in good agreement with the experimental values of emissivity in the 10-12  $\mu\text{m}$  spectral interval (Stephens et al., 1978) which is the largest contributor to the total emissivity (Stephens, 1978b). A similar formulation was used by Chylek and Ramaswamy (1982) for approximating the flux emissivity of water clouds in the 8-11.5  $\mu\text{m}$  band. For

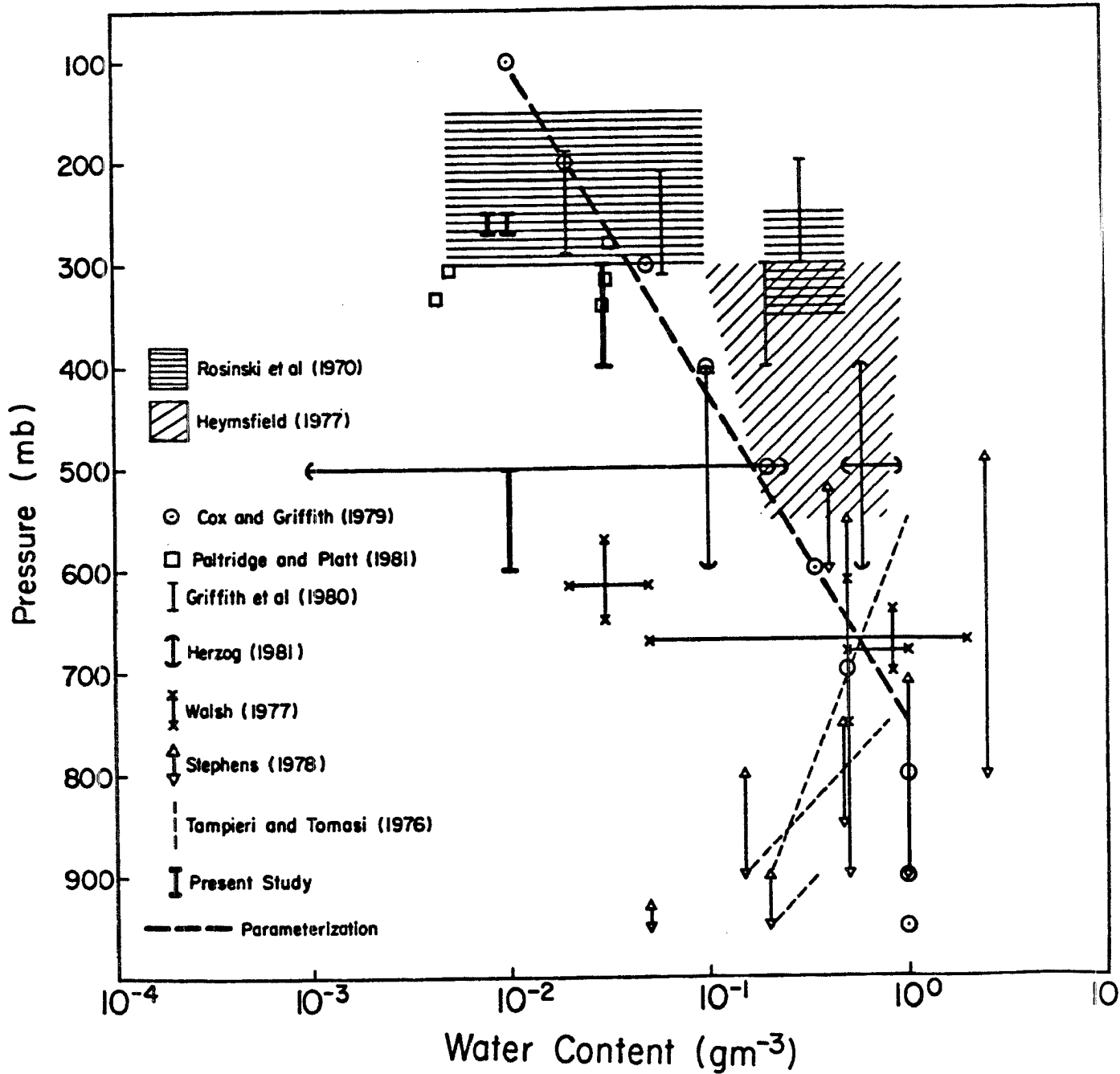


Figure 3. Measurements of cloud water content as a function of pressure. The thick dashed line depicts the relationship between assumed cloud water content and cloud top pressure.

wavelengths  $\lambda > 11.5 \mu\text{m}$ , Chylek and Ramaswamy (1982) found that the broad-band flux emissivity was also dependent on the drop size distribution. Using equation (1), Chylek and Ramaswamy (1982) parameterized the 8-14  $\mu\text{m}$  flux emissivity for three typical cloud droplet size distributions.

The work of Platt (1976), Griffith et al. (1980) and Paltridge and Platt (1981) suggest that the emissivity of ice clouds may be parameterized similar to the water cloud parameterization discussed above, with  $a=1$  and  $b$  (mass absorption coefficient) ranging from 0.05 to  $0.096 \text{ m}^{-2} \text{ g}^{-1}$ . Liou and Wittman (1979) parameterized the reflectance, transmittance and emittance of a cirrus cloud, whose ice water content (IWC) ranged from 5.2 -  $150.4 \text{ g m}^{-2}$ , using a polynomial expression.

Cloud emittance as a function of water path are shown in figure 4 for the various parameterizations discussed above. The parameterization of Stephens (1978b) includes several different size distributions representative of various water cloud types; while the results of Chylek and Ramaswamy (1982) and Liou and Wittman (1979) depend on the drop size distribution. The results of Griffith et al. (1980) and Paltridge and Platt (1981) were based on measurements in ice clouds. Figure 5a depicts the downward, upward and net longwave fluxes for an atmosphere containing an ice cloud with an IWC of  $0.01 \text{ gm}^{-3}$ ; results using both the Stephens (1978b) and Griffith et al. (1980) parameterizations are shown. Differences between the two parameterizations may be attributed to 1) the different incident fluxes at the cloud boundaries and 2) the implicit inclusion of a water vapor content typical of water clouds in the Stephens (1978b) parameterization; while Griffith et al. (1980) attempt to isolate the emissivity of the cloud from the gaseous constituents in the atmosphere. Using these same parameterizations, the downward, upward and net longwave fluxes for an atmosphere containing a water cloud were

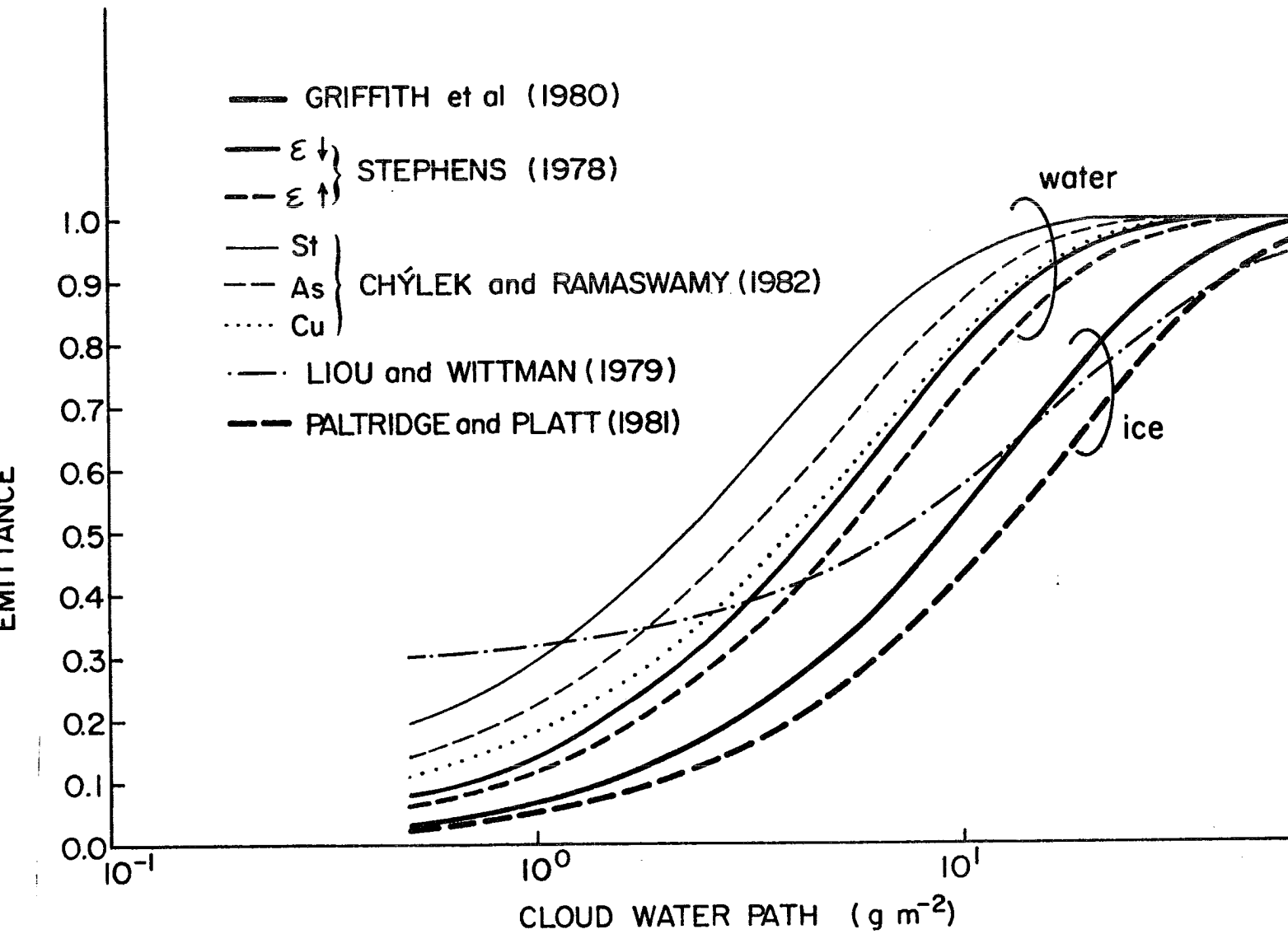


Figure 4. Cloud emittance as a function of cloud water path for various parameterizations shown in the legend.

calculated and are shown in figure 5b. The differences between the two schemes are small, as suggested by Griffith et al. (1980). Considering our lack of knowledge of the cloud droplet size distributions, as well as the similarity between the parameterization schemes of Griffith et al. (1980) and Stephens (1978) for water clouds, the results of Griffith et al. (1980) were adopted for both water and ice clouds.

The SW radiative properties of a cloud are a function of the cloud water content, particle size distribution, depth into cloud, cloud shape, cloud top height, solar zenith angle as well as surface albedo. In a study of the shortwave radiative properties of water clouds, Stephens (1978a) found the shortwave fractional absorptance to be primarily a function of the LWP. The relationship between cloud radiative properties and drop size distribution are discussed in Ackerman and Stephens (1986). Stephens (1978b) and Stephens et al. (1984) incorporated several typical cloud drop size distributions to parameterize the SW radiative properties of water clouds as a function of the LWP, solar zenith angle and the underlying surface albedo. In a similar study, Liou and Wittman (1979) parameterized the SW radiative properties of four different cloud types (low cloud, middle cloud, high cloud and stratus) as a function of solar zenith angle, LWP and surface albedo. A comparison of these two schemes is shown in figure 6, which gives the daily total energy absorbed by a 1 km thick cloud as a function of cloud top height for a zero surface albedo. The open squares were derived from the results of Liou and Wittman (1979) for the four different cloud types presented in their study. The solid squares depict the results of the Stephens et al. (1984) parameterization where the clouds were assigned the corresponding water contents given by Liou and Wittman (1979). The discrepancies are large. Since the parameterization scheme of Stephens et al. (1984) incorporates

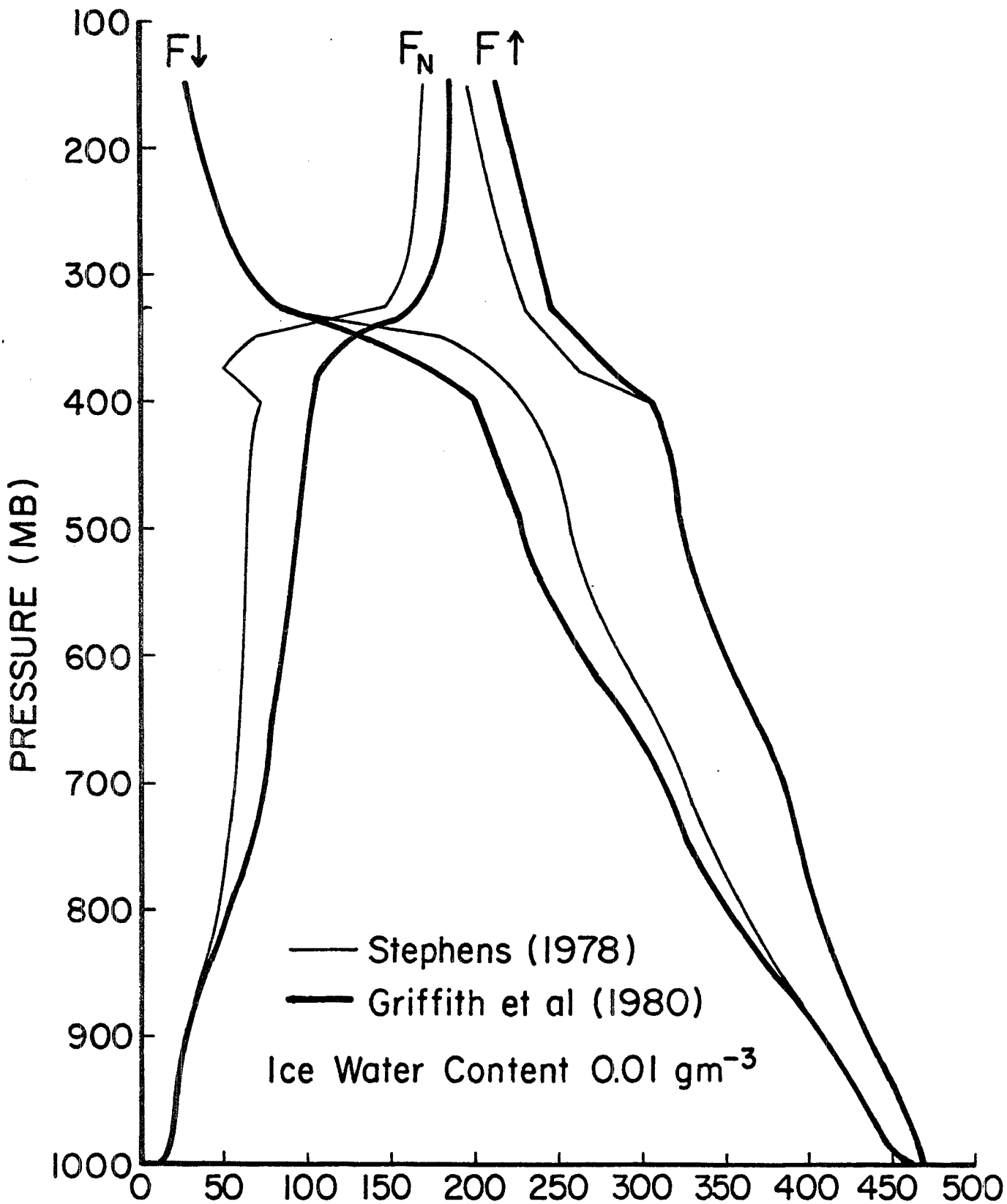


Figure 5a. The downward, upward and net ( $F_N$ ) longwave fluxes for an atmosphere containing an ice cloud. Results for two cloud radiative parameterizations are shown.

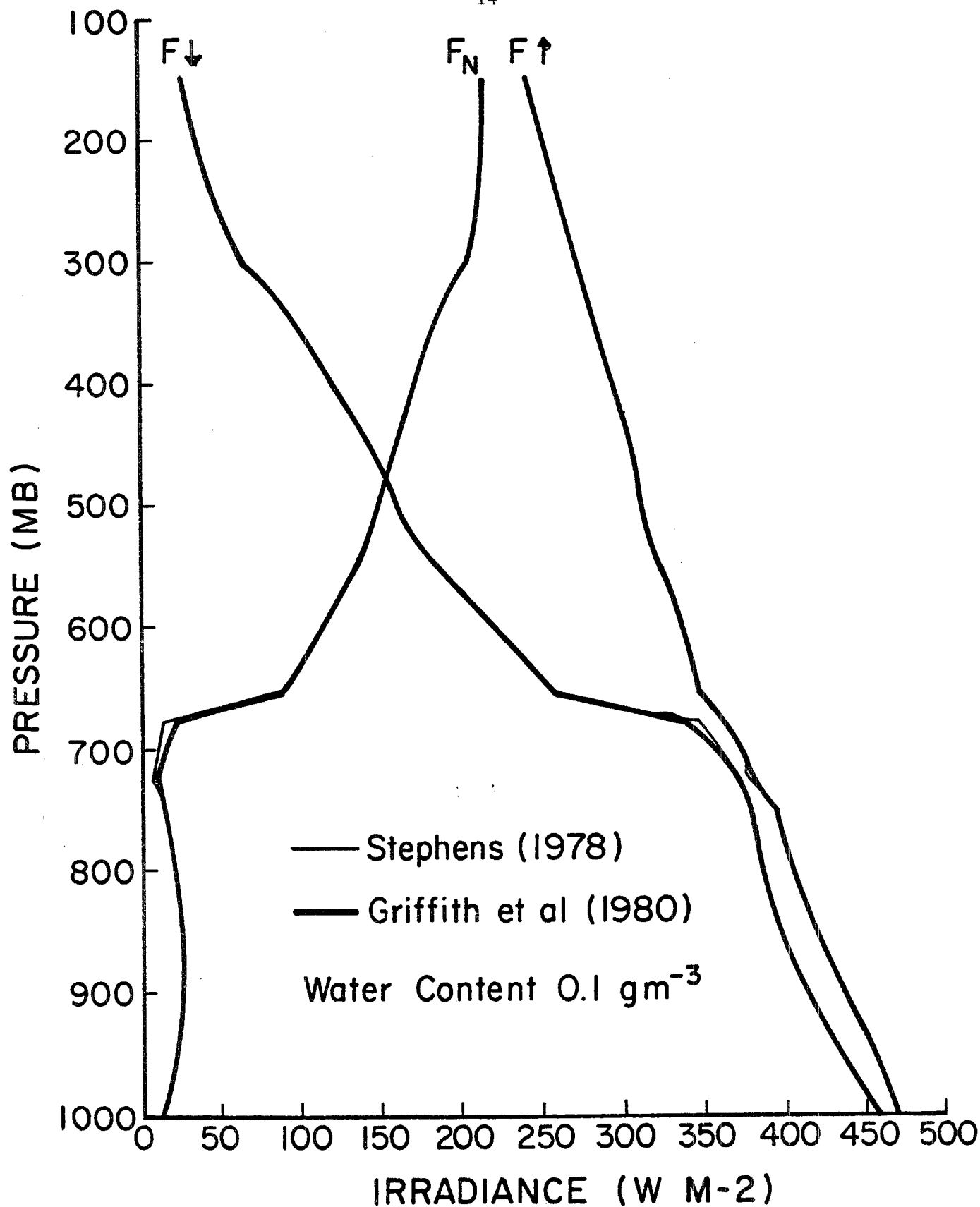


Figure 5b. The downward, upward and net ( $F_N$ ) longwave fluxes for an atmosphere containing a low level water cloud. Results for two cloud radiative parameterizations are shown.

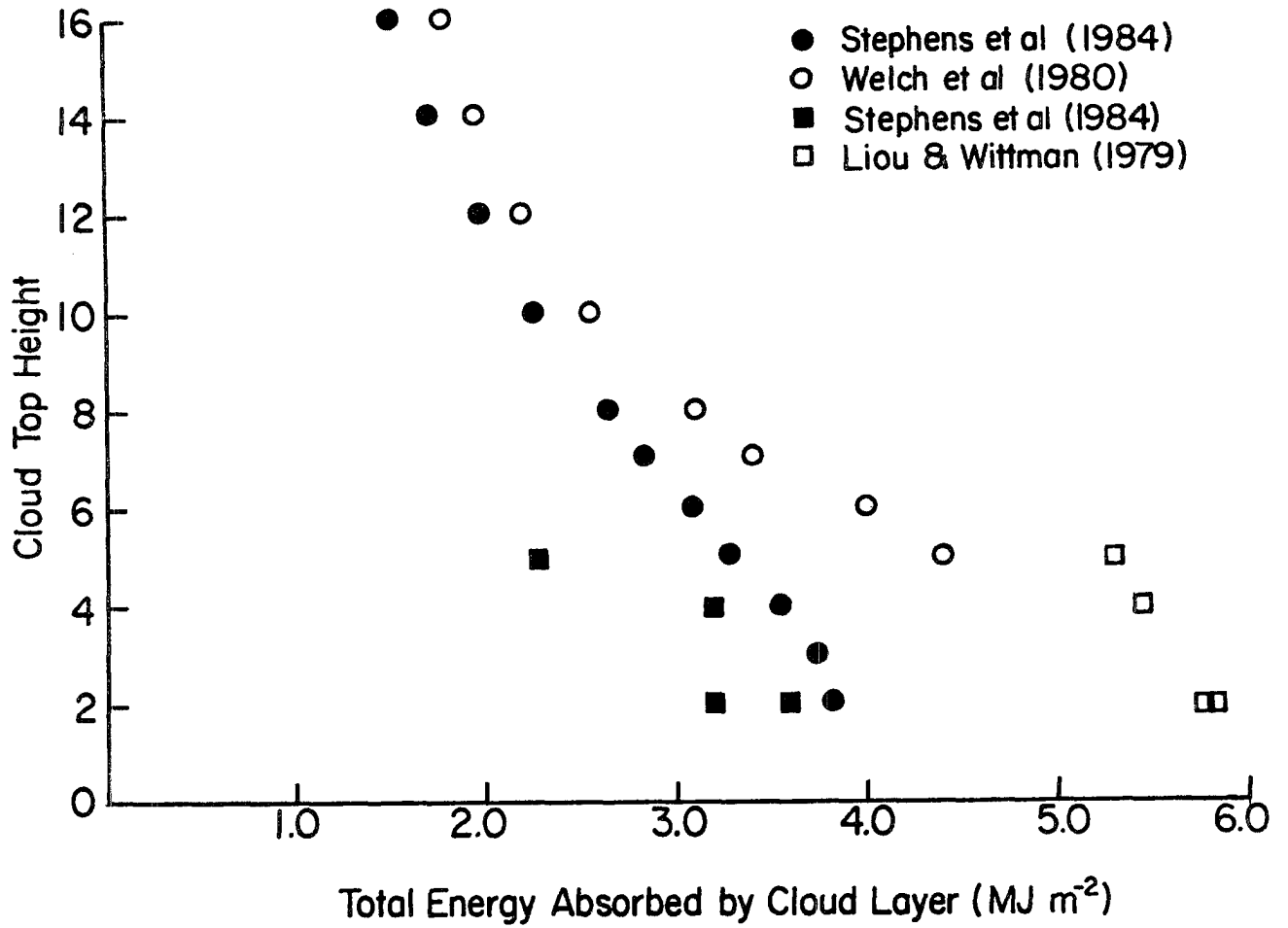


Figure 6. Daily total SW energy absorbed by a 1 km thick cloud as a function of cloud top height for a zero surface albedo. Results from three different parameterization schemes are shown.

several drop size distributions, it was adopted for specifying the SW radiative properties of extended water clouds.

Welch et al. (1980b) conclude that detailed knowledge of ice crystal concentration, size and shape are not necessary to estimate the bulk SW radiative characteristics of an ice cloud. Welch et al. (1980b) indicate that broadband reflectance, transmittance and absorptance of an ice cloud can be reasonably estimated given the cloud optical depth. In addition, the calculations of Welch et al. (1980a) show that water and ice have similar radiative characteristics, and that cloud radiative characteristics are primarily determined by the particle concentration and size distribution, with the phase of the water playing a secondary role.

From calculations tabulated in Welch et al. (1980a), a relationship was derived expressing cloud absorptance as a function of IWP, for a solar zenith angle ( $\theta$ ) of  $0^\circ$  (figure 7). The open circles in figure 7 indicate a single calculation, while the solid thick line is a least square fit to the data. Also shown (thick dashed line) is the relationship between absorptance and LWP for  $\theta = 0^\circ$ , given by Stephens et al. (1984). For water paths less than  $100 \text{ gm}^{-2}$  there is little difference between the ice and water cloud parameterization. In the case of large water paths, there is considerable difference between the two parameterizations; however, these differences are largely due to the different size distributions used in the two studies. Stephens et al. (1984), used monomodal drop size distributions with most drops having a radius less than  $20 \text{ }\mu\text{m}$ . The large IWP derived from the Welch et al. (1980) data include large monomodal and bimodal drop size distributions. Bimodal and large particle size distributions increase the absorption of optically thick ice and water clouds, explaining the differences in the absorption values at large water paths. For comparative purposes, the

relationship between absorptance and water path for  $\theta = 0^\circ$  derived by Liou and Wittman (1979) for two cloud types is also shown in figure 7.

Figure 6 also depicts the daily total energy convergence of a 1 km thick cloud as a function of cloud top height. The solid circles result from the Stephens et al. (1984) parameterization where the clouds were assigned water contents according to figure 3. The open circles depict results of an ice water parameterization based on the Welch et al. (1980a) data, where again the clouds were assigned water contents according to figure 3. After considering the variations in cloud water content (figure 3); variations in particle size distributions and concentrations; the similar radiative characteristics of ice and water (Welch et al. 1980a); and the small differences in the water and ice parameterization of the daily energy convergence of high clouds (figure 6), the parameterization scheme developed by Stephens et al. (1984) was used to represent the radiative properties of extended clouds, irrespective of the phase of the water.

The above SW parameterizations are applicable to homogeneous, extended clouds. The work of Welch et al. (1980a) suggest that the bulk radiative properties of heterogeneous, extended clouds may be determined from the average microphysical cloud properties. Their work also indicates that for a finite cloud with a width to thickness ratio of approximately 120, less than one percent of the incident energy exits the sides of the cloud, and the absorptance of the cloud approaches that of an infinite cloud. In the case of "cubic" clouds, Davis et al. (1979) have shown that absorption of solar energy by finite clouds may be more or less than semi-infinite clouds, depending on the solar zenith angle. The radiative characteristics of finite clouds was intensively investigated by Welch et al. (1980a). Studies by several authors, [e.g. McKee and Cox (1974, 1976), Davis (1978), Aida

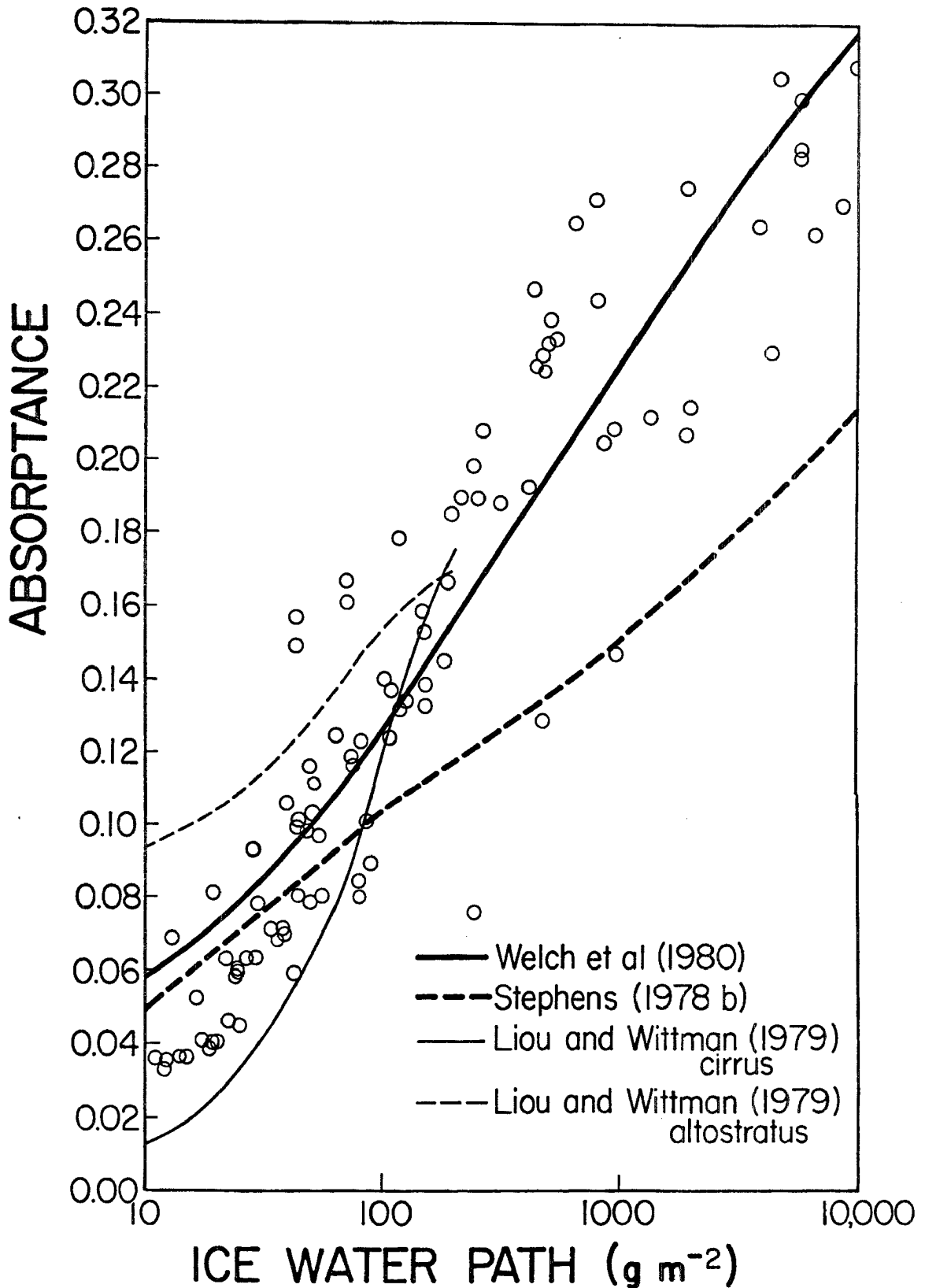


Figure 7. Cloud shortwave absorptance as a function of ice water path for a solar zenith angle of  $0^\circ$ . The circles represent single calculations given by Welch et al. (1980), while the thick solid line represents a fit to their data. Results from parameterizations given by Stephens (1978b) and Liou and Wittman (1979) are also shown.

(1977), Davis et al., (1979a,b), Welch et al. (1980a) and Newiger and Bahnke (1981)] indicate important differences between individual finite clouds and their plane parallel counterparts. Welch and Zdunkowski (1981a,b) present a simple parameterization for non-interacting "cubic" cumulus cloud fields. The effect of a cloud's shape on its radiative characteristics was also discussed by Welch and Zdunkowski (1981c).

Figure 8 depicts the absorptance of a 460 m thick atmospheric layer as a function of cloud cover; the cloud was assumed to be 460 m thick with a solar zenith angle of 0°. The layer absorptance was determined from

$$ABS = (1-F) * CLR_A + F * CLD_A \quad (2)$$

where

ABS = layer absorptance

F = percent cloud cover

CLR<sub>A</sub> = layer absorptance of the clear region

CLD<sub>A</sub> = layer absorptance of the cloud.

The solid line in figure 8 represents the layer absorptance assuming the radiative properties of an infinite cloud, while the dashed line assumes those of a non-interacting cubic cloud; thus one may consider these lines to be limits on the layer absorptance. Although differences in the absorption of an infinite versus finite cloud may be large, these differences are reduced when area weighted with the clear regions. For example, a non-interacting layer field can have a maximum cloud cover of approximately 25%, which, for this case, results in an infinite-finite cloud absorptance difference of less than 1%. Cloud cover greater than 25% results in cloud-cloud interaction such that the finite cloud case should approach that of the infinite case as the cloud cover approaches 100%. The circles represent layer absorptance assuming a

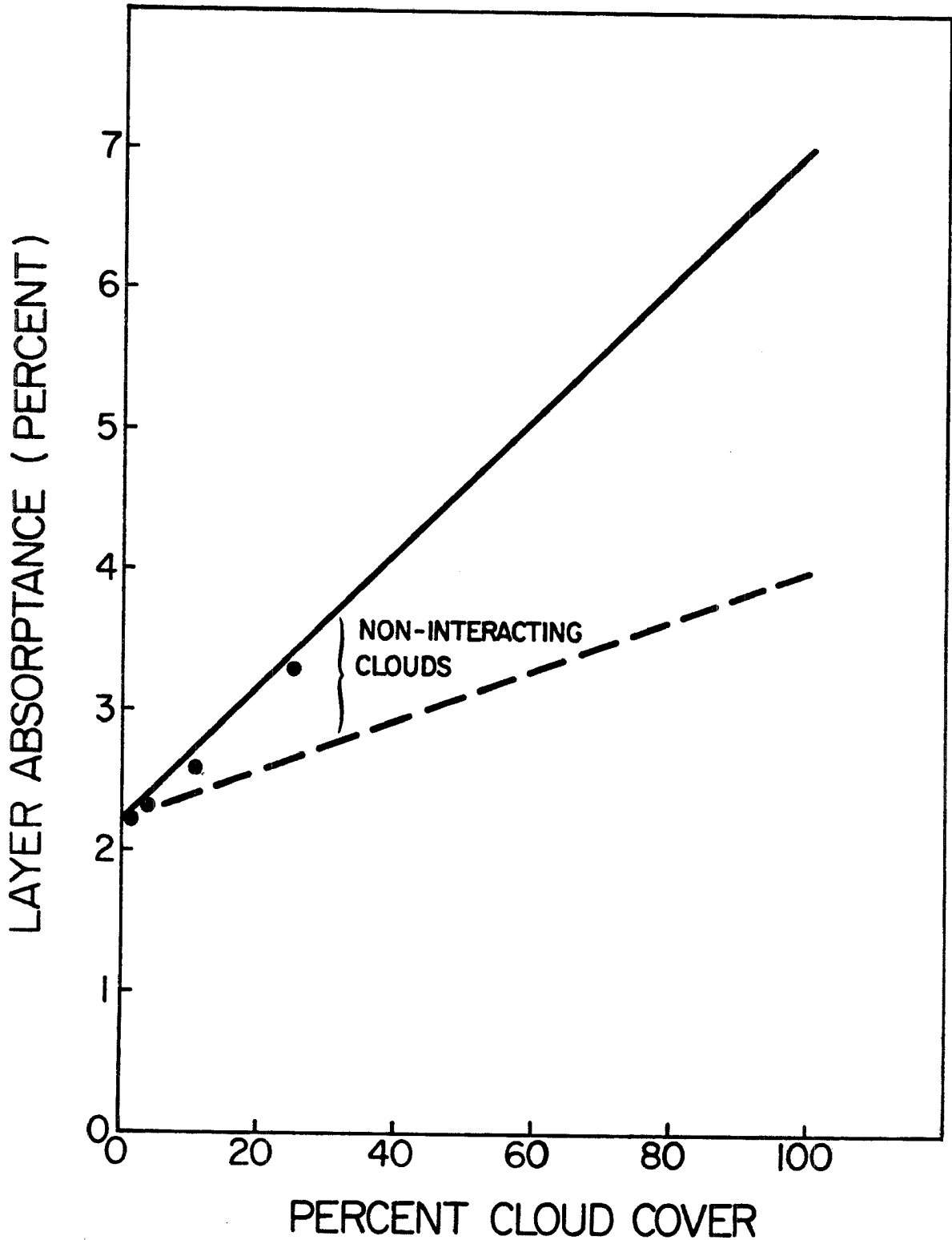


Figure 8. Absorptance of a 460 m thick atmospheric layer as a function of cloud cover; the cloud was assumed to be 460 m thick and solar zenith angle of  $0^\circ$ . The solid line represents the layer absorptance assuming the radiative properties of an infinite cloud, while the dashed line assumes those of a non-interacting cubic cloud. The circles represent layer absorptance assuming a 460 m thick cloud whose horizontal dimensions correspond to the appropriate cloud cover.

460 m thick cloud whose horizontal dimensions correspond to the appropriate cloud cover, indicating that cloudy regions composed of extended layered clouds are well represented by assuming the radiative properties of the infinite cloud. Considering our lack of knowledge of individual cloud microphysical and macrophysical properties, non-interacting fair weather cumulus type cloud fields are also well represented by assuming the bulk radiative properties of an infinite cloud. The finite effects of specific clouds have thus been neglected in determining bulk cloud absorptance. While infinite-finite difference in cloud reflectance maybe large, the resulting effect on the atmospheric absorptance above cloud is small (Davis et al. 1979). Absorptance below a cloud base was assumed to be zero.

#### 2.4 Aerosol Radiative Properties

Ackerman and Cox (1982) have shown that the dust over the Saudi Arabian peninsula and the adjacent Arabian Sea plays a significant role in determining the radiative energy budget of these regions. By comparing calculations for a dust free atmosphere with in-situ broadband radiative measurements, Ackerman and Cox (1982) inferred the broadband shortwave radiative characteristics of the dust. They parameterized the fractional absorptance of the dust in terms of the dust mass loading as

$$FA_D = A_0 + A_1 \ln[u + \exp(-A_0/A_1)] \quad (3)$$

where;

$FA_D$  = fractional absorptance of the dust

$u$  =  $\sec \theta \int M dz$

$M$  = dust mass loading ( $g m^{-3}$ )

$dz$  = depth into the dust layer

$\theta$  = solar zenith angle

$A_0$  = 0.02

$A_1$  = 0.039

This parameterization is similar to assigning the dust layer a broadband single scattering albedo ( $\omega_0$ ) of 0.96 (Patterson et al., 1983). This value is in agreement with the results of Fouquart et al. (1983), where 60% of the observed broadband  $\omega_0$  were between 0.94 and 0.96. However, this value is somewhat larger than the  $\omega_0$  inferred by Patterson et al. (1983). They estimated a value of  $\omega_0$  between 0.8 and 0.9, thus predicting considerably more absorption of solar radiation. The above parameterization was incorporated into the broadband shortwave radiative transfer model of the present study.

The results of Ackerman and Cox (1982) indicated that the dust had no detectable effect on the longwave radiative fluxes. This is consistent with the findings of Ellingson and Serafino (1984). Measurements by DeLuisi et al. (1976) suggest that the IR cooling is inhibited in a desert atmosphere, though they could not directly determine the effects of the aerosol. The calculations of Carlson and Benjamin (1980) indicate a LW cooling at the top of the dust layer for both their desert and ocean models, with a low level warming for the ocean case. The net effect of the dust layer on the atmospheric radiative heating rates was positive for both their ocean and desert cases, resulting in a net profile similar to Ackerman and Cox (1982). There is some disagreement in the literature with regards to the effects of soil derived aerosols on the LW fluxes; we assume that the effects are small, in agreement with the aircraft measurements made during SMONEX (Ackerman and Cox, 1982 and Ellingson and Serafino, 1984)

## 2.5 Cloud distributions

Accurate estimates of the horizontal and vertical distributions of clouds are essential for the determination of the radiation energy budgets. Cloud top pressure distributions for each  $1^\circ \times 1^\circ$  region were determined using a method analogous to that employed by Cox and Griffith (1979). The technique is basically a threshold method employing  $11\mu\text{m}$  satellite observations. The adequacy of this technique has been discussed previously [Cox and Griffith (1979), Ackerman and Cox (1981), Minnis and Harrison (1984) and Rossow et al. (1985)] and is explored further in the following section. The Visible-Infrared Spin Scan Radiometer (VISSR) onboard the geostationary satellite GOES-1 which was positioned at approximately  $57^\circ$  E longitude during FGGE provided the satellite data set. The visible ( $.5\text{-}.85\mu\text{m}$ ) and IR ( $10.0\text{-}12.5\mu\text{m}$ ) channels were used to determine the cloud top distributions. The data were mapped by Smith (1984) and covered a the region  $30^\circ\text{S}\text{-}40^\circ\text{N}$  latitude and  $30^\circ\text{E}$  to  $100^\circ\text{E}$  longitude (figure 1). Eight time periods per day were used to estimate diurnal fluctuations (2, 5, 8, 11, 14, 17, 20 and 23 GMT). There were problems with the GOES-1 VISSR IR sensor during 1979 so that a consistent day to day evolution of the southwest summer monsoon was unavailable. The transformation of the VISSR IR raw counts to equivalent blackbody temperatures was accomplished using the standard National Environmental Satellite Service (NESS) lookup table. Since no checks were made to update the GOES-1 calibration table, a re-calibration of the GOES-1 IR sensor was made by comparing  $1^\circ \times 1^\circ$  mean temperature from the GOES-1 with the TIROS-N Advanced Very High Resolution Radiometer (AVHRR) derived temperatures at coincident time periods. The results are shown in figure 9 along with a least squares fit to the data. The major discrepancy was at the

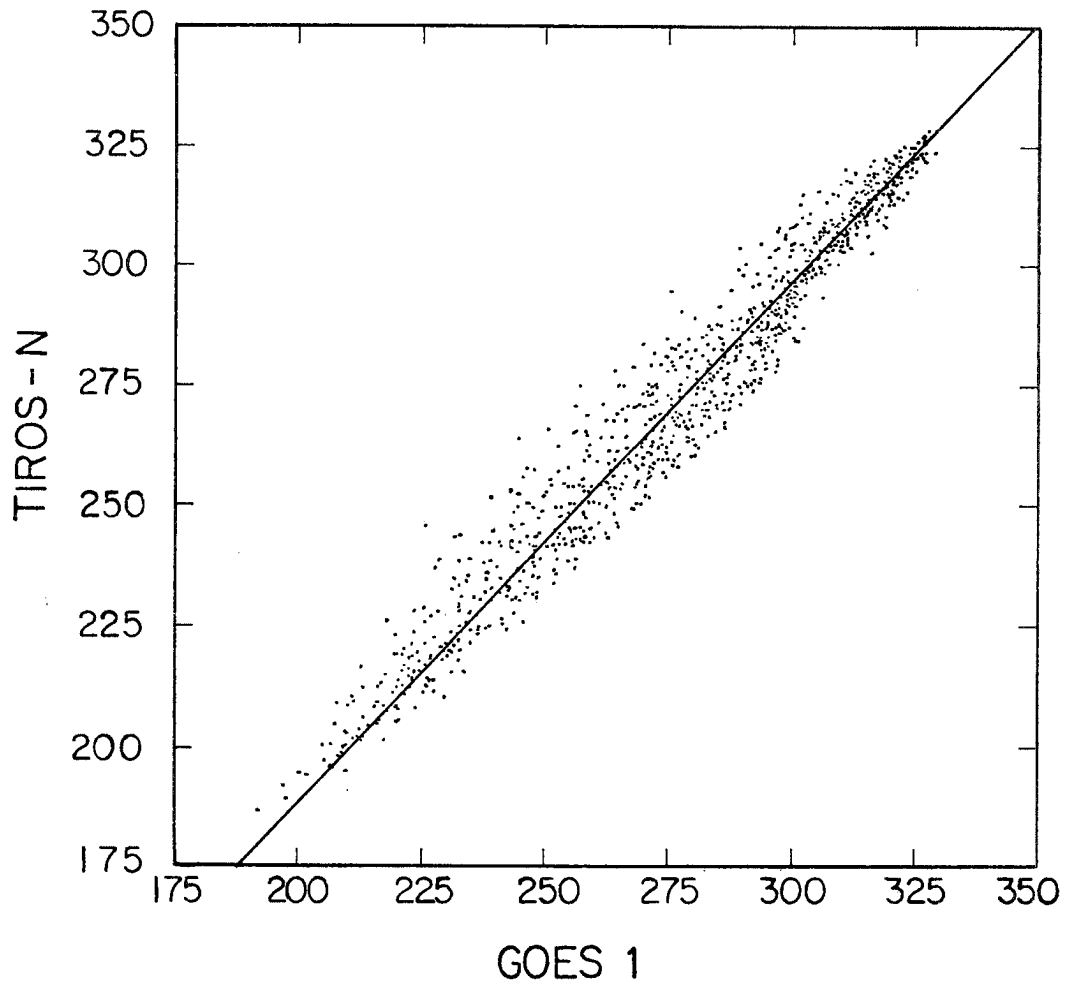


Figure 9. Intercomparison of GOES-1 VISSR and TIROS-N AVHRR derived  $1^{\circ} \times 1^{\circ}$  mean temperatures at coincident time periods.

colder temperature where the GOES-1 was several degrees warmer. There is excellent agreement at the higher temperatures.

Two corrections were applied to the satellite derived apparent cloud top temperature (Cox and Griffith, 1979). The first correction accounts for water vapor emission in the window channel of the satellite detector. This correction term was represented as a function of the precipitable water above cloud top determined from FGGE IIIB moisture profiles. Figure 10 depicts this temperature correction where the circles depict calculations using various FGGE IIIB temperature and moisture profiles and the solid line is the function used in this study. The second correction accounts for the penetration distance into the cloud before radiative blackness is achieved, and is a function of cloud water content and the mass absorption coefficient. Cloud water content was assigned according to figure 3 along with a mass absorption coefficient of  $0.045 \text{ m g}^{-1}$ . The penetration distance was then converted to a temperature correction using the lapse rate of the given region. Once the cloud top temperature is determined, cloud top pressure is located using the temperature profile of the appropriate region. Satellite measurements in the visible were used to tune the clear sky IR threshold over the ocean in a manner similar to that used by Cox and Griffith (1979).

For the computation of the SW profiles, cloud tops were assigned to 50 mb layers, cloud thickness was assumed to be 100 mb, and absorption below cloud base was assumed to be negligible. In the case of the LW radiative profiles, clouds were assumed to be either thin or thick. Thin clouds were assumed to have their bases in the same 100 mb layer as the cloud top. The bases of the thick clouds were assigned a pressure level corresponding to the approximate lifted condensation level (LCL) of the given subregion. The distribution of

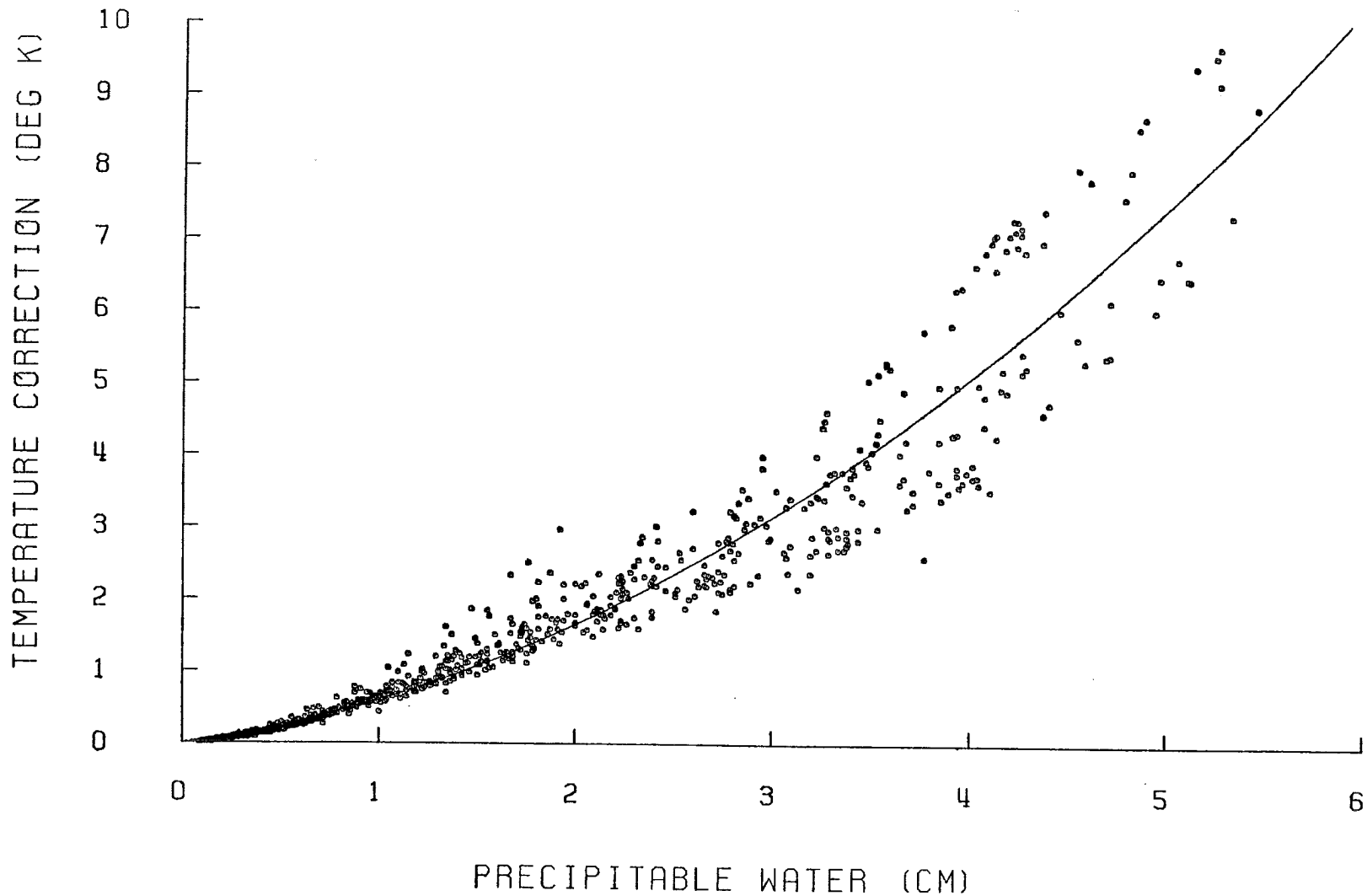


Figure 10. Satellite cloud top IR temperature correction as a function of total precipitable water above cloud top.

thin and thick clouds used is the same as that presented by Cox and Griffith (1979).

## 2.6 Aerosol distribution

While there is no really good way to quantitatively observe dust or aerosol distributions over the time and space domains represented by the large scale MONEX study area, regionally representative values of aerosol concentration have been assumed based on aircraft and surface observations. Surface observations of present and past weather conditions include descriptive observations of the dust loading in the atmosphere (e.g. widespread dust in suspension in the air, severe dust storm, sand storm) as well as estimates of visibility at the time of observation. Surface observations made at 0000, 0600, 1200 and 1800 GMT were used in the present study to estimate the horizontal distribution of atmospheric dust. An example of the percent occurrence of a dust loading defined as an observation that noted the suspension of dust in the atmosphere for 1° latitude by 1° longitude grid for June 1979 is shown in figure 11a. Figure 11b displays the visibility associated with these dust outbreaks. Surface dust loading was estimated from the visibility observations following the work of Patterson and Gillette (1977);

$$M = C/V^{\gamma} \quad (4)$$

where  $M$  = mass concentration in  $\text{g m}^{-3}$  and  $V$  is the visibility in km. For airborne soil particles Patterson and Gillette (1977) derived an average value of  $C = 2.3 \times 10^{-2} \text{ g m}^{-3} \text{ km}$  and  $\gamma = 1.07$ .  $C$  and  $\gamma$  are dependent on such factors as windspeed, degree of local erosion and distance from the source region (all of which are difficult to assess in the present study); the above

# DUST OUTBREAKS

## JUNE 1979

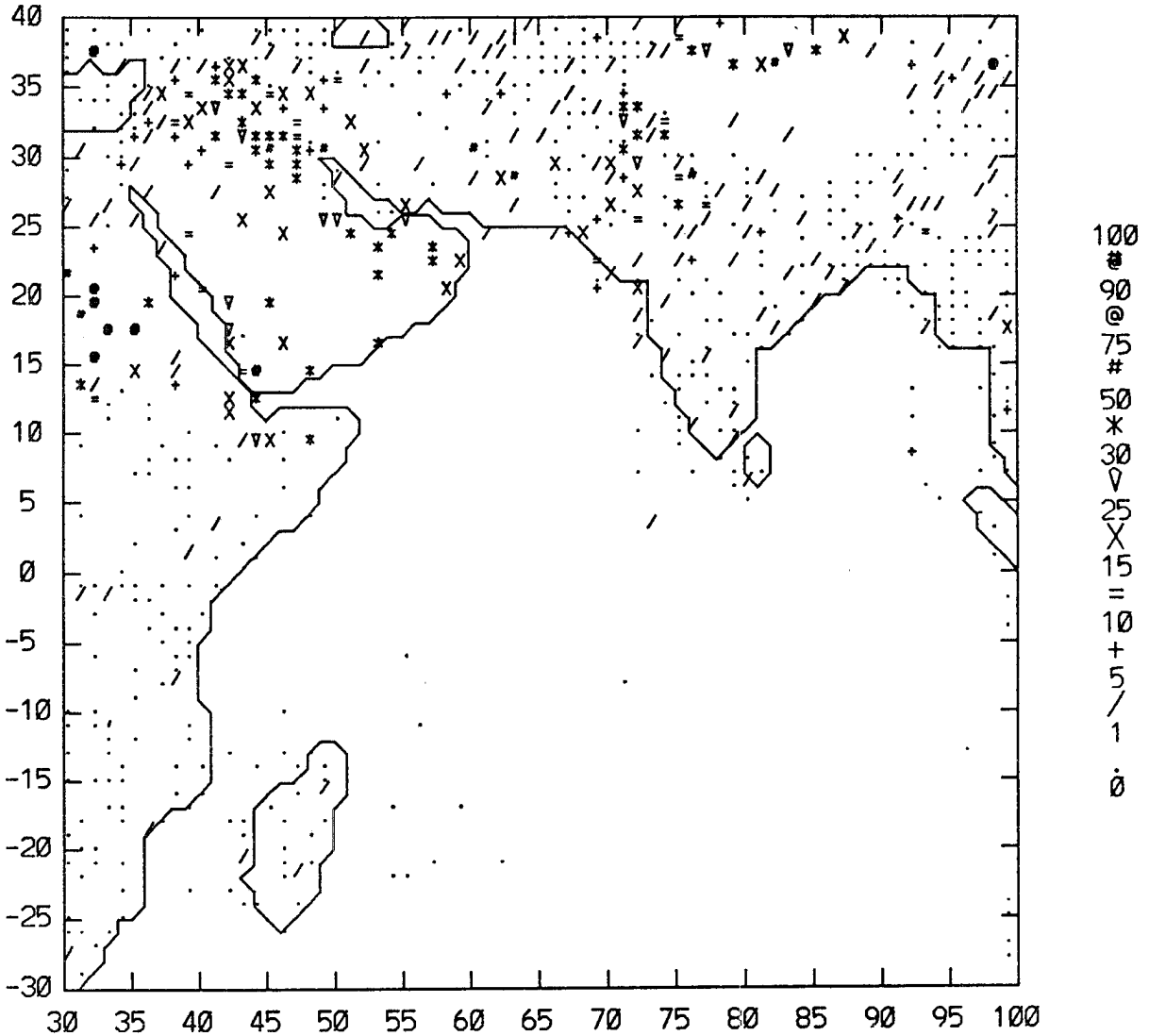


Figure 11a. Percent occurrence (see legend) of surface based observations that noted the suspension of dust in the atmosphere for the month of June 1979. Observations were averaged over a 1° grid.

# VISIBILITY (KM)

## JUNE 1979

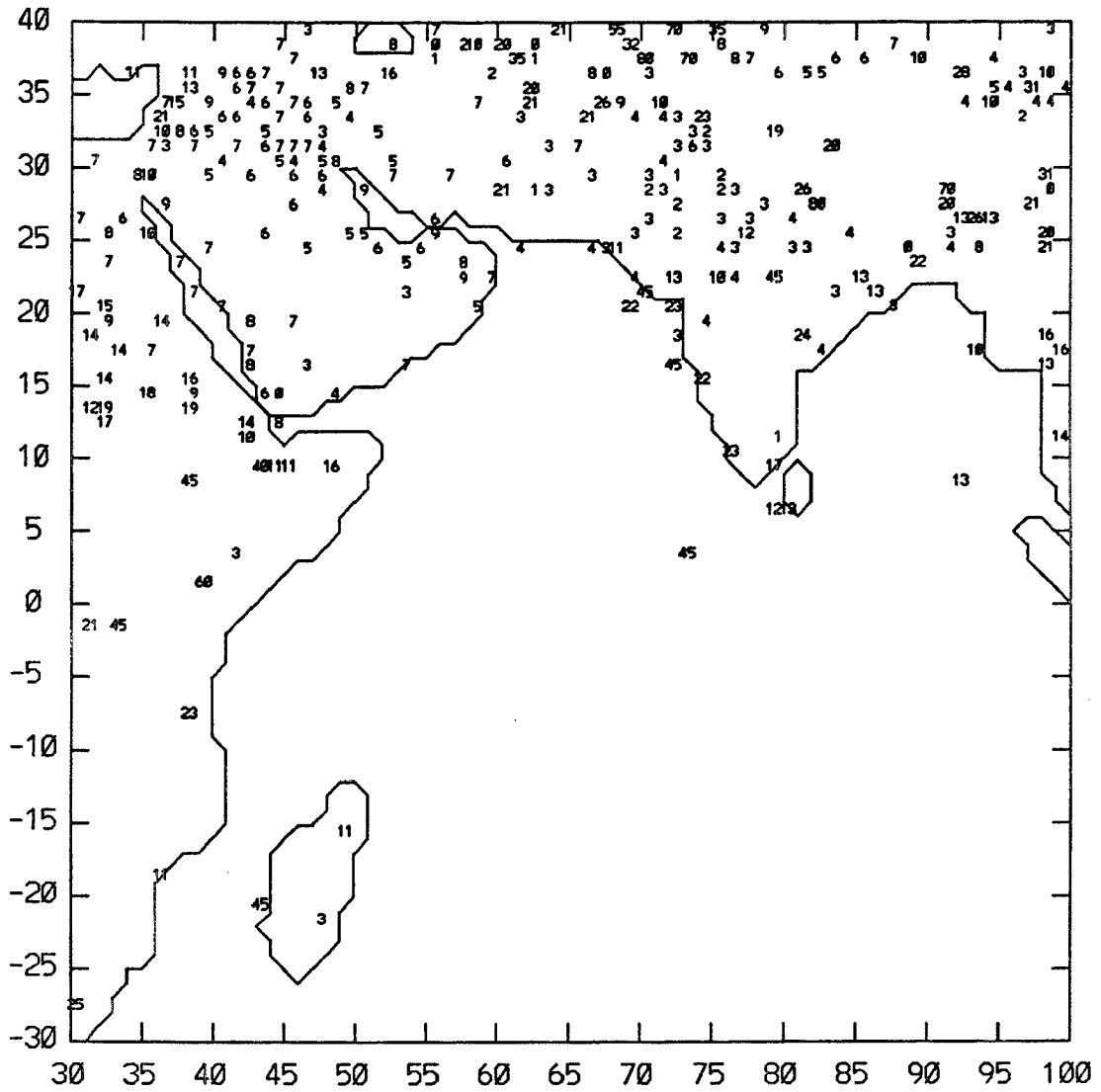


Figure 11b. Mean surface estimated visibility (km) associated with the dust outbreaks of figure 11.

relationship is used as a first order approximation to the dust mass loading near the surface. The vertical profile of dust mass loading is assumed to have the same dependence with height as in the Ackerman and Cox (1982) mean case. Concentrations were adjusted proportionately according to the assumed surface concentration.

Figure 12 depicts the number of days in which an observation of suspended dust was made as a function of month for the year 1979 for several stations in the southwest monsoon region. Also shown (heavy line) are the number of 'dust days' in which the visibility was less than 5 km. The dashed line includes dust days and days with haze observations. Tic marks on the ordinate represent 10 day increments while those along the abscissa represent the months of January, April, August and December. An annual cycle in the number of days with suspended aerosols is evident at most stations. The summer maximum in the number of dust days over the desert regions is correlated with the high summer insolation. For example, the high daytime summer, near-surface temperatures result in large turbulent eddies and a mixed layer which can extend to 600 mb (Ackerman and Cox, 1982). Once dust is injected into the atmosphere it can reach higher altitudes than in the winter months when the mixed layer and turbulent eddies are much smaller; this results in larger summer residence times and greater transportation distances. Seasonal variation in regional circulation systems also play an important role in the distribution of dust days. For example, the summer minimum at New Delhi and the minimum in the occurrence of haze in the Ghangi River valley region is associated with the heavy monsoon rains.

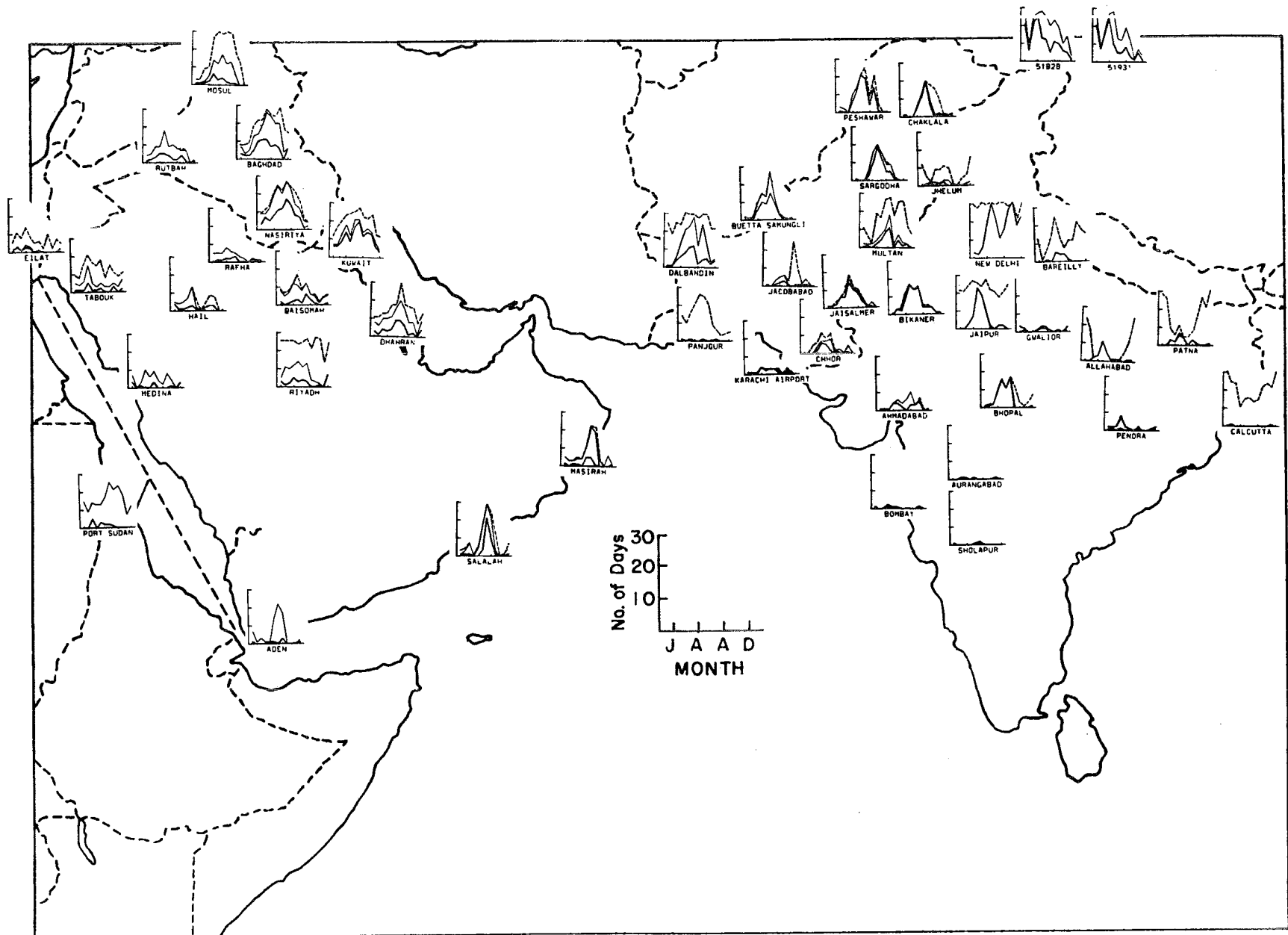


Figure 12. Number of days in which an observation of suspended dust was made as a function of month for the year 1979 for several stations in the southwest monsoon region. Also shown (heavy line) are the number of dust days in which the visibility was less than 5 km. The dashed line includes dust days and days with haze observations. Tic marks on the ordinate represent 10 day increments while those along the abscissa represent the months of January, April, August and December.

## 2.7 Spatial and Temporal Resolution of the Radiative Energy Budgets

Since the differential heating between land and ocean areas plays an important role in the development of the southwest monsoon, it is important that the horizontal scale of the radiative energy budgets (REB) be small enough to show these differences. For the purposes of the present study, a spatial scale of  $1^\circ$  latitude by  $1^\circ$  longitude was chosen to classify surface type (ocean, land or Himalaya). Radiative calculations for each  $1^\circ \times 1^\circ$  division individually would require large amounts of computer time; thus REB were computed on a larger spatial scale. The area of interest was divided into  $5^\circ \times 5^\circ$  regions, each  $5^\circ \times 5^\circ$  region was then subdivided into  $1^\circ \times 1^\circ$  divisions. Each of the  $1^\circ \times 1^\circ$  divisions was classified as an ocean, land or Himalaya subregion. Figure 1 depicts this classification where high mountains are considered a Himalaya subregion, and the remaining symbols denote different land subregions. Mean temperature and moisture profiles, dust loading, surface albedo, and topography were then determined for each subregion within the  $5^\circ \times 5^\circ$  grid. Radiative calculations were made for each subregion (e.g. ocean, land or Himalaya) for each  $5^\circ \times 5^\circ$  grid. Individual atmospheric radiative heating profiles were calculated at a vertical resolution of 50 mb. Radiative energy budgets were composited for each  $1^\circ \times 1^\circ$  division by linearly weighting clear and cloud radiative divergence profiles at a vertical resolution of 100 mb. Separate energy budgets were derived for nighttime and daytime periods for the six different 10 day periods listed in Table 1. While a spatial scale of  $1^\circ$  latitude by  $1^\circ$  longitude was used in deriving the radiative fields, most of the results which follow are spatial averages.

### 3. RESULTS

Prior to discussing the distribution and variability of the radiative components associated with the southwest summer monsoon of 1979, it is instructive to compare cloud cover estimates from three different observation platforms; the GOES-1 VISSR, the TIROS-N AVHRR and surface observations. (A detailed analysis of the satellite derived cloud cover and its relationship to monsoon activity is presented in the Appendix). The three data sets have different spatial and temporal resolutions, which can lead to large discrepancies in derived cloud amount at any given time and place (Ackerman and Cox, 1981). However, these differences can be reduced by appropriate temporal and/or spatial averaging as discussed below. Figure 13 depicts total cloud cover derived from the GOES-1 (G), the TIROS-N (T) and surface observations (solid line) for four stations. The four stations were chosen to represent different geographical regions; Dharan, Saudi Arabia (desert), New Delhi, India (continental), Madras, India (coastal) and Maldiva (island). Also shown in the figures are the present weather surface observations, made four times a day (00,06,12 and 18 GMT). The methodology in deriving the cloud top distributions from the two satellites is perfectly general and most differences should result from different spatial and temporal resolutions as well as the different satellite viewing angles and the associated cloud geometry and cloud distribution. The problem of satellite viewing angle and derived fractional cloud amount has been discussed by Davis and Cox (1980). While there are problems in comparing satellite and surface estimates of cloud cover (Ackerman and Cox, 1981), the three techniques show similar trends although large differences may exist at any one time period. As one would

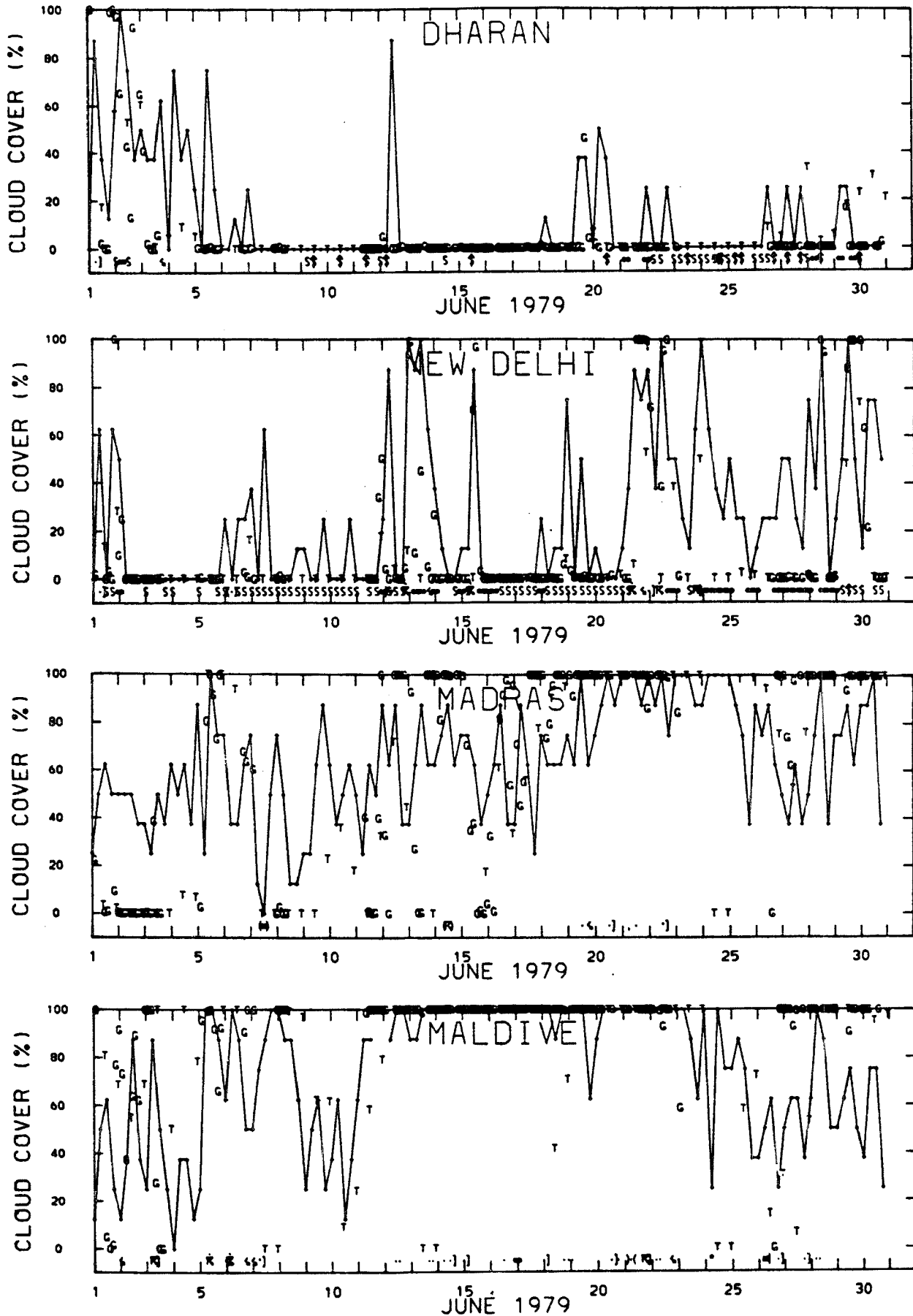


Figure 13. Total cloud cover derived from the GOES-1 (G), TIROS-N (T) and surface (solid line with +) observations for four different stations for June 1979. Present weather surface observations are depicted in the bottom of each figure.

expect, the three observations agree best when there is total cloud cover or clear skies.

Keeping the maximum spatial resolution, total cloud cover was averaged over the month of June 1979 for the three different methodologies and the results are shown in figure 14. There is good agreement in the spatial distribution of monthly mean cloud cover among the three techniques. The agreement between the GOES-1 and surface observations are best as both capture a better representation of the cloud cover diurnal variation. While the TIROS-N only samples the cloud cover twice daily, it does give a reasonable representation in the monthly mean cloud cover. A comparison of GOES-1 derived high cloud distribution versus the TIROS-N derived amount is shown in figure 15. The comparison is quite good especially considering the TIROS-N temporal resolution.

The effect of spatial averaging is shown in figure 16 where the highest temporal resolution of each of the observations has been retained. The spatial averaging was performed for four regions: the Arabian Sea, the Bay of Bengal, the Indian Subcontinent and the Saudi Arabian Peninsula. The thick lines represent TIROS-N measurements, individual points (G) mark the GOES-1 retrieval while the thin lines depict the surface observations. The relationship between the variations in cloud cover and monsoon activity are discussed in the Appendix; however here we want to point out the excellent agreement between the two satellite retrieved cloud cover estimates when averaged over these geographic regions. The largest discrepancies occur over the Indian subcontinent during the onset phase. The surface estimates of cloud cover over Saudi Arabia are much higher than the satellite estimates. While some of these differences may be attributed to difficulties in the satellite retrieval of thin cloud, most of the discrepancy is a result of the

# PERCENT CLEAR

## JUNE 1979

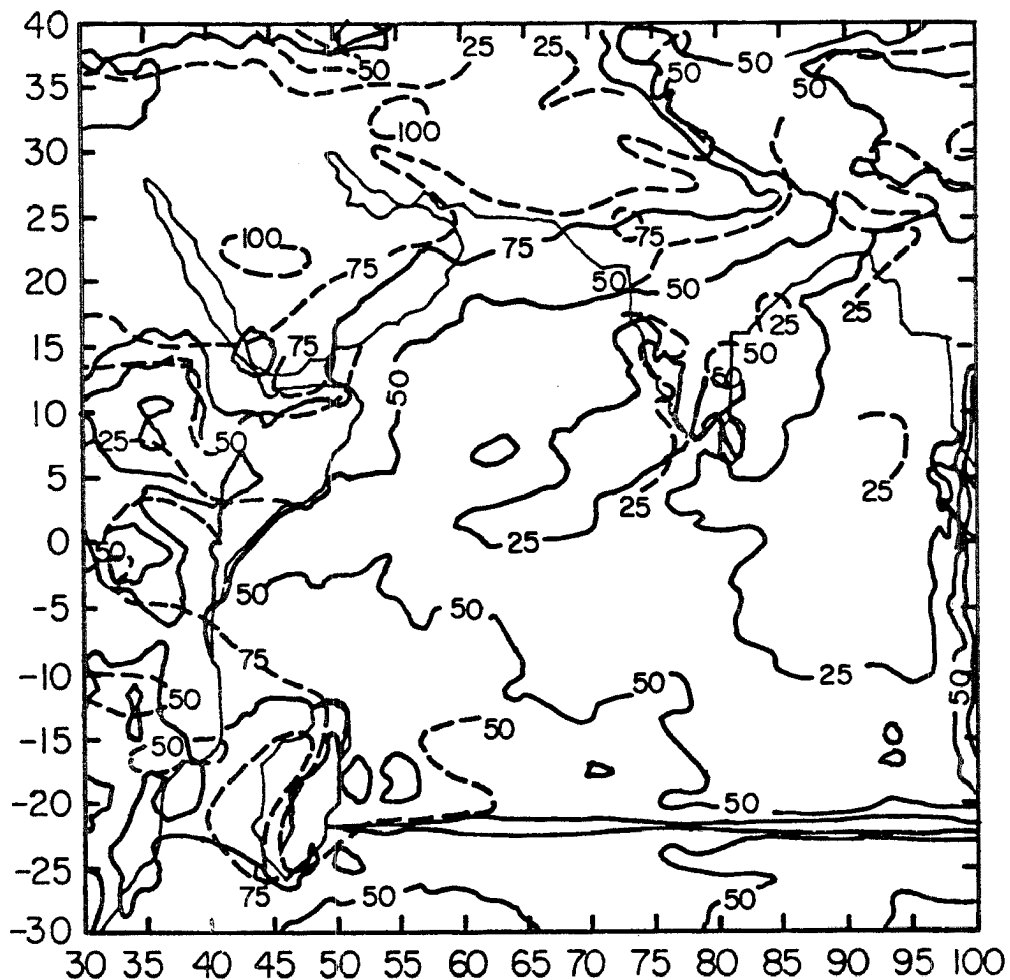


Figure 14a. Monthly mean percent clear regions for June 1979 as derived from surface observations (dashed line) and the GOES-1 observations (solid line).

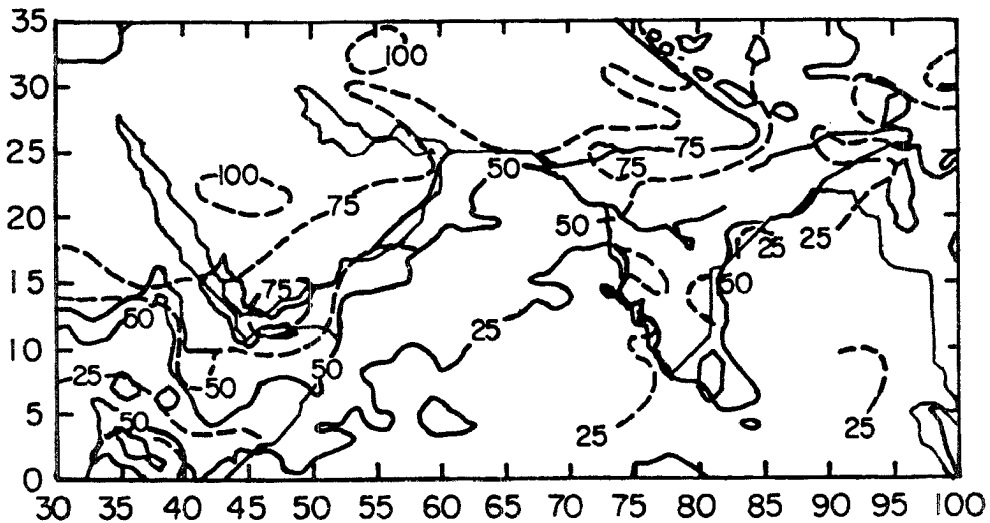


Figure 14b. Monthly mean percent clear regions for June 1979 as derived from surface observations (dashed line) and the TIROS-N satellite (solid line).

# HIGH CLOUDS JUNE 1979

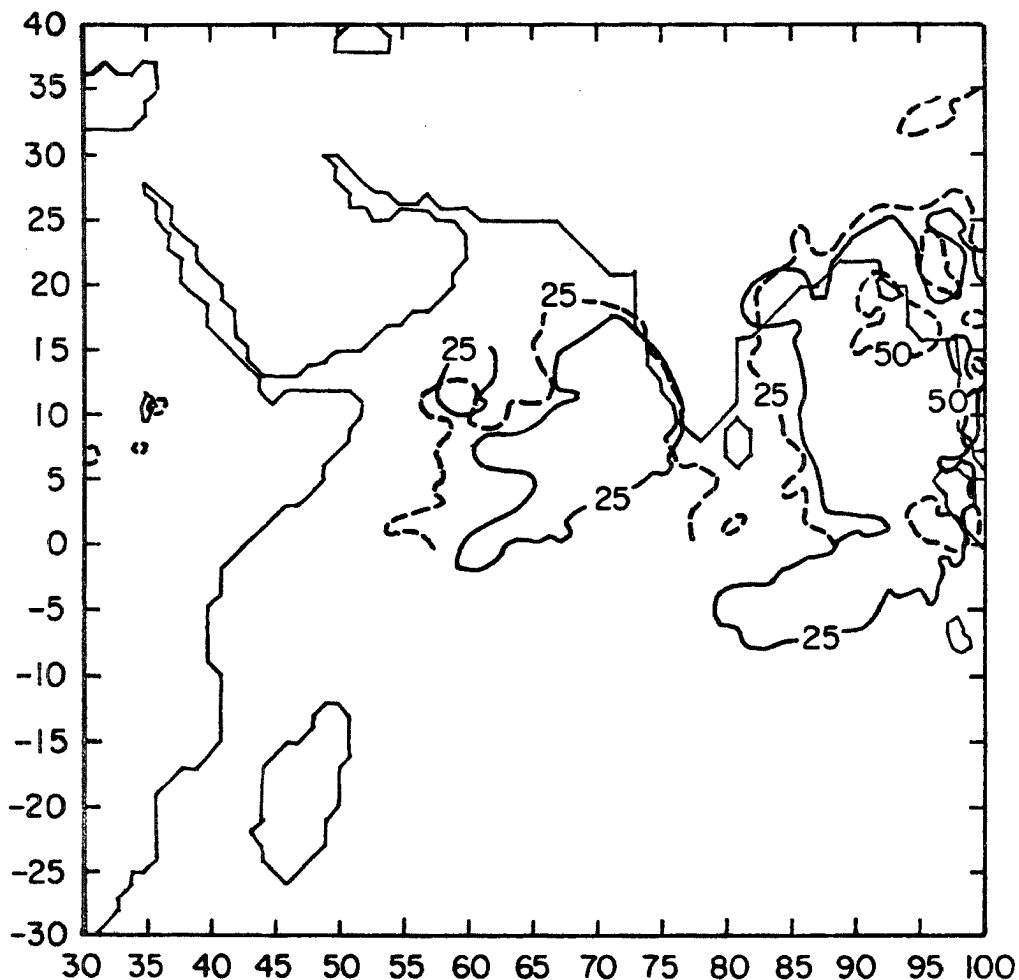


Figure 15. Comparison of the percent of high clouds (cloud tops  $\leq$  400 mb) derived from the GOES-1 (solid line) and TIROS-N (dashed line) for the month of June 1979. Contour intervals are 25% coverage.

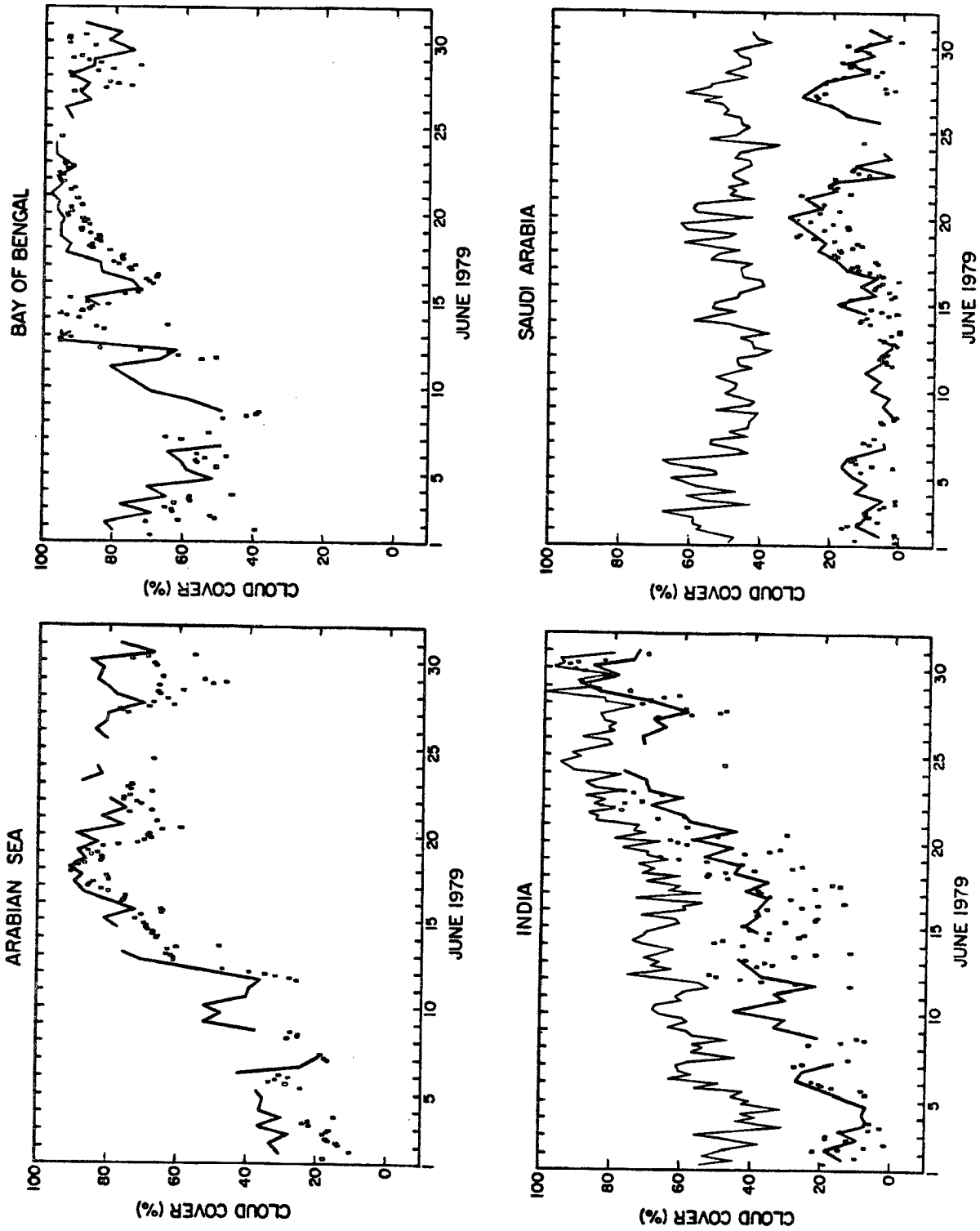


Figure 16. Comparison of total cloud amount for the month of June 1979 averaged over four geographic regions as derived by the GOES-1 (G), TIROS-N (thick line) and surface (thin line) analysis.

geographic distribution of the surface observations. Most of the surface stations are located near the coast of the peninsula (figure 11); this biases the cloud estimate to higher values (see figure 15). A similar problem, though not as severe, is seen in cloud cover estimates over India. There is also good agreement in the satellite derived high cloud (cloud top < 400 mb) cover for the four regions as shown in figure 17.

While there is presently no adequate procedure for determining the accuracy of a given method for deriving cloud cover, the above intercomparisons suggest that while large errors may result on small time and space scales, appropriate temporal and spatial averaging may yield reasonable estimates of cloud cover and thus of the radiative energy budgets. The remainder of this section presents analysis of the radiative energy budgets derived using the GOES-1 cloud cover analysis.

Table 1. Periods of radiative energy budget estimates.

<u>PERIOD</u>	<u>CALENDAR DAYS</u>
January Phase	January 11-20
February Phase	February 11-20
Early May Phase	May 1-10
Pre-onset Phase	May 27 - June 5
Onset Phase	June 11 - June 22
Post-onset Phase	June 23 - June 30

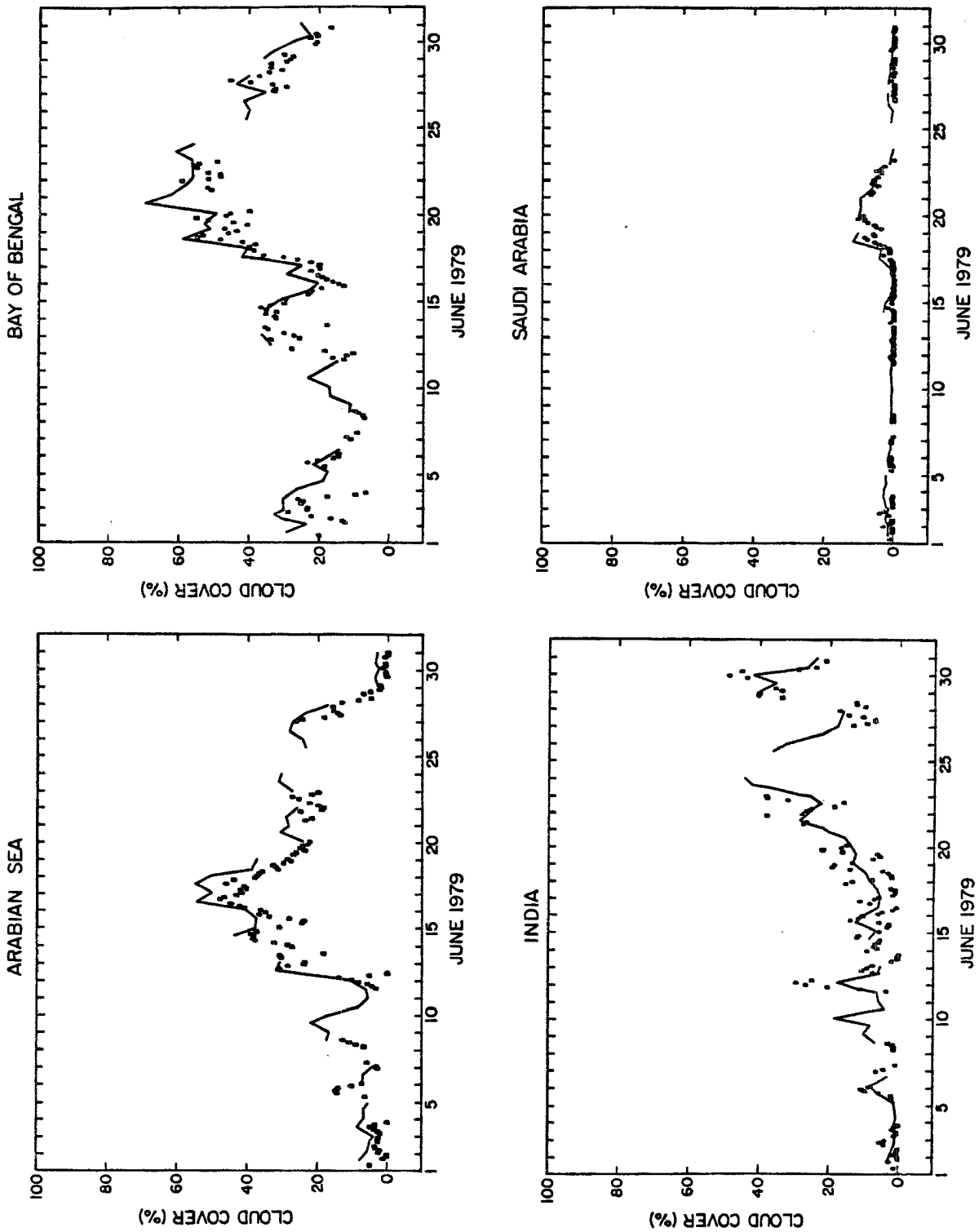


Figure 17. Comparison of high cloud amount for the month of June 1979 averaged over four geographic regions as derived by the GOES-1 (G) and TIROS-N (thick line) analysis.

### 3.1 Radiative Energy Budgets

The following sections discuss the primary characteristics of the derived radiative energy budgets associated with the 1979 southwest summer monsoon. The radiative heating rates are first compared with climatological estimates (Katayama, 1967 and Dopplnick, 1979). The horizontal variability of the total tropospheric convergence (TTC) is presented and discussed for each of the six phases, and the effects of spatial averaging on the radiative energy losses is explored. Gradients of TTC are also presented. Changes in the vertical radiative heating profiles for different geographic regions are discussed in relation to monsoon activity. Cross-sectional analysis of radiative heating profiles are presented for three of the six phases and changes in the estimated net radiative surface flux are presented and discussed.

#### 3.1a Comparison with climatological estimates of radiative heating

Figure 18 shows a comparison of the latitudinal mean radiative heating rates of the present study with the zonal mean climatological estimates given by Dopplnick (1979). Figure 18a displays the mean heating rates of the January and February phases of the present study, as well as the Dopplnick (1979) December-February case, while figure 18b presents the mean profile of the pre-onset, onset and post-onset periods with the climatological estimates for June, July and August given by Dopplnick (1979). The Dopplnick winter heating rates (figure 18a) display a maximum cooling in the middle troposphere of the northern hemisphere; the level of maximum cooling increases as the equator is approached. The present study also features maximum cooling in the northern hemisphere middle troposphere, however the location of maximum cooling tends to be lower in the atmosphere with decreasing latitude. Both analyses depict

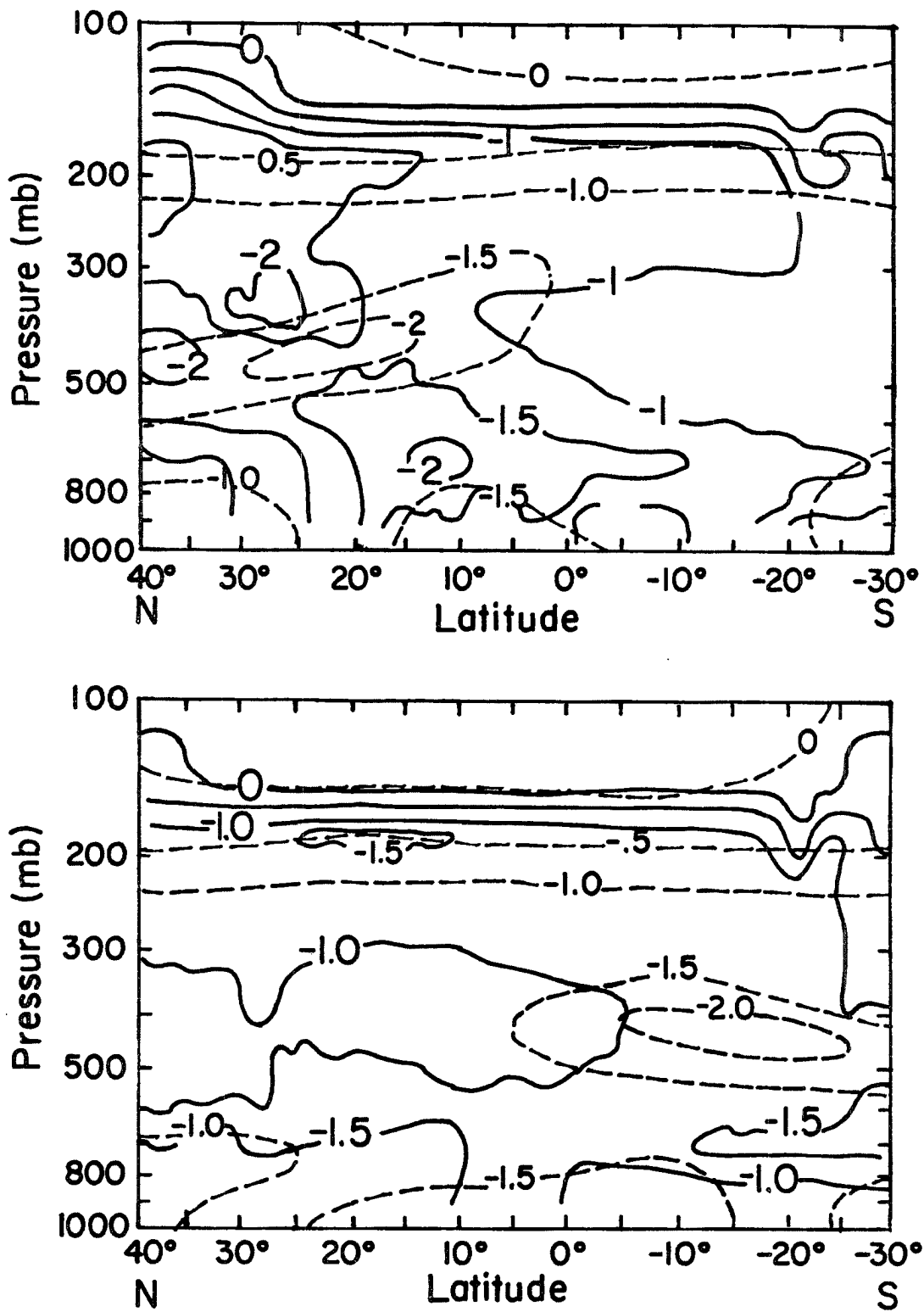


Figure 18. Comparison of the present results (solid lines) with the results of Dopplick (1979) (dashed lines). Top: comparison of the Dopplick December-February profiles with the mean of the January and February phases of the present study. Bottom: comparison of Dopplick June-August results with the pre-onset, onset and post-onset mean of the present study Units of the radiative heating are  $^{\circ}\text{C}/\text{Day}$ .

a minimum cooling in the southern hemisphere middle tropospheric levels. During the summer months the Dopplick profiles (figure 18b) have a maximum radiative cooling between 400-500 mb in the southern hemisphere. Results of the present study do not display such a feature.

Figure 19 compares zonal cross-sections of net radiative heating for the January and February mean of the present study with the January case of Katayama (1967). For the case of the zonal cross-section along the equator Katayama shows a region of relative minimum cooling near the 400 mb level. In the present study a relative minimum occurs higher in the troposphere, and is smaller in magnitude. Discrepancies in the lower atmosphere between the two studies result from the inclusion of the 8-12  $\mu\text{m}$  continuum absorption in the present study, an effect which was not included in the Katayama results. Large differences in radiative heating rates appear in the cross-sectional analysis along 20°N latitude. Principal reasons for the differences are the inclusion of the water vapour continuum in the present study, and differences in cloud distribution, and their associated radiative properties.

### 3.1b Total tropospheric convergence

Figure 20 depicts the 24 hour mean total tropospheric convergence (TTC) profiles in  $\text{Wm}^{-2}$  for the six periods of the 1979 monsoon (see Table 1). The TTC of the January and February periods exhibit a zonal character, particularly over the oceanic regions, with larger cooling to the north and smaller cooling to the south. During the January period the maximum tropospheric cooling occurs over the northern Arabian Peninsula and the northern Indian subcontinent. In the February period the maximum cooling occurs over the northern Arabian Sea and northern Bay of Bengal. In both periods the range of TTC is approximately -160 to -65  $\text{W m}^{-2}$ .

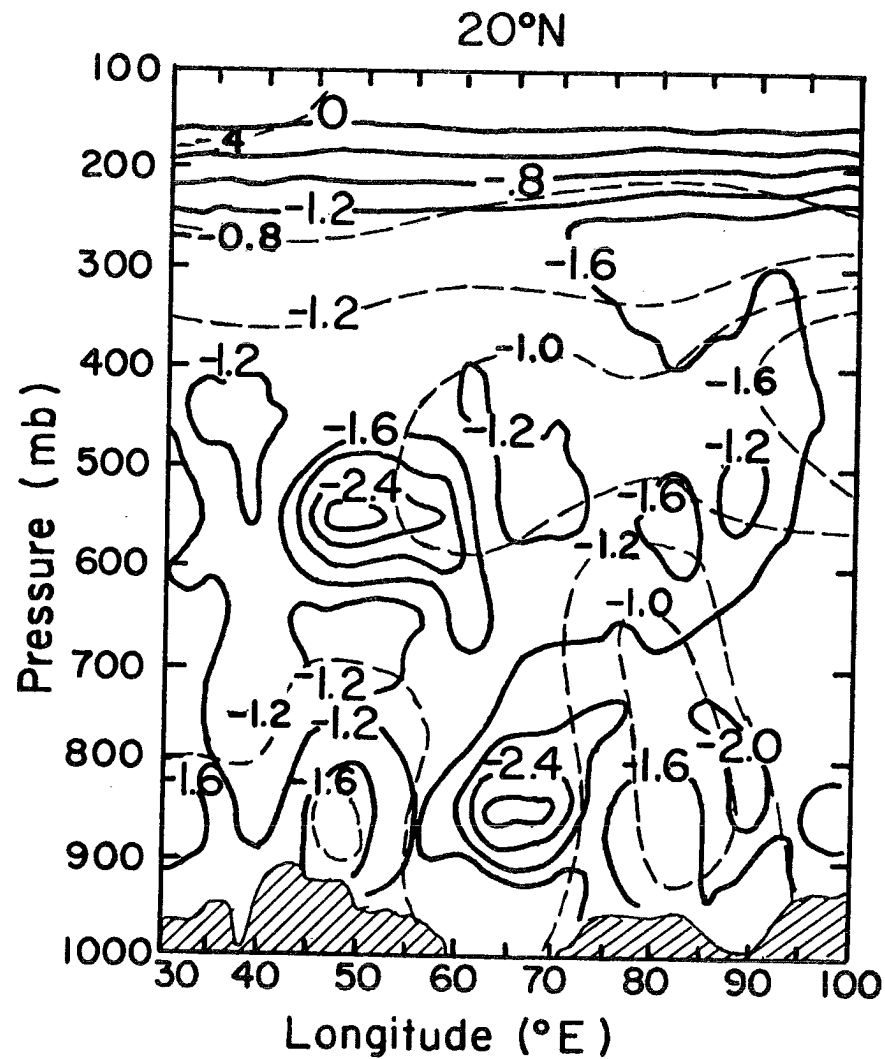
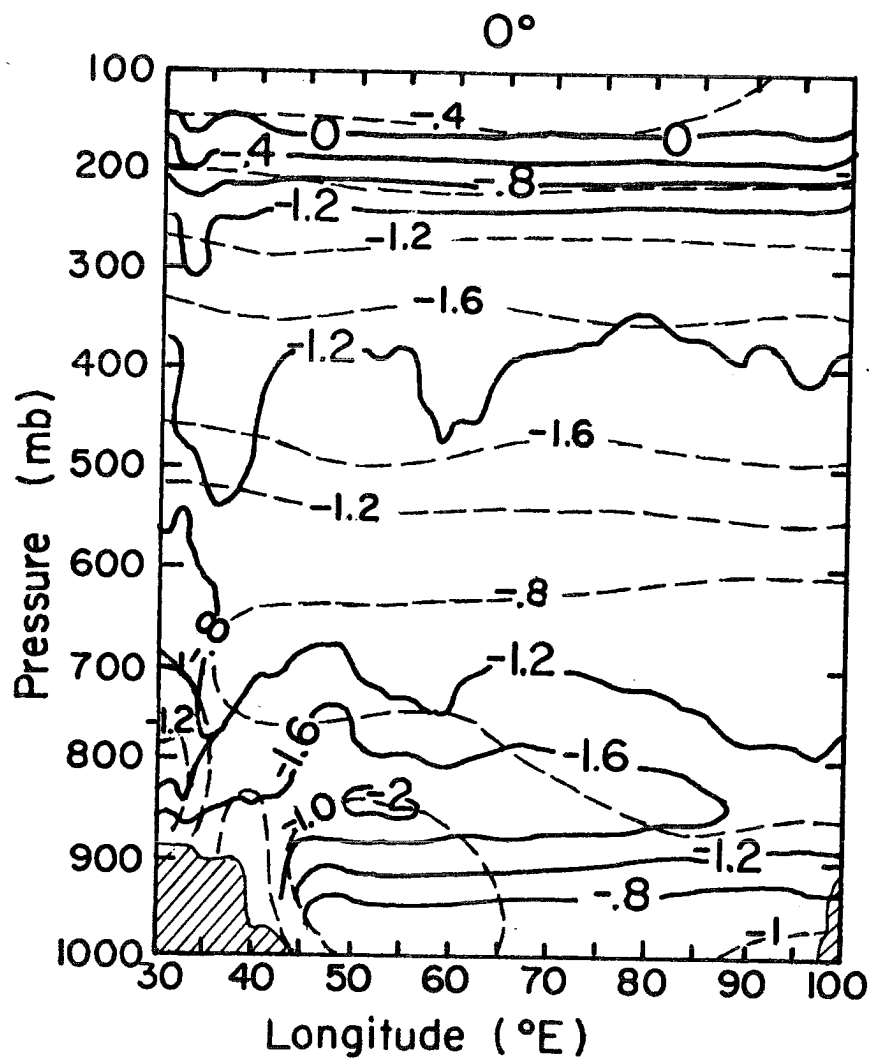


Figure 19. Zonal cross-sections of radiative heating ( $^{\circ}\text{C}/\text{Day}$ ) for the equator (a) and  $20^{\circ}\text{N}$  (b). The results for the January case of Katayama (1967) are given as dashed lines, while the solid lines depict the results for the average of the January and February phases of the present study.

# 24 HOUR TROPOSPHERIC CONVERGENCE

JANUARY

GOES-1

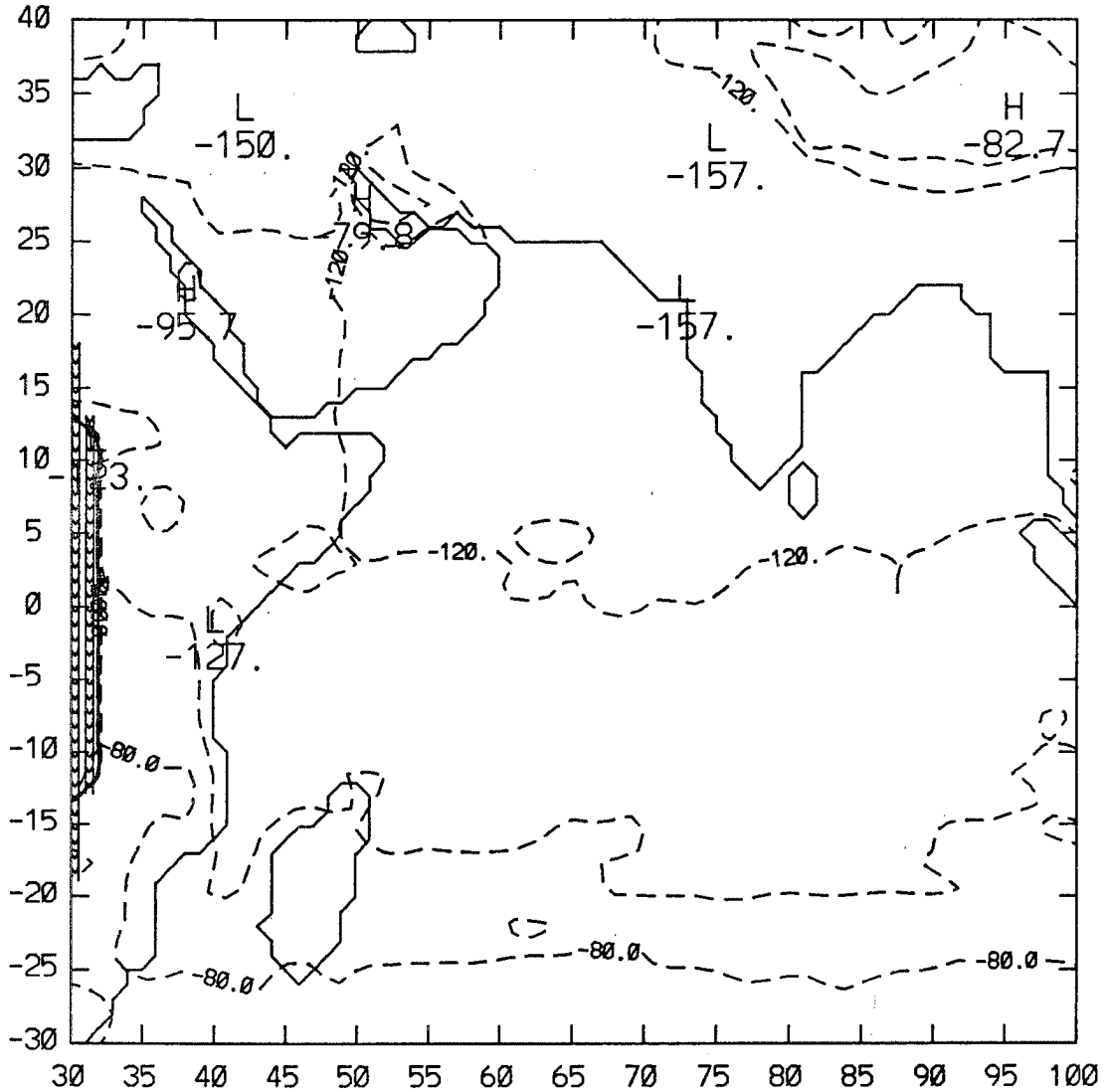


Figure 20. The 24 hour mean total tropospheric convergence in  $W m^{-2}$  for the six phases of the 1979 monsoon. Regions of missing data are denoted with M. Contour interval is  $20 W m^{-2}$

# 24 HOUR TROPOSPHERIC CONVERGENCE

FEBUARY

GOES-1

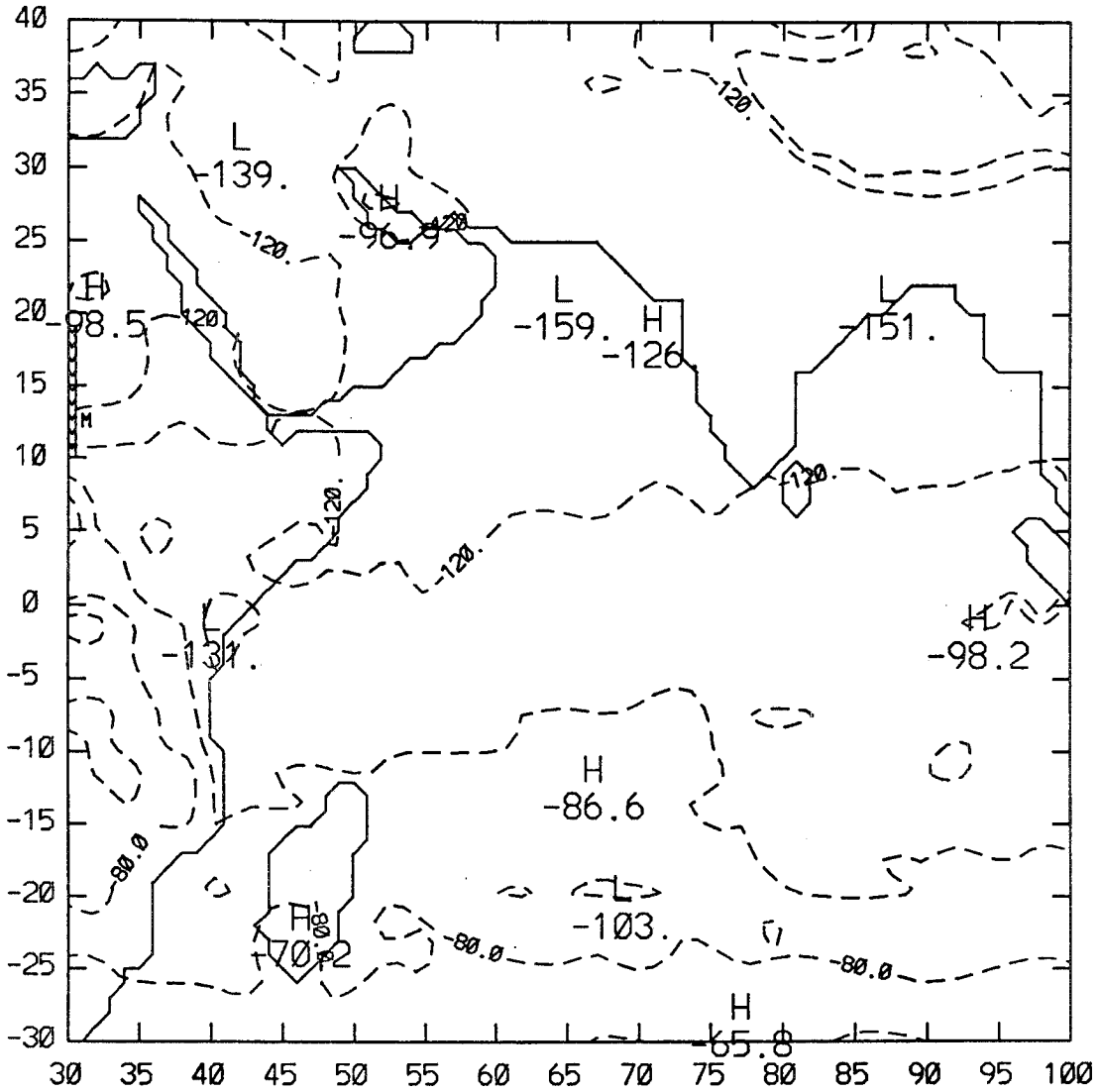


Figure 20. Continued

# 24 HOUR TROPOSPHERIC CONVERGENCE EARLY MAY

GOES-1

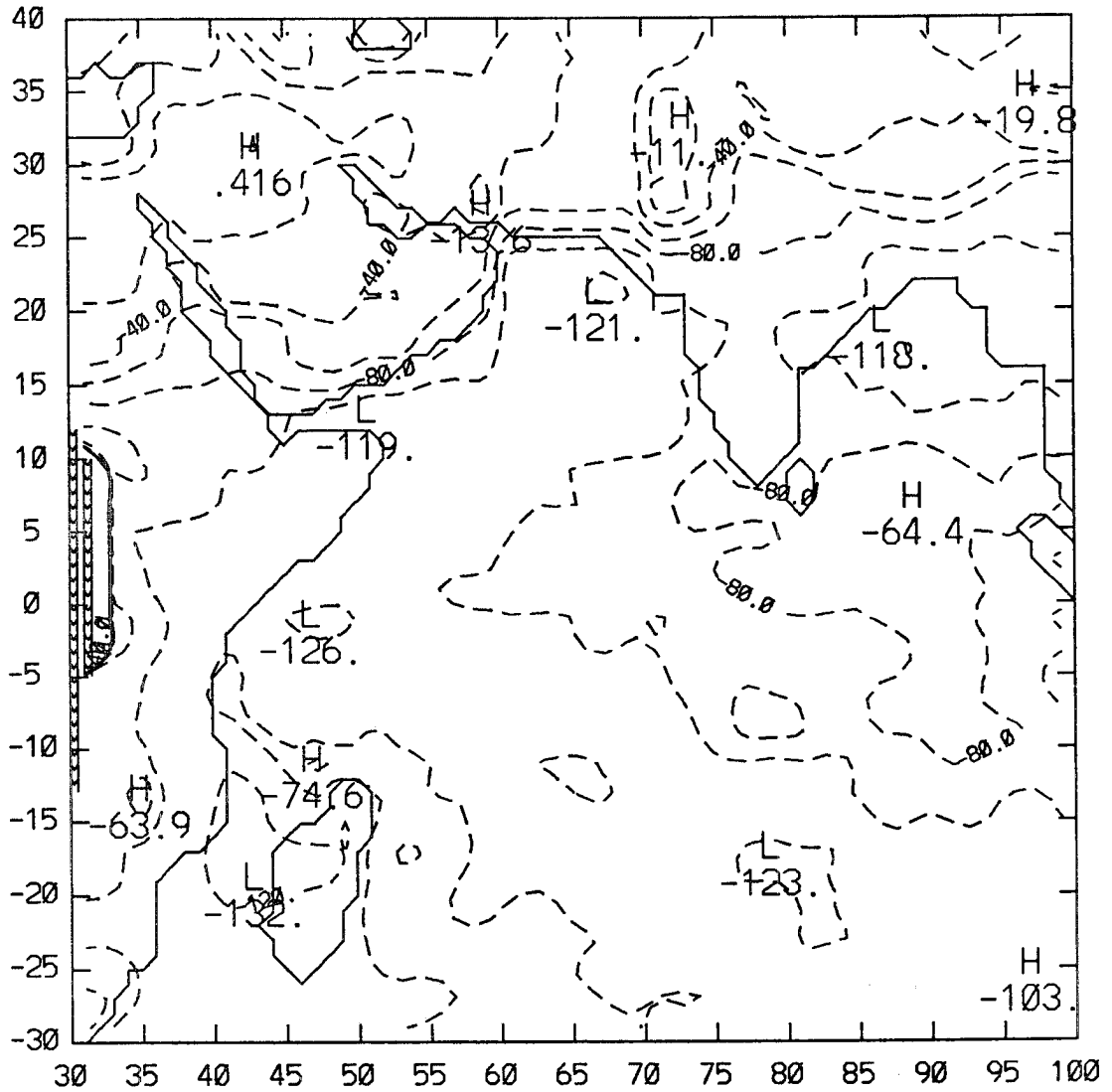


Figure 20. Continued

# 24 HOUR TROPOSPHERIC CONVERGENCE

PRE-ONSET

GOES-1

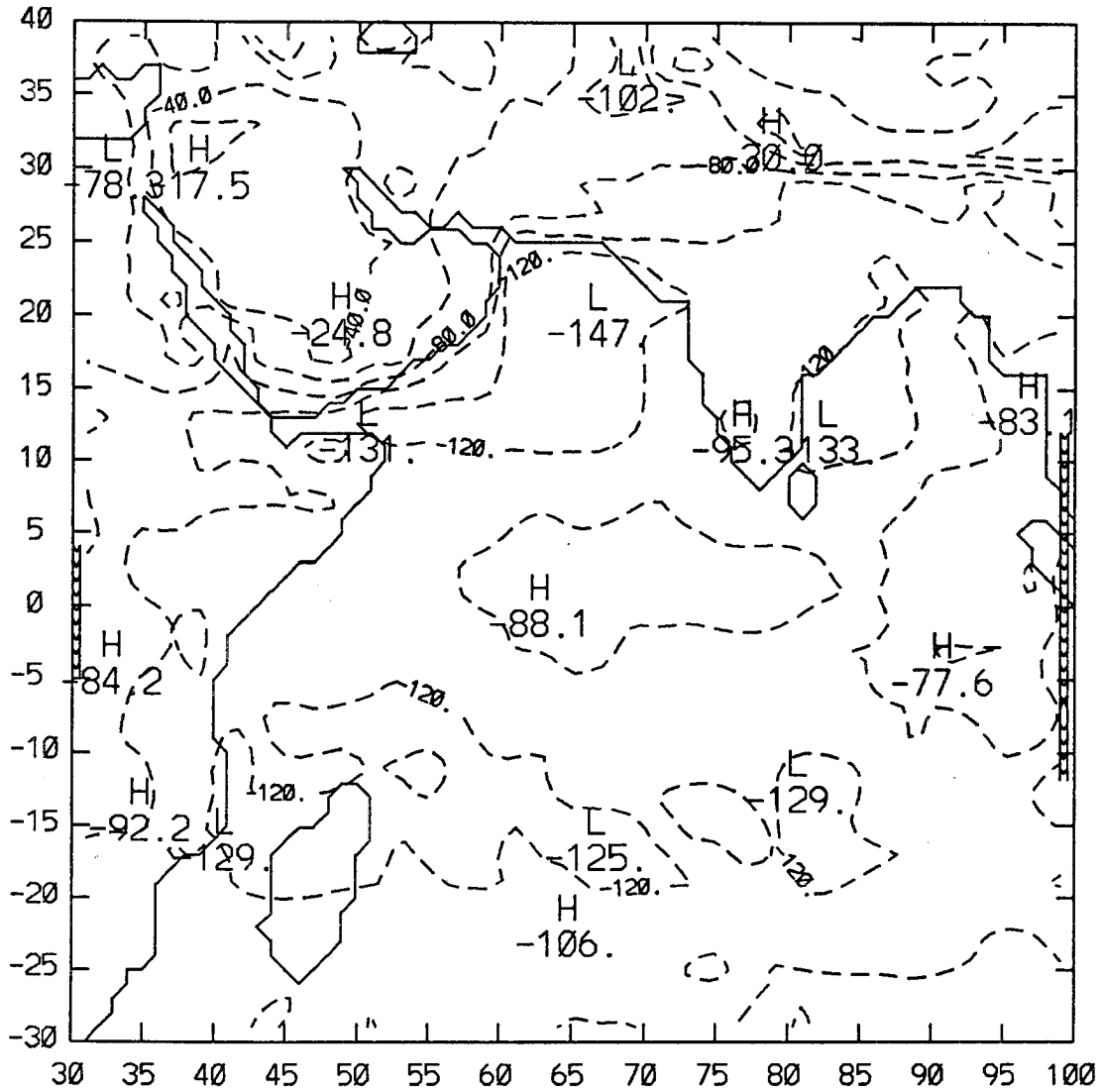


Figure 20. Continued



# 24 HOUR TROPOSPHERIC CONVERGENCE POST-ONSET

GOES-1

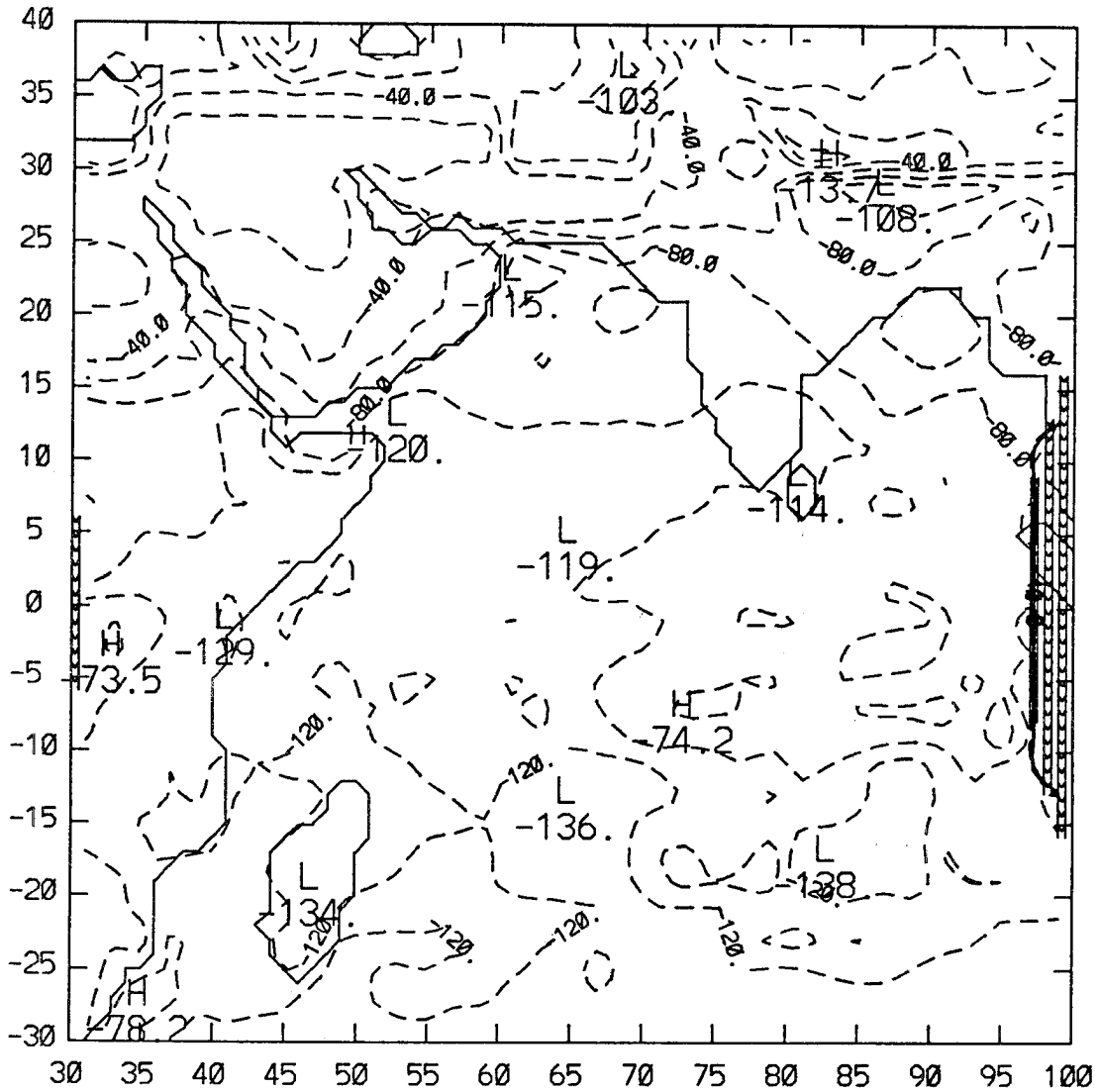


Figure 20. Continued

By early May zonal gradients in TTC are as large as longitudinal gradients, with a range of 0 to  $-130 \text{ W m}^{-2}$ . Maximum cooling is associated with cloud free oceanic regions (e.g. over the northern Arabian Sea and Bay of Bengal). The minimum cooling in the southern Bay of Bengal results from suppression of the LW energy loss and enhancement of the atmospheric SW absorption arising from clouds associated with the large convective systems of this region. The weak heating over the Saudi Arabian peninsula is caused by solar absorption by dust, resulting in radiative heating between 500-700 mb.

In the pre-onset phase the TTC tends to a zonal structure over the Indian Ocean south of  $10^\circ \text{ N}$ . The range of TTC during this period is approximately  $-150$  to  $-15 \text{ W m}^{-2}$ . Maximum cooling over the Arabian Sea and Bay of Bengal results from strong low level cooling (cooling between the surface and 700 mb) associated with clear sky conditions. These regions of cooling are larger than in the previous period. The minimum cooling over the southern regions of India results from convective clouds, which suppresses the low level cooling while enhancing the radiative cooling of the upper troposphere. Minimum cooling occurs over the Saudi Arabian peninsula as a result of the dry, dusty atmosphere. During this phase of the monsoon there are strong meridional gradients in the radiative heating between  $10^\circ$  and  $25^\circ \text{ N}$ .

In the onset phase the monsoon advances northward and cloud cover extends into the northern regions of the Bay of Bengal further suppressing the cooling minimum observed there in the previous phases. The cloud free northern Arabian Sea continues to exhibit a relative minimum in TTC, while a relative maximum still exists over Saudi Arabia resulting in a strong meridional gradient of TTC. Convective activity over the Bay of Bengal and the eastern Arabian Sea results in a weakening of the TTC gradients exhibited in the previous two phases. The Indian Ocean tends to a more zonally uniform TTC

than the northern region. The range of TTC over the region is -15 to -140  $Wm^{-2}$ .

In general the large amounts of cloud associated with the post-onset phase suppress the horizontal gradients in TTC observed in the Arabian Sea in the previous phases. The range of TTC is -15 to -140  $Wm^{-2}$ . As in the previous phases convective regions display relative minima in TTC while the clear oceanic regions exhibit maximum cooling. The desert regions also exhibit regions of minimum cooling.

The period of maximum variability in TTC is the early May and post-onset phases, as seen in the calculation of the coefficient of variation of the latitudinal and longitudinal mean TTC. The coefficient of variation is defined as the ratio of the standard deviation to the mean, with large values representing large dispersion. Table 2 presents the coefficient of variation for the latitudinal mean TTC, the early May and post-onset periods possess the greatest variability, while the January and February periods exhibit the smallest dispersion. Greatest variability occurs northward of  $10^{\circ}N$  in all six periods with smallest variabilities in the southern Indian Ocean. This is to be expected considering the land distribution. During the early May through post-onset periods, the presence of large cloud amounts and dust results in an increase in the variability northward of  $10^{\circ}N$ . The coefficient of variation for the longitudinal mean TTC is given in Table 3. As in the latitudinal mean TTC, the January and February periods display the least dispersion. Comparison of Tables 2 and 3 reveal that the latitudinal variations in TTC are as large as the longitudinal variations. Spatial averaging does not remove these large variations as shown in figure 21, which depicts analysis of the pre-onset TTC on spatial scales of  $3^{\circ}$ ,  $5^{\circ}$ ,  $7^{\circ}$  and  $10^{\circ}$ . Even when averaged over a  $10^{\circ}$  grid TTC still does not exhibit a

TABLE 2. Coefficient of Variation for the Latitudinal Mean TTC

Latitude	January	February	Early May	Pre-Onset	Onset	Post-Onset
40°N-35°N	.158	.126	.399	.264	.262	.257
35°N-30°N	.186	.174	.548	.379	.520	.636
30°N-25°N	.161	.125	.640	.388	.605	.645
25°N-20°N	.136	.130	.489	.445	.498	.467
20°N-15°N	.106	.096	.308	.308	.260	.264
15°N-10°N	.067	.057	.114	.119	.163	.153
10°N- 5°N	.076	.081	.165	.073	.147	.112
5°N- 0°N	.056	.088	.185	.088	.114	.122
0°N- 5°S	.080	.139	.143	.104	.095	.145
5°S-10°S	.070	.138	.155	.089	.108	.152
10°S-15°S	.103	.136	.136	.082	.061	.094
15°S-20°S	.091	.084	.111	.053	.085	.107
20°S-25°S	.051	.057	.081	.049	.053	.088
25°S-30°S	.081	.070	.093	.097	.064	.120

TABLE 3. Coefficient of Variation for the Longitudinal Mean TTC

Longitude	January	February	Early May	Pre-Onset	Onset	Post-Onset
30°E-35°E	.253	.261	.466	.188	.415	.429
35°E-40°E	.169	.177	.482	.397	.345	.447
40°E-45°E	.164	.151	.503	.423	.471	.468
45°E-50°E	.160	.165	.462	.432	.484	.524
50°E-55°E	.191	.183	.441	.363	.412	.430
55°E-60°E	.204	.198	.366	.240	.360	.363
60°E-65°E	.200	.208	.292	.235	.297	.304
65°E-70°E	.197	.201	.244	.193	.273	.273
70°E-75°E	.20	.199	.392	.195	.261	.319
75°E-80°E	.193	.194	.306	.201	.251	.255
80°E-85°E	.20	.192	.337	.203	.252	.289
85°E-90°E	.212	.207	.327	.194	.241	.316
90°E-95°E	.216	.195	.281	.215	.258	.282
95°E-100°E	.212	.192	.299	.282	.291	.341

zonal pattern. Maximum cooling occurs over the Arabian Sea and Bay of Bengal with suppressed cooling over the northern regions of the Arabian Peninsula. These meridional gradients result from continental/ocean influence as well changes in cloud cover and aerosol distributions.

While large longitudinal variations exist in the TTC, particularly in the early May through post-onset phases, it is instructive to compare the latitudinal averages of TTC in order to compare seasonal differences. Figure 22 depicts latitudinal mean (averaged over 5° longitude) total tropospheric convergence ( $TTC_L$ ) for the six periods. In the January and February periods minimum cooling takes place in the southern sections of the region, with maximum cooling in the 25°N-20°N latitudinal belt. By early May the gradient in  $TTC_L$  is reversed, with maximum cooling in the southern regions and minimum cooling in the northern regions. Similar trends occur for the pre-onset, onset and post-onset phases. These latter three periods have similar  $TTC_L$  in the southern hemisphere, with maximum differences northward of 10°N. The effects of these gradients on the mean meridional circulation can be seen by considering the following expression for the stream function derived from quasigeostrophic theory (Holton, 1979)

$$\left( \frac{\partial^2}{\partial y^2} + \frac{f_0^2}{\sigma} \frac{\partial^2}{\partial \rho^2} \right) \chi = \frac{-f_0}{\sigma} \frac{\partial}{\partial \rho} \frac{\partial M}{\partial y} + \frac{\partial^2 B}{\partial y^2} - \frac{\partial \bar{Q}}{\partial y} \quad (5)$$

where:

X is the stream function for the mean meridional circulation,

(assumed to be zero at the equator)

M is the momentum flux,

B is a measure of the northward eddy heat flux,

$f_0$  the mean coriolis parameter for the domain,

Q is the vertically integrated diabatic heating.



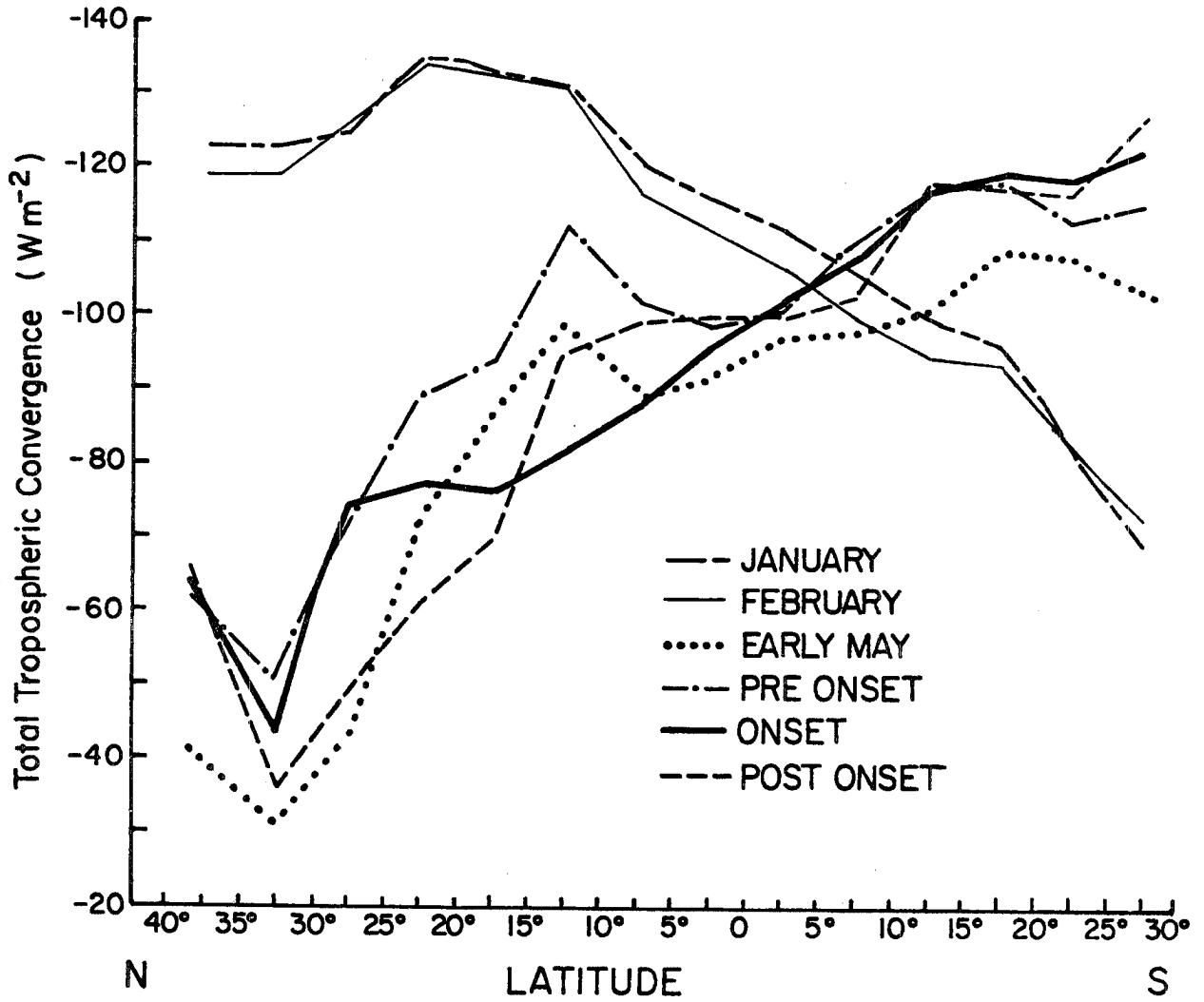


Figure 22. Latitudinal mean (averaged over 5° longitude) total tropospheric convergence for the six periods.

The left hand side is proportional to  $-X$  (Holton, 1979), and thus

$$X \propto \frac{\partial \text{TTC}_L}{\partial y}$$

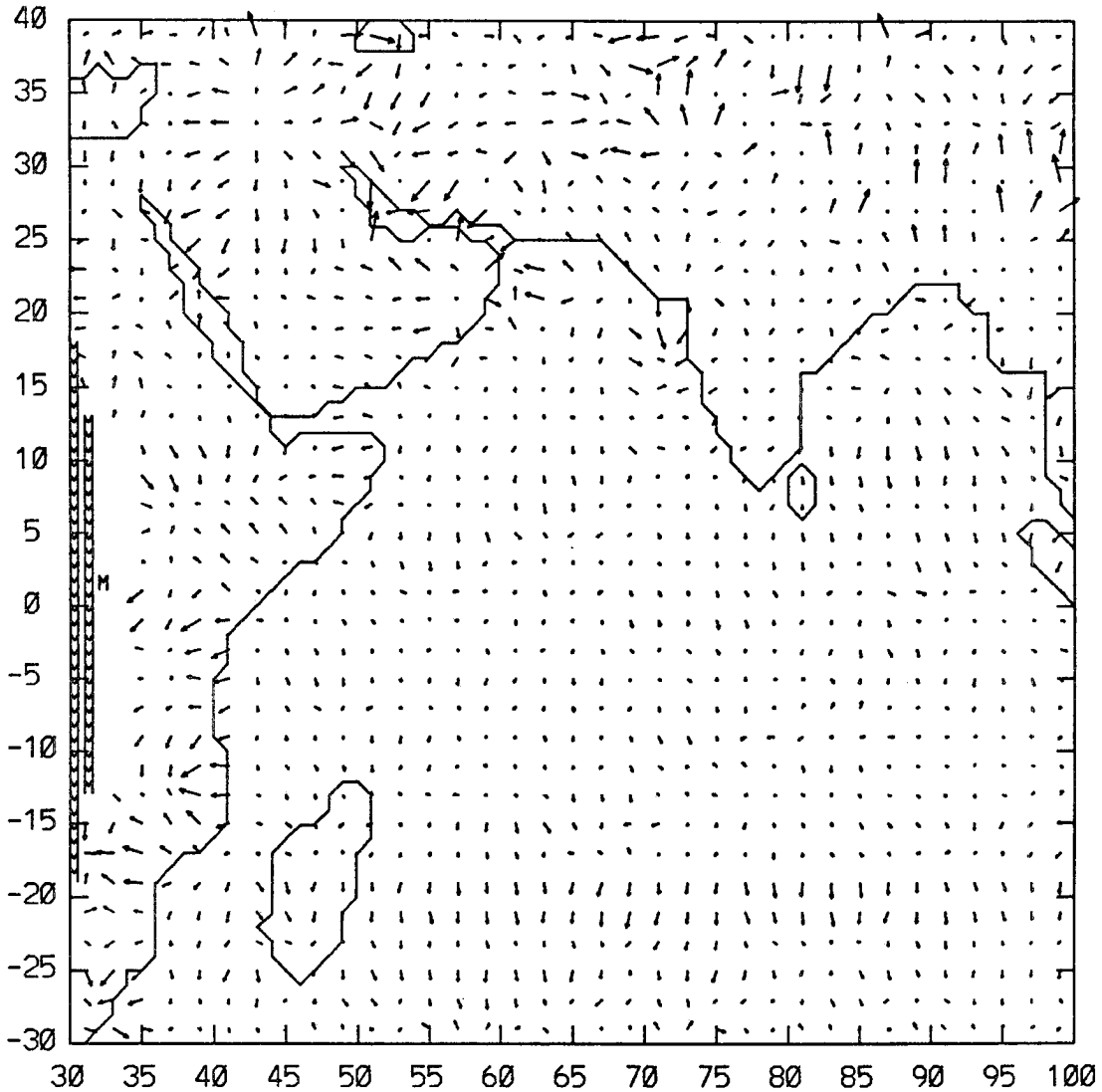
In the northern Hemisphere a negative  $X$  is associated with rising motion to the south and sinking motions to the north (e.g. Hadley cell circulation). During the early May, pre-onset, onset and post-onset periods,  $\frac{\partial \text{TTC}_L}{\partial y} > 0$  (figure 22) thus driving a meridional circulation with rising motion in the north and sinking motion to the south. This is the type of circulation associated with the active monsoon. This radiative induced circulation will be smallest during the onset period when the zonal gradients of  $\text{TTC}_L$  are smallest.

While the above model is somewhat simplistic, it demonstrates that the gradients (horizontal and vertical) of diabatic heating contribute to the circulation. This was also shown by Krishnamurti and Ramanathan (1982) who found that the monsoon onset was sensitive to the initially imposed fields of total differential heating ( $-\frac{\partial}{\partial p} \nabla Q$ ). The orientation of the differential heating determined the evolution of the divergent circulation, which, with the proper orientation of the nondivergent and irrotational motion fields, could be effective in generating kinetic energy of nondivergent motions leading to an onset. The total diabatic heating term is composed of condensational heating ( $Q_C$ ), radiative heating ( $Q_R$ ) and sensible heat fluxes ( $Q_S$ ). In the presence of active convection the total differential heating field will be dominated by  $\nabla Q_C$ . Over the cloud free regions (e.g. the desert regions and the northern Arabian Sea) the orientation of the  $\nabla Q$  fields will be determined by  $\nabla Q_S$  and  $\nabla Q_R$ . Figure 23 displays the vertically integrated radiative differential heating fields ( $\nabla \text{TTC} \text{ Wm}^{-2} \text{ Km}^{-1}$ ) for the six periods, for the region  $0^\circ$  to  $30^\circ\text{N}$ . During January and February the  $\nabla \text{TTC}$  tends to be uniform,

# 24 HOUR TROPOSPHERIC CONVERGENCE

JANUARY

GOES-1



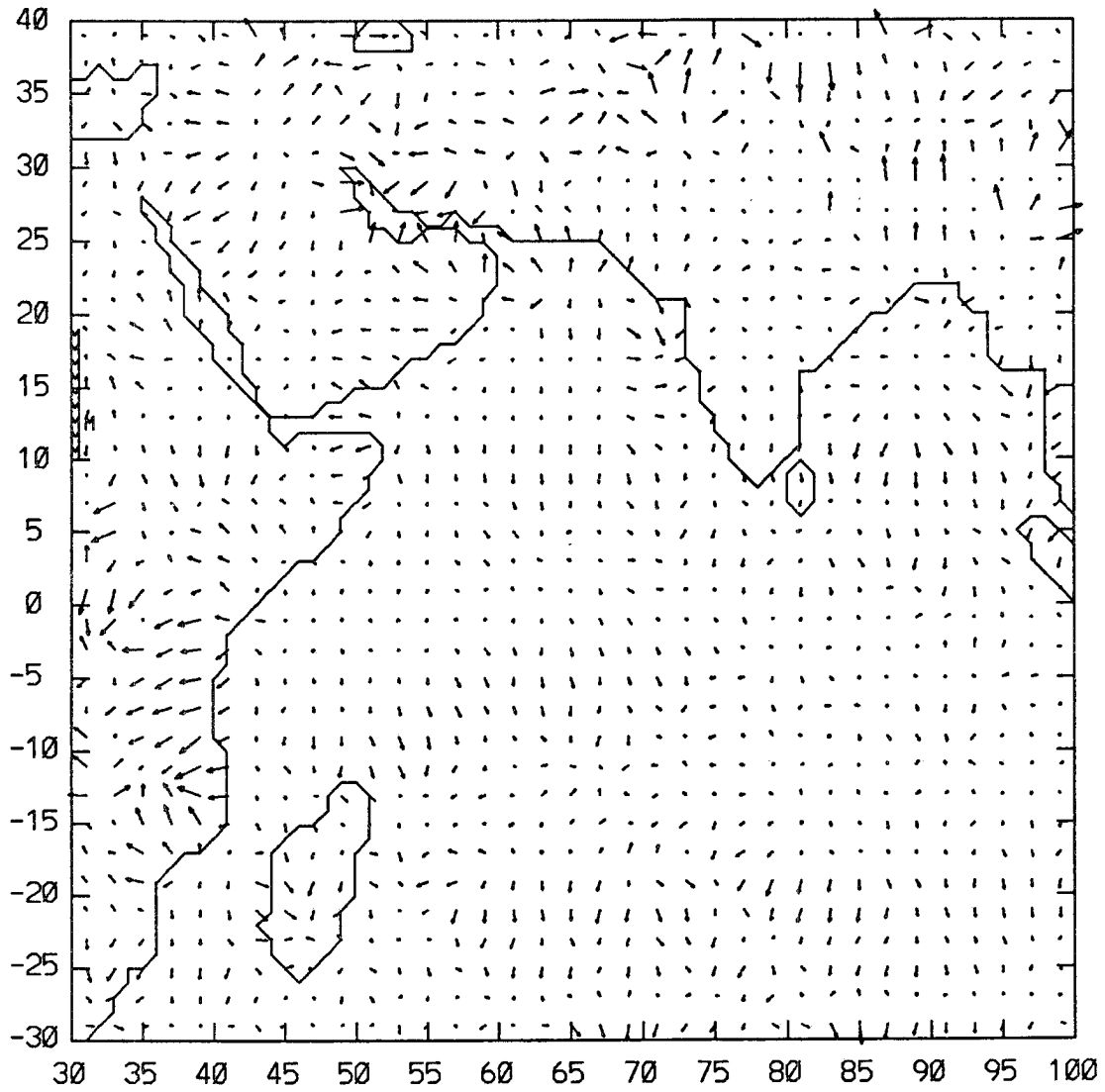
0.100E+00  
MAXIMUM VECTOR

Figure 23. Vertically integrated radiative differential heating fields for the six periods, for the region 0° to 30°N and 30°E to 100°E. Units are  $W m^{-2} km^{-1}$ .

# 24 HOUR TROPOSPHERIC CONVERGENCE

FEBUARY

GOES-1



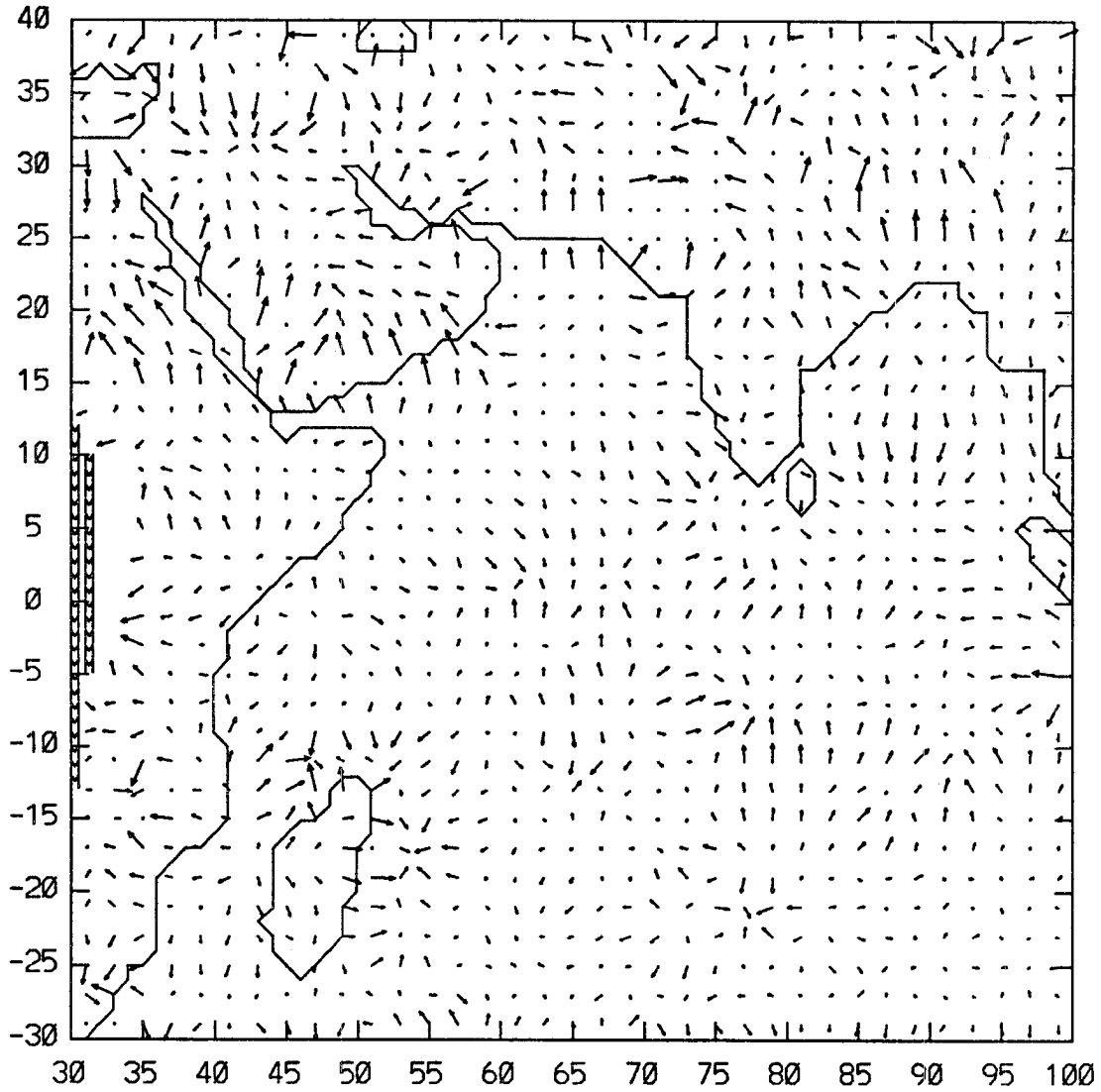
0.100E+00  
MAXIMUM VECTOR

Figure 23. Continued

# 24 HOUR TROPOSPHERIC CONVERGENCE

EARLY MAY

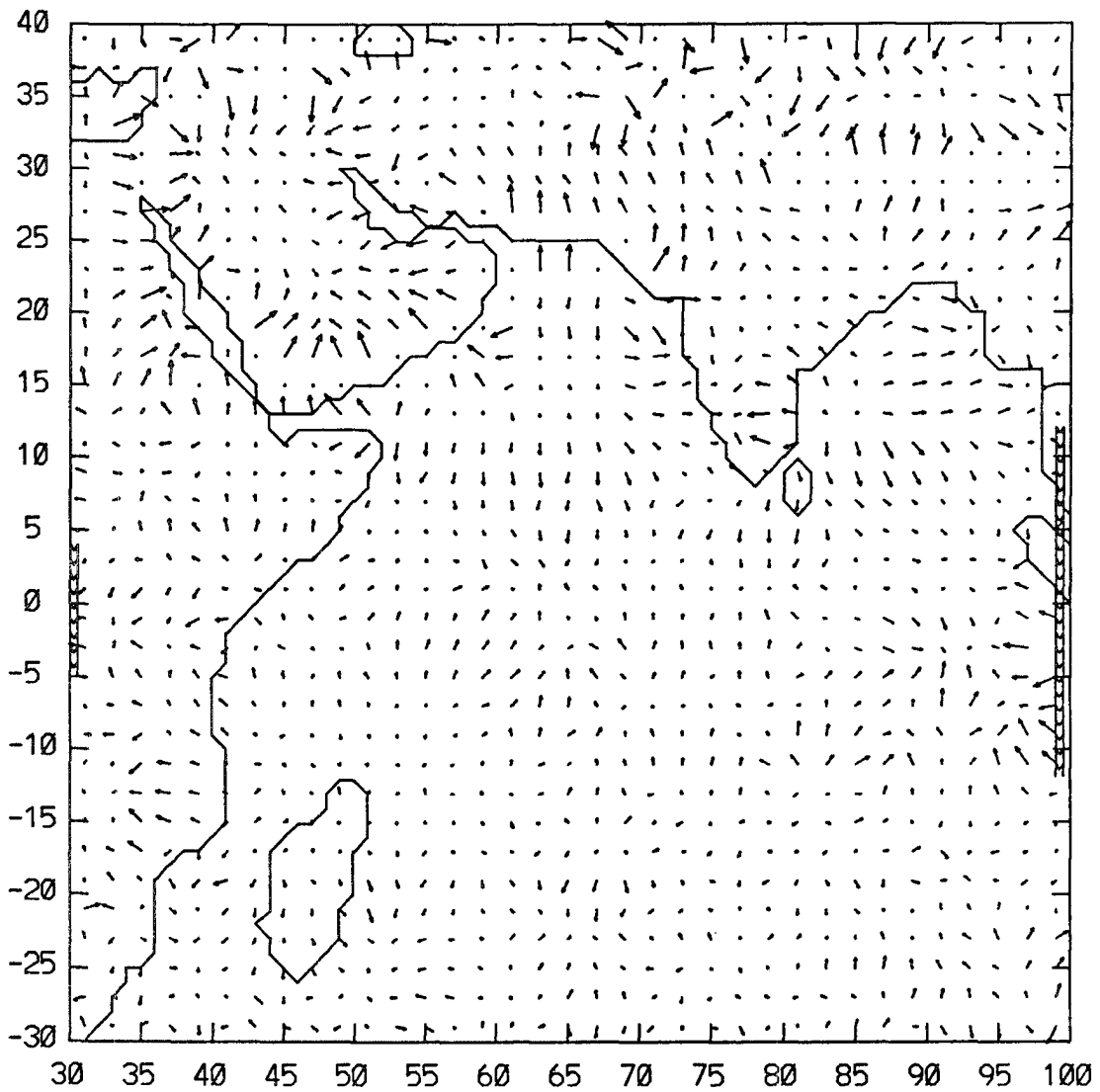
GOES-1



0.100E+00  
MAXIMUM VECTOR

Figure 23. Continued

24 HOUR  
TROPOSPHERIC CONVERGENCE  
PRE-ONSET  
GOES-1



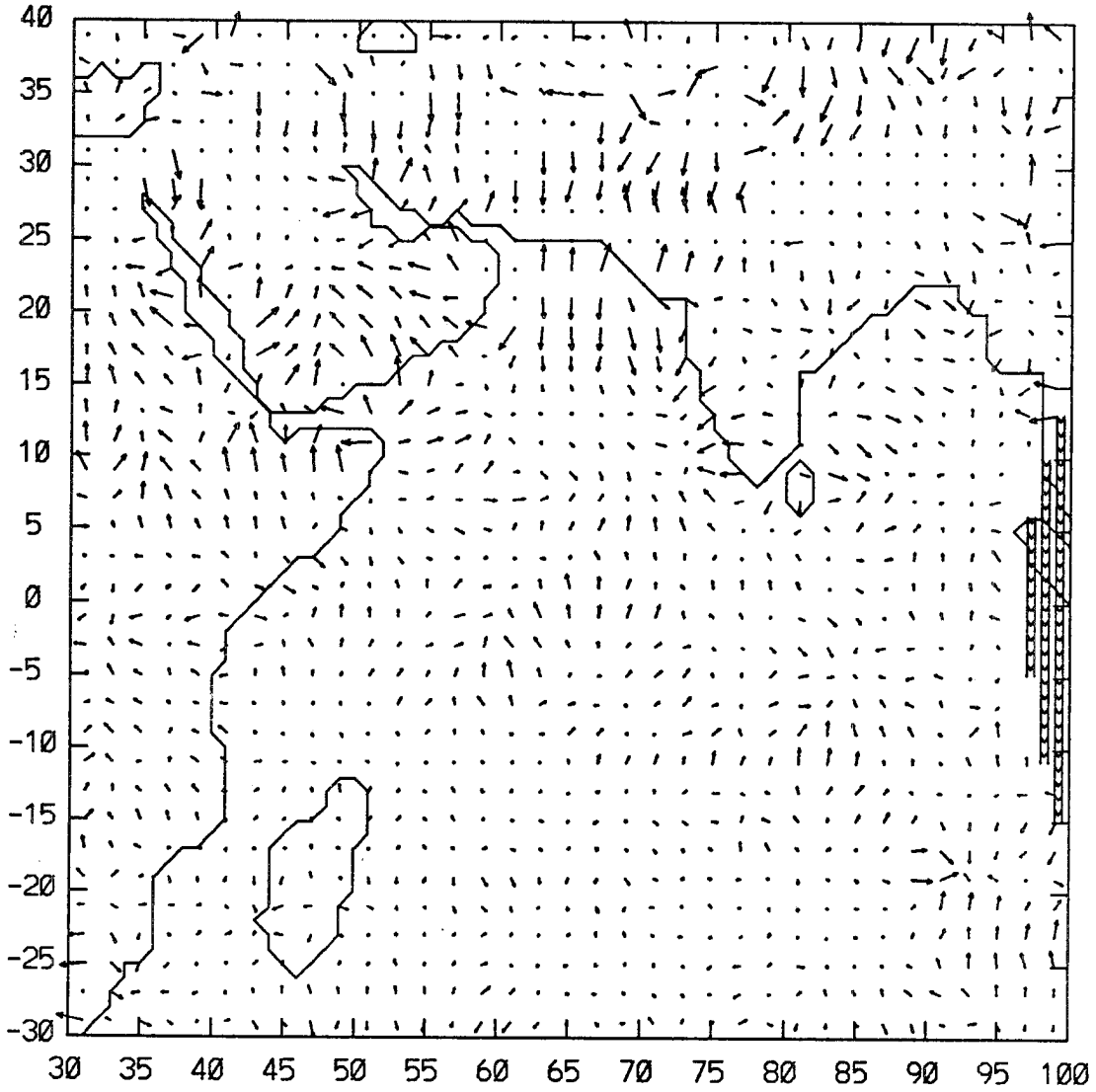
0.100E+00  
MAXIMUM VECTOR

Figure 23. Continued

# 24 HOUR TROPOSPHERIC CONVERGENCE

ONSET

GOES-1

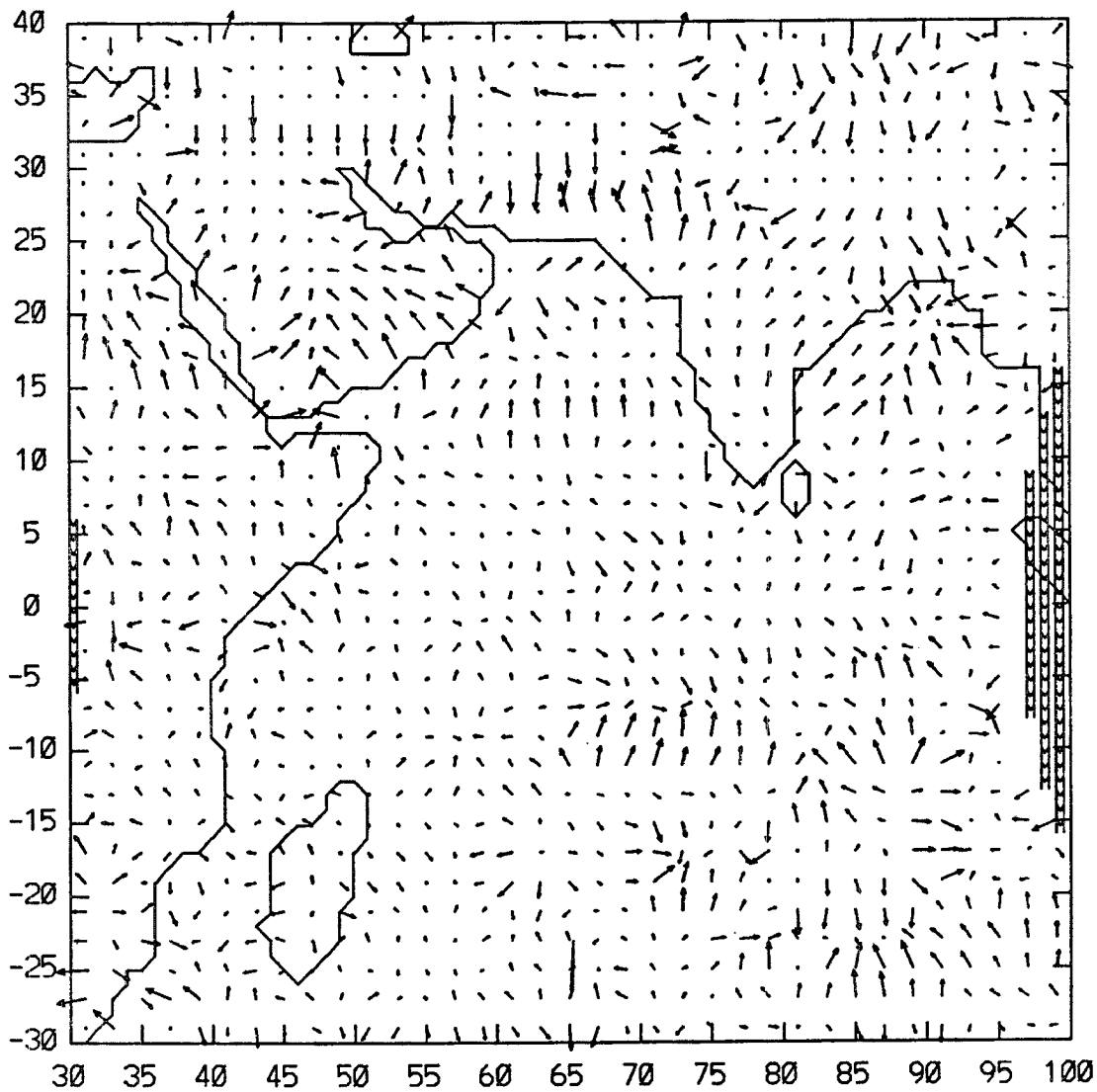


0.100E+00  
MAXIMUM VECTOR

Figure 23. Continued

# 24 HOUR TROPOSPHERIC CONVERGENCE POST-ONSET

GOES-1



0.100E+00  
MAXIMUM VECTOR

Figure 23. Continued

with largest values associated with coastal regions. The next four periods display large variations in the differential radiative heating field. In the early-May through post-onset periods  $\nabla$  TTC points toward the northern regions of the Saudi Arabian Peninsula. These gradients are largely due to the presence of a dust layer. During the early May and pre-onset periods  $\nabla$  TTC is oriented from the eastern Arabian Sea toward the Indian subcontinent; this differential heating field is reversed during the onset period due to the presence of the onset vortex in the southeastern Arabian Sea. The Bay of Bengal also shows reversals in the orientation and magnitude of  $\nabla$  TTC during these four periods in association with changing cloud amounts.

### 3.1c Vertical radiative heating profiles

The vertical structure of  $Q_R$  is an important parameter in assessing the coupling between radiative and dynamical processes. In the previous section we considered the distribution of TTC in order to present an overview of the radiative fields. To illustrate the changes in the vertical structure of the radiative heating, figure 24 presents tropospheric radiative heating profiles averaged over a  $5^\circ$  latitude by  $5^\circ$  longitude region for four areas; northwest Arabian Sea ( $25^\circ\text{N } 60^\circ\text{E}$  to  $20^\circ\text{N } 65^\circ\text{E}$ ), eastern Arabian Sea ( $15^\circ\text{N } 70^\circ\text{E}$  to  $10^\circ\text{N } 75^\circ\text{E}$ ), central India ( $25^\circ\text{N } 75^\circ\text{E}$  to  $20^\circ\text{N } 80^\circ\text{E}$ ) and the northwest Bay of Bengal ( $20^\circ\text{N } 85^\circ\text{E}$  to  $15^\circ\text{N } 90^\circ\text{E}$ ). Figure 25 depicts the changes in the regionally averaged cloud top profiles for the four phases. All the radiative heating profiles display a minimum cooling in the mid-troposphere which results principally from the vertical distribution of water vapor. The early May and pre-onset phases of the northwest Arabian Sea case are largely cloud free, and the differences in the radiative profiles result from less water vapor in the early May period. During the onset phase the increased cloud cover suppresses

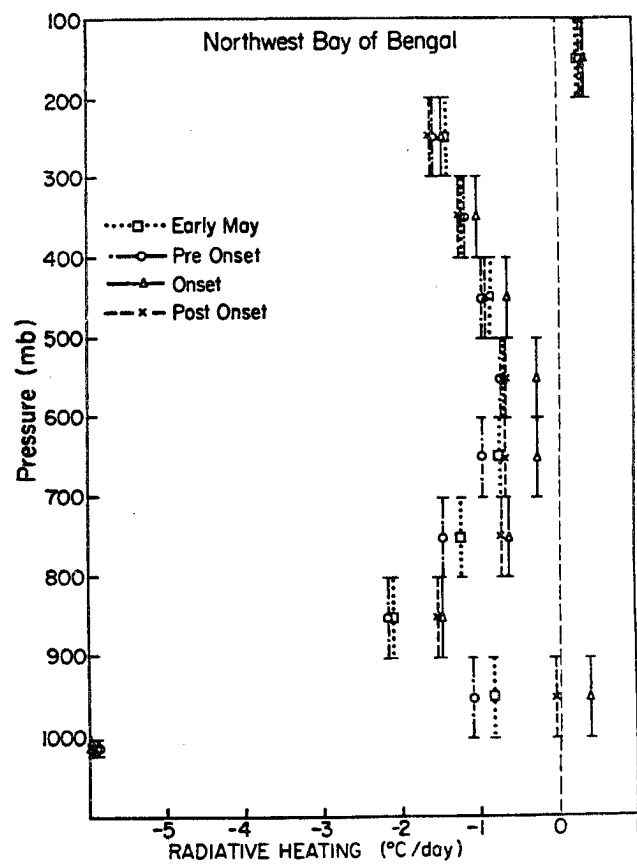
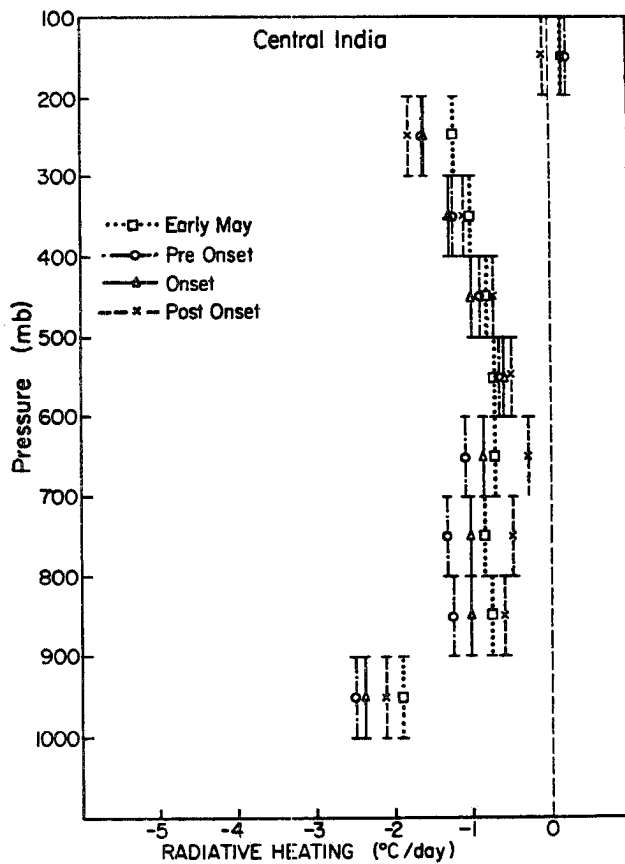
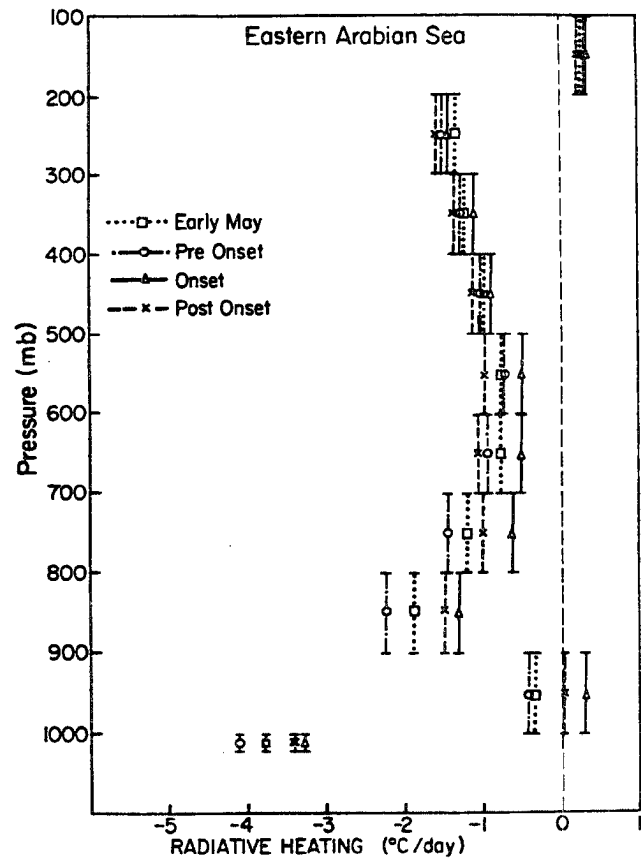
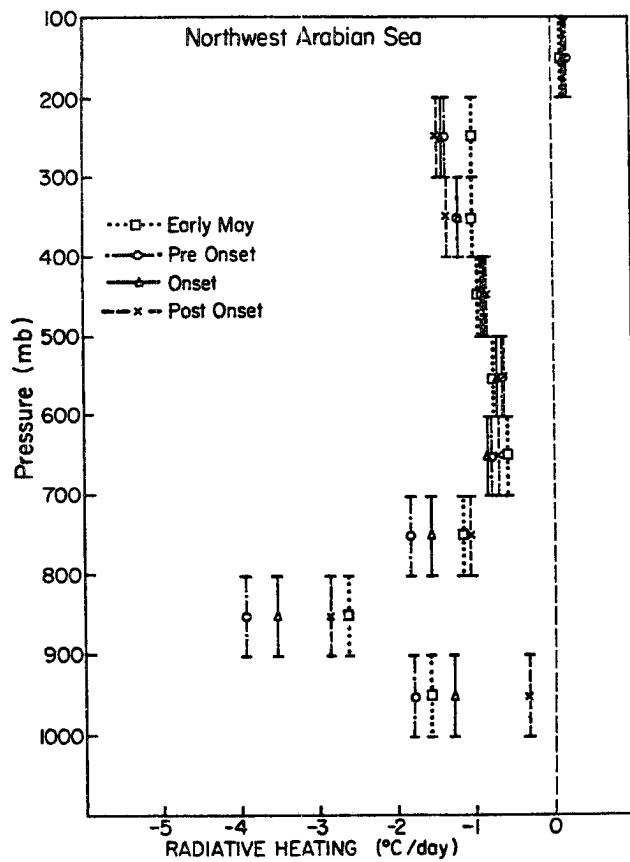


Figure 24. Radiative heating profiles averaged over a  $5^\circ$  latitude by  $5^\circ$  longitude region for four areas; a) northwest Arabian Sea ( $25^\circ\text{N}$   $60^\circ\text{E}$  to  $20^\circ\text{N}$   $65^\circ\text{E}$ ), b) eastern Arabian Sea ( $15^\circ\text{N}$   $70^\circ\text{E}$  to  $10^\circ\text{N}$   $75^\circ\text{E}$ ), c) central India ( $25^\circ\text{N}$   $75^\circ\text{E}$  to  $20^\circ\text{N}$   $80^\circ\text{E}$ ) and d) northwest Bay of Bengal ( $20^\circ\text{N}$   $85^\circ\text{E}$  to  $15^\circ\text{N}$   $90^\circ\text{E}$ ).

### CLOUD TOP PRESSURE DISTRIBUTION

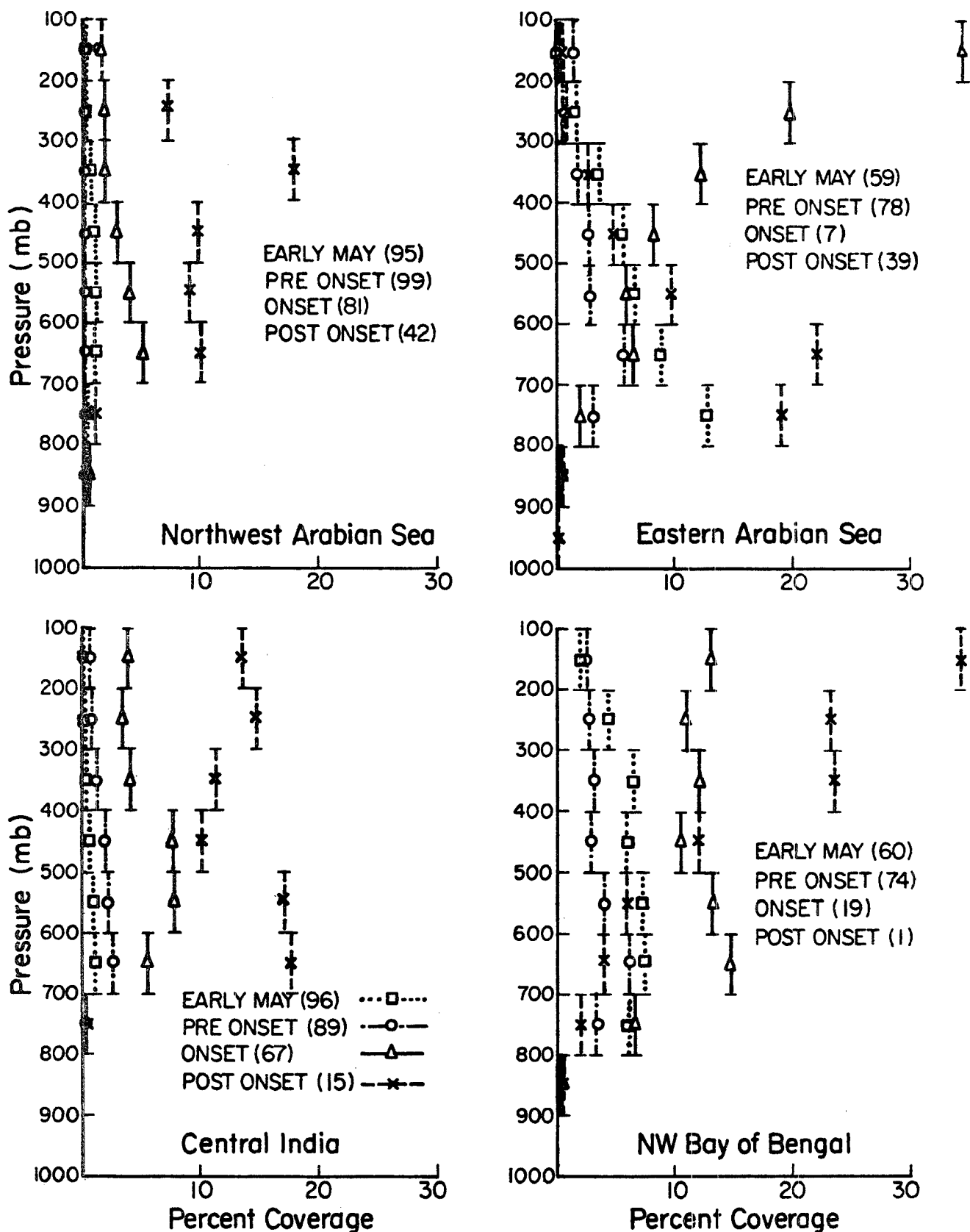


Figure 25. Regionally averaged cloud top pressure profiles for the four phases discussed in the text. The regions are; a) northwest Arabian Sea (25°N 60°E to 20°N 65°E), b) eastern Arabian Sea (15°N 70°E to 10°N 75°E), c) central India (25°N 75°E to 20°N 80°E) and d) northwest Bay of Bengal (20°N 85°E to 15°N 90°E). The periods are Early May (dotted line); Pre-onset (dash-dot line); onset (solid line); and Post-onset (dashed line). Values in parenthesis are the percentage of cloud free areas.

(compared to the pre-onset phase) the radiative cooling below 700 mb. During the post-onset phase the increase in mid- and upper-tropospheric cloud amount results in an increased cooling of the upper troposphere and a further reduction of the radiative cooling in the lower troposphere.

For the eastern Arabian Sea region, the early May period has more cloud than the pre-onset period; as a result the latter period shows a larger lower tropospheric cooling. During the onset phase there are large amounts of upper tropospheric cloud which reduce the total radiative energy loss of the atmosphere. In the post-onset phase the maximum in upper level clouds is replaced with a maximum in the 600-800 mb level; this results in an increase in the middle and upper troposphere radiative cooling.

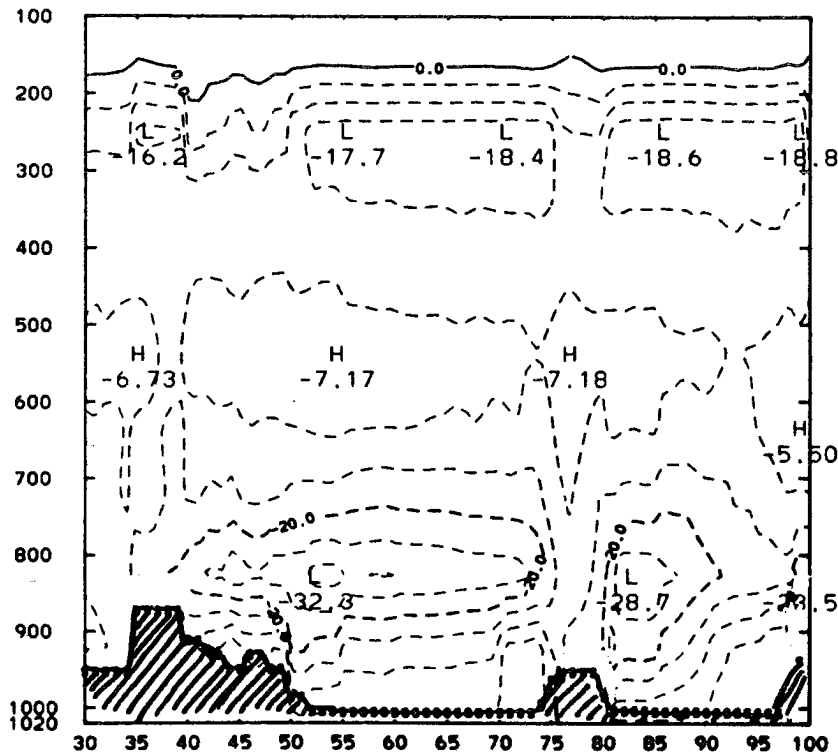
The difference in the pre-onset and early May heating rates for central India are primarily due to the drier, early May period. The increased cloud cover during the onset phase, with maximum cloud cover in the 400-600 mb level, results in smaller cooling below 500 mb and slightly increased cooling above 500 mb when compared with the pre-onset phase. The bimodal cloud structure for this region in the post-onset period results in a minimum radiative energy loss below 500 mb and a maximum loss above 300 mb.

For the northwest Bay of Bengal, minimum cloud coverage is associated with the pre-onset period as is maximum tropospheric cooling. The large increase in upper tropospheric cloud during the onset phase suppresses the total tropospheric radiative energy losses. During the post-onset phase the upper tropospheric cloud maximum is replaced with a maximum in the 600-700 mb layer. This is reflected in the heating profiles by an increased cooling above 700 mb.

A zonal cross-section of tropospheric radiative convergence along the latitude band  $10^{\circ}$ - $15^{\circ}$  N is depicted in the left hand panels of figure 26 for

24 HOUR  
TROPOSPHERIC CONVERGENCE  
PRE-ONSET

10-15N



24 HOUR  
CLOUD COVER  
PRE-ONSET

10-15N

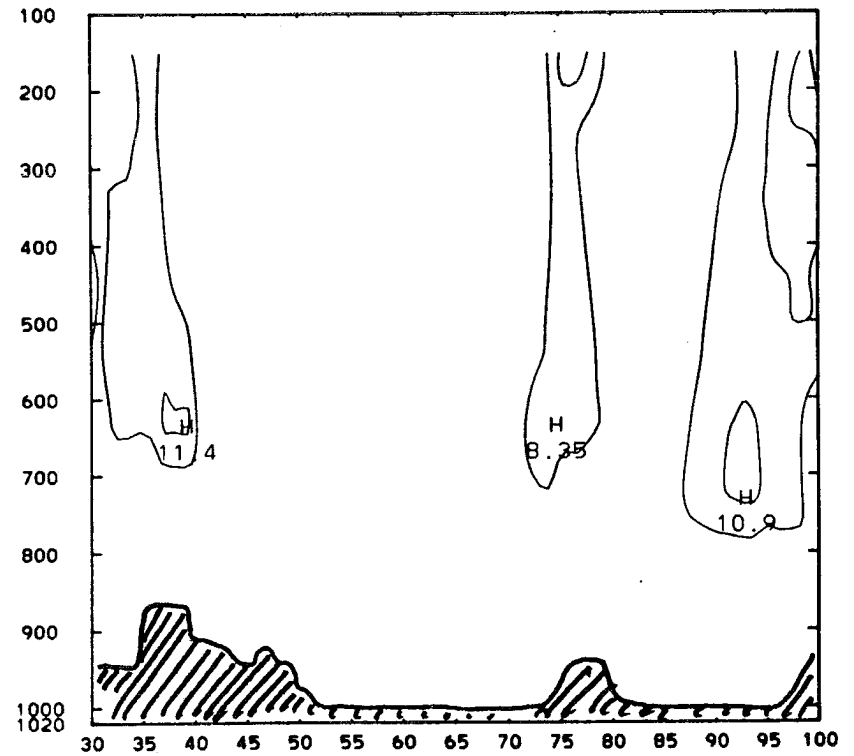
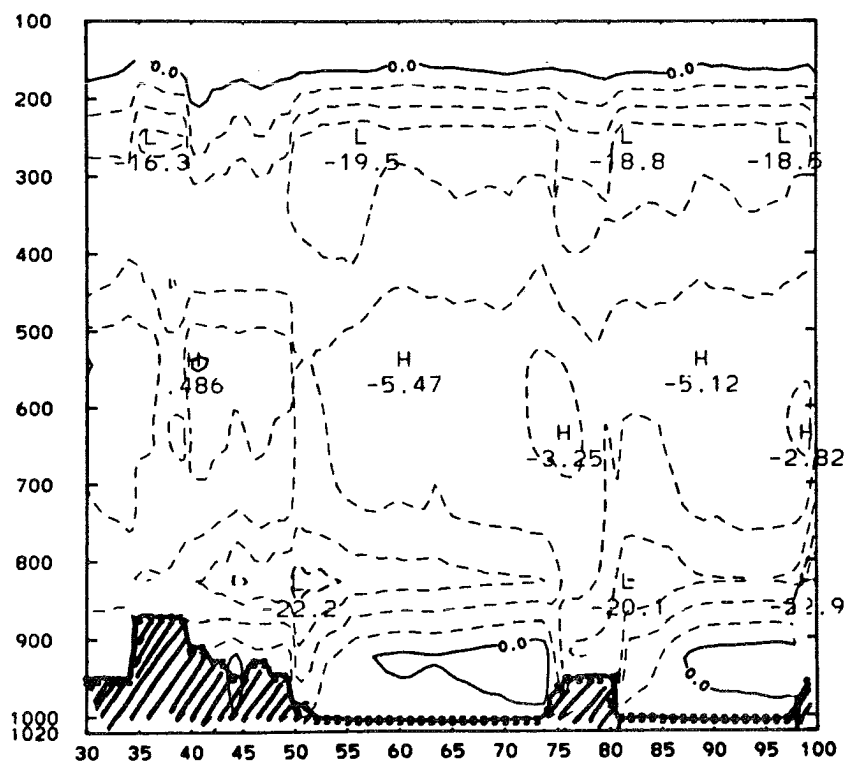


Figure 26. Zonal cross-section of tropospheric radiative convergence along the latitude band 10°-15° N (left hand panels) for the a) pre-onset, b) onset and c) post-onset phases respectively. The right hand panels display a similar cross-section of the vertical distribution of cloud top pressure.

24 HOUR  
TROPOSPHERIC CONVERGENCE

ONSET

10-15N



24 HOUR  
CLOUD COVER

ONSET

10-15N

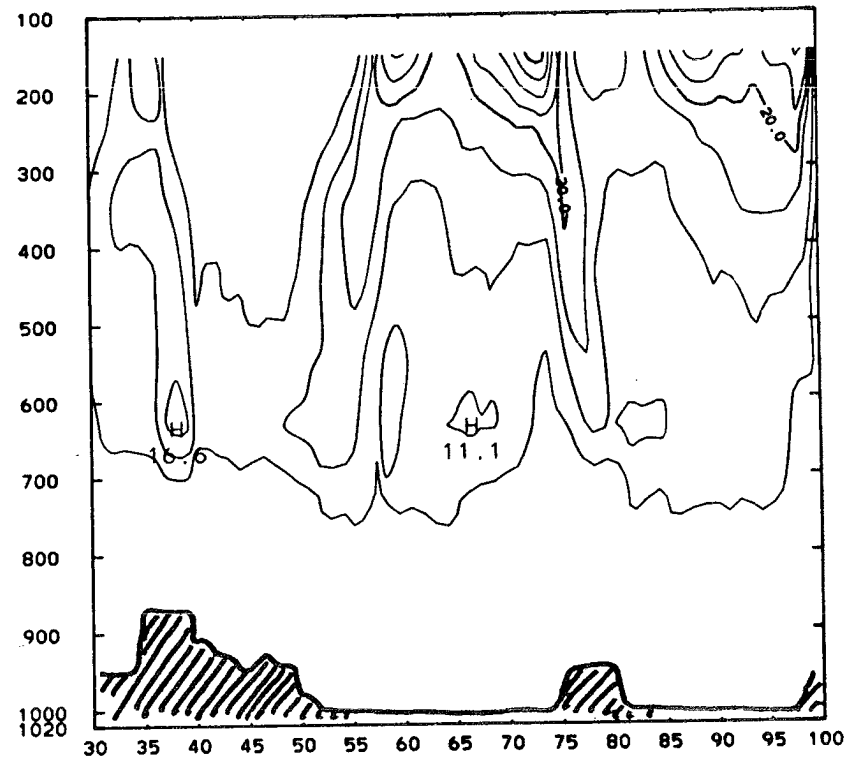
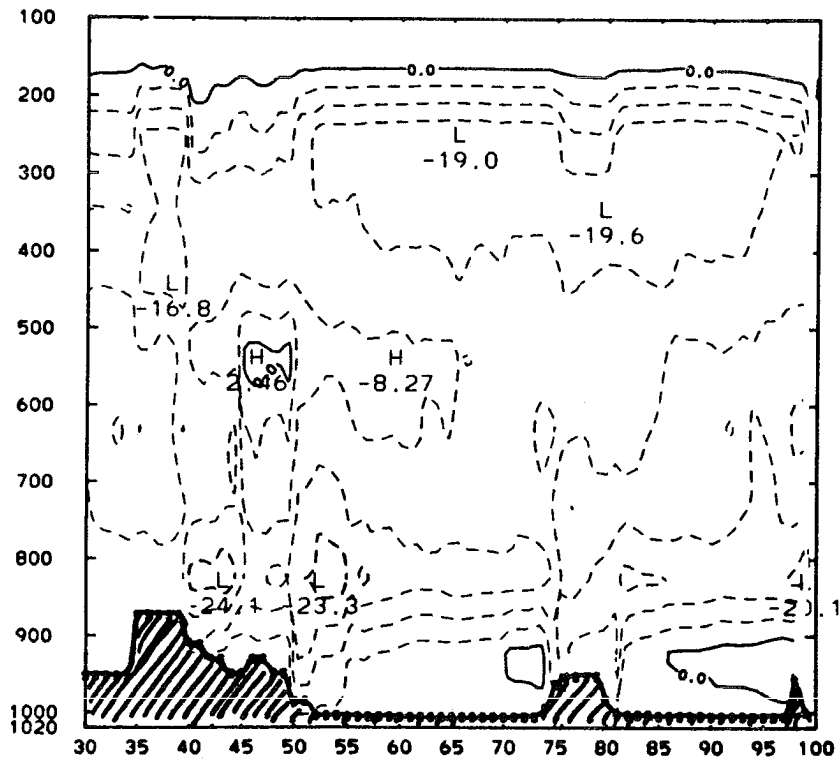


Figure 26. Continued

24 HOUR  
TROPOSPHERIC CONVERGENCE  
POST-ONSET

10-15N



24 HOUR  
CLOUD COVER  
POST-ONSET

10-15N

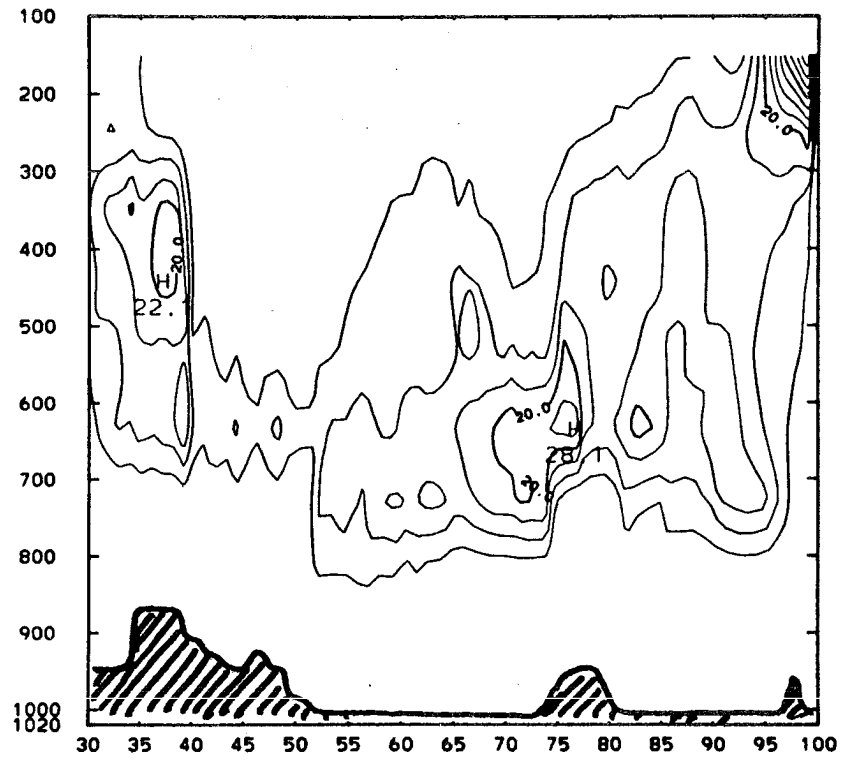


Figure 26. Continued

the pre-onset, onset and post-onset phases respectively. The right hand panels display a similar cross-section of the vertical distribution of cloud top pressure. In the pre-onset phase the largest latitudinal differences occur below 700 mb, where the Arabian Sea and Bay of Bengal have regions of maximum cooling. Differences in radiative convergence in the middle and upper levels of the atmosphere tend to be small. During the onset phase the large increase in upper level clouds over the Arabian Sea and Bay of Bengal results in a small net convergence below 900 mb due to the assumed cloud base distribution in conjunction with low level moisture. Again the maximum gradients occur near 800 mb, though the magnitude of the cooling is less. The cloud cover also reduces the radiative cooling in the middle levels of the atmosphere while slightly increasing the cooling in the upper levels. In the post-onset phase, the cloud tops are generally located in the middle levels of the atmosphere and thus enhance the meridional gradients in radiative heating at these levels. The small maximum convergence in the 500-600 mb layer over eastern Africa results from the presence of a dust layer.

### 3.1d Surface net radiative fluxes

The net surface radiation budget is a major component affecting the land and ocean surface heating, and as a result may indirectly affect monsoon variability. For example, Sikka and Gadgil (1980) observed a low frequency variability over India in the 'maximum cloudiness zone' (MCZ), which they note is nearly coincident with the 700 mb trough. Sikka and Gadgil attribute this variability in the MCZ, as well as its northward migration, to variations of surface radiative heating produced by the cloudiness gradient associated with the MCZ and surrounding clear regions. Their hypothesis is supported by the model results of Webster (1983) which suggest that the northward migrations of

the MCZ result from changes in the surface sensible heating ahead of the convective cloud system.

Before discussing the derived surface radiative fluxes it is worthwhile to mention the parameters which control these fluxes, and the assumptions made in this study. In the case of clear sky conditions the controlling parameters are the distributions of absorbing gases and the atmospheric temperature structure (which determine the downward fluxes), and the surface's albedo, emittance and temperature (which largely determine the upward fluxes). Satellite observations, data from the field phase of MONEX and the FGGE level IIIb data set represent the best large scale depictions of temperature, moisture and surface radiative properties ever assembled over the MONEX region. Thus accurate input parameters to the radiative transfer routine are available for the cloud free atmosphere. Surface radiative energy budgets are particularly difficult to derive under cloudy conditions. Shortwave radiative fluxes at the surface have been inferred from satellite measurements (e.g., Tarpley 1979, Gautier et al. 1980 and Gautier 1984). The success of these techniques is in large part a result of the fact that surface insolation is largely a function of the total water path, and is more or less independent of the cloud vertical distribution. Satellite techniques for estimating insolation either account for clouds statistically or assume cloud radiative properties. In the present study, satellite observations are used to derive cloud amount and the surface SW flux is calculated assuming the cloud water contents shown in figure 3. Estimates of the net LW surface flux is very difficult as there is a strong dependence on cloud base pressure (Fung et al. 1984). Satellite estimates of LW net flux must include some relationship between effective cloud base and cloud top temperature. In the present study a limiting value of the lifted condensation level pressure is placed on cloud

base, and a statistical distribution of cloud base pressure, which is a function of cloud top pressure, is assigned according to the work of Cox and Griffith (1979).

As there is no data available for direct verification of the surface radiative energy budgets ( $Q_{\text{Rsfc}}$ ), estimates of their accuracy is reduced to comparisons with other studies. Even the comparisons themselves are difficult to perform as different studies employ very different techniques and often have different spacial and temporal scales. Until recently, estimates of  $Q_{\text{Rsfc}}$  for large geographic areas were based on empirical formulae. While these types of analysis may produce qualitatively correct patterns of  $Q_{\text{Rsfc}}$ , errors in the absolute values may be large. The spatial characteristic of the  $Q_{\text{Rsfc}}$  in the present study are very similar to those derived (based on empirical formulae) by Ramage et al. (1972) for the International Indian Ocean Expedition (IIOE), though differences in magnitude are quite large. As an example, the results of the present study are approximately  $40 \text{ W m}^{-2}$  less than the IIOE results for the cloud free northwestern Arabian Sea. More recently Gautier (1986) employed satellite observations to estimate the net shortwave radiation at the surface (NSW) for the summer MONEX period. The NSW of the present study compares favorably with the results of Gautier, not only in the location of maximae and minimae but also in absolute magnitude. For example, over the Arabian Sea in the pre-onset period, Gautier has a maximum NSW of about  $320 \text{ W m}^{-2}$ . The present study has a maximum in the same geographic region with a magnitude of approximately  $310 \text{ W m}^{-2}$ . During the pre-onset period of the present study a minimum in NSW over the Arabian Sea of approximately  $160 \text{ W m}^{-2}$  is observed, compared to a less than  $150 \text{ W m}^{-2}$  minimum reported by Gautier. We know of no study for which our estimates of the net longwave radiation at the surface can be compared with; thus it is

difficult to gage the accuracy of the  $Q_{RSfc}$ . However the patterns of  $Q_{RSfc}$  are probably realistic and the magnitudes are consistent, from an energetic point of view, with the derived atmospheric radiative energy budgets presented previously.

Figure 27 depicts estimates of the surface net radiative flux for the six periods. Contour intervals are  $50 \text{ W m}^{-2}$  with positive values representing a net surface gain. The January fluxes tend to a zonal distribution with maximum surface radiative gains of approximately  $215 \text{ Wm}^{-2}$  over the southern Indian Ocean. The net gain decreases northward, with net losses over the Himalaya. These results are in agreement with Katayama (1967), though his zero line is further north. The February phase displays features similar to the January surface budget.

During the early May phase the maximum surface gain is in the northern Arabian Sea, where clear skies allow a large SW downward flux and the small albedoes result in a large net SW energy gain. On the other hand the SE Indian Ocean displays a net surface loss. This results from a lower insolation due to the sun-earth geometry as well as a strong diurnal variation in total cloud amount (see appendix). The maximum in total cloud during the daylight hours reduces the net SW energy gain such that the longwave energy loss dominates. During the pre-onset phase a more cellular pattern in the surface radiation budget begins to emerge, with maximae associated with cloud free oceanic regions and minimae with continental and/or cloudy regions. The maximum surface energy gain is the Arabian Sea region, in agreement with Budyko (1955) and IIOE. A relative maximum is also observed over the western Bay of Bengal, with relative minimae over the Saudia Arabian and Indian peninsulas. In the onset phase the northern Arabian Sea still exhibits a maximum net surface flux, though the magnitude is reduced compared to the

# SURFACE NET FLUX

JANUARY

GOES-1

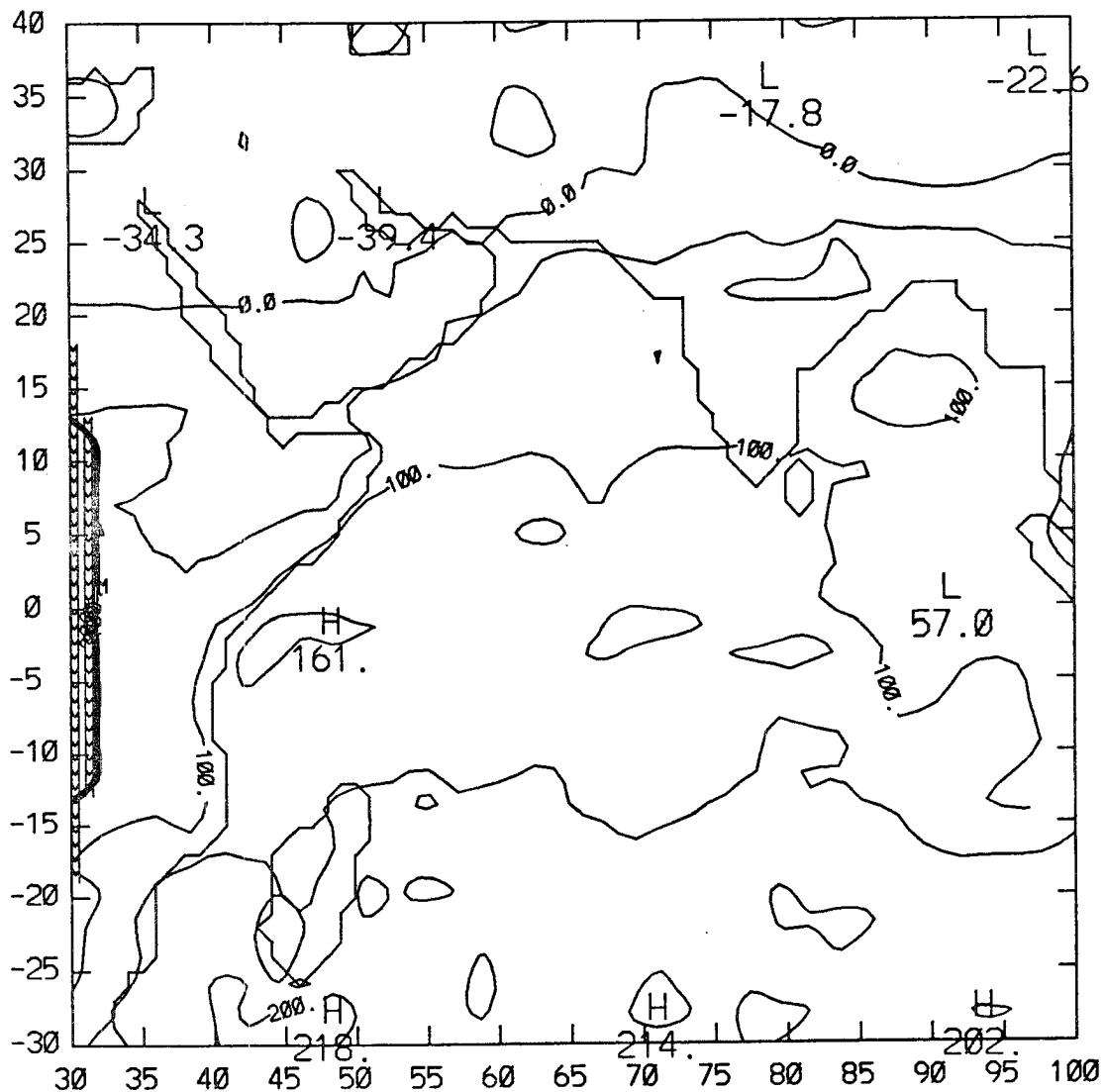


Figure 27. Surface net radiative flux for the six phases of the 1979 summer monsoon. Contour intervals are  $50 Wm^{-2}$  with positive values representing a net surface gain.

# SURFACE NET FLUX

FEBUARY

GOES-1

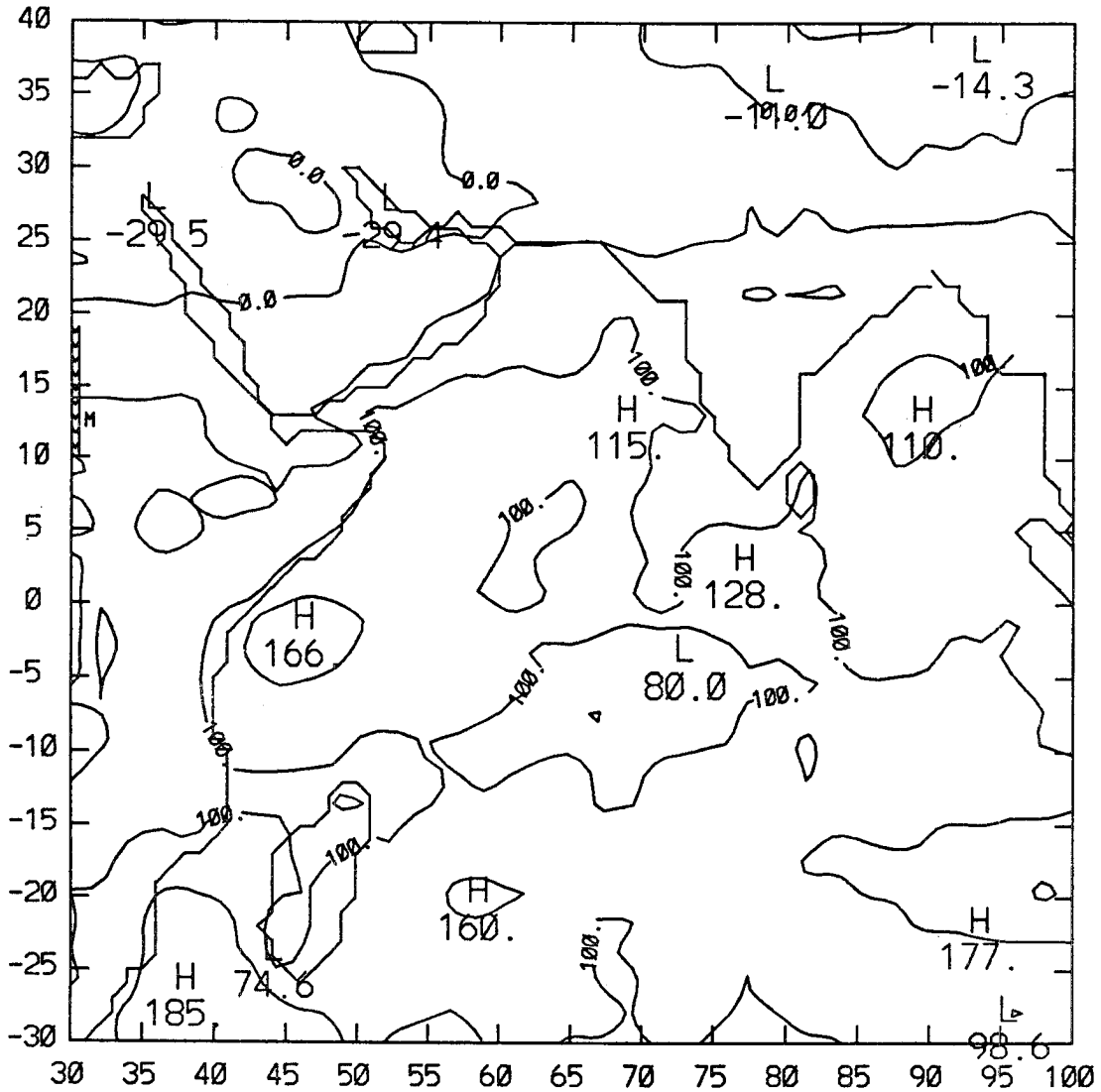


Figure 27. Continued

# SURFACE NET FLUX

EARLY MAY

GOES-1

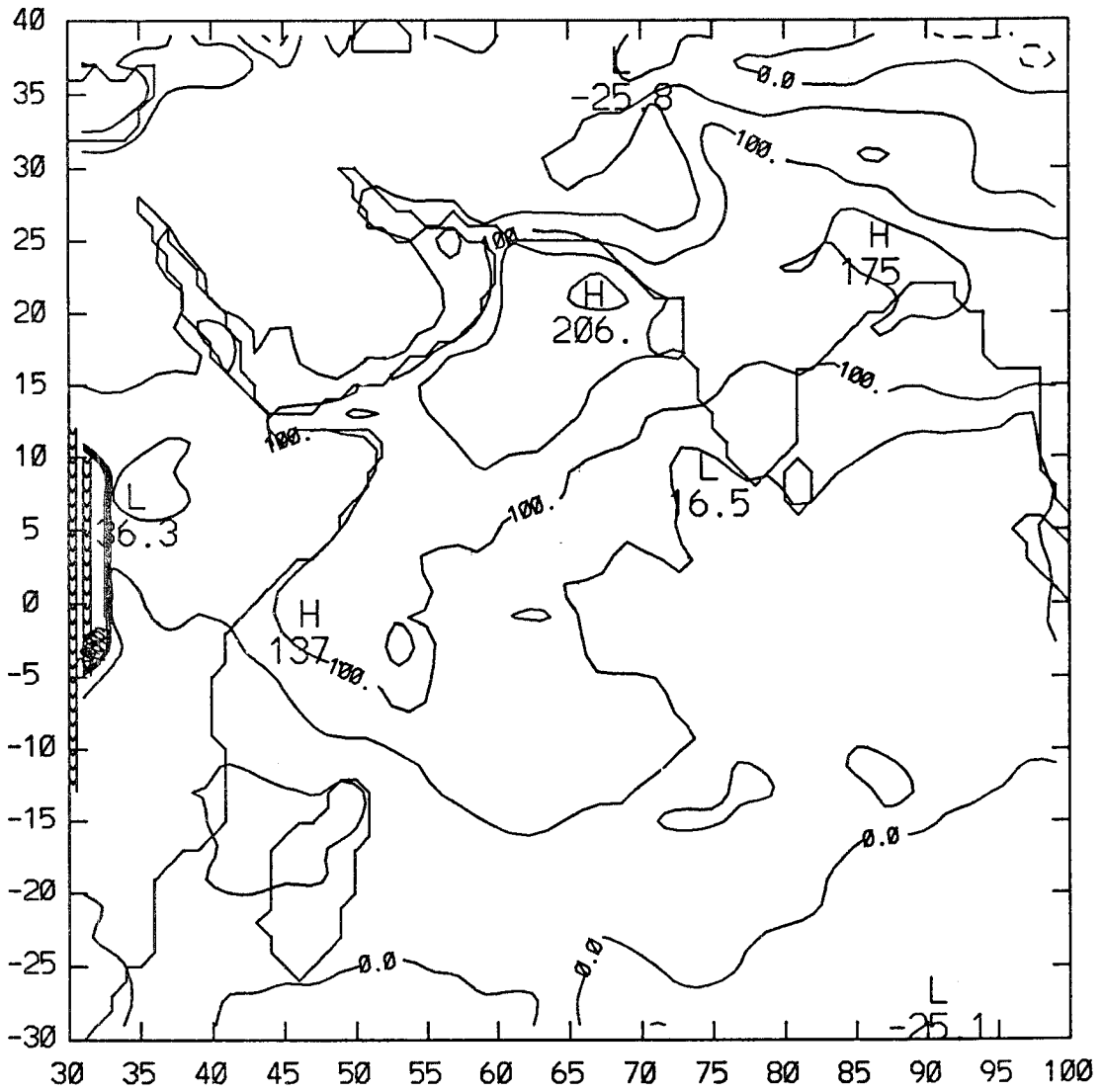


Figure 27. Continued

# SURFACE NET FLUX

PRE-ONSET

GOES-1

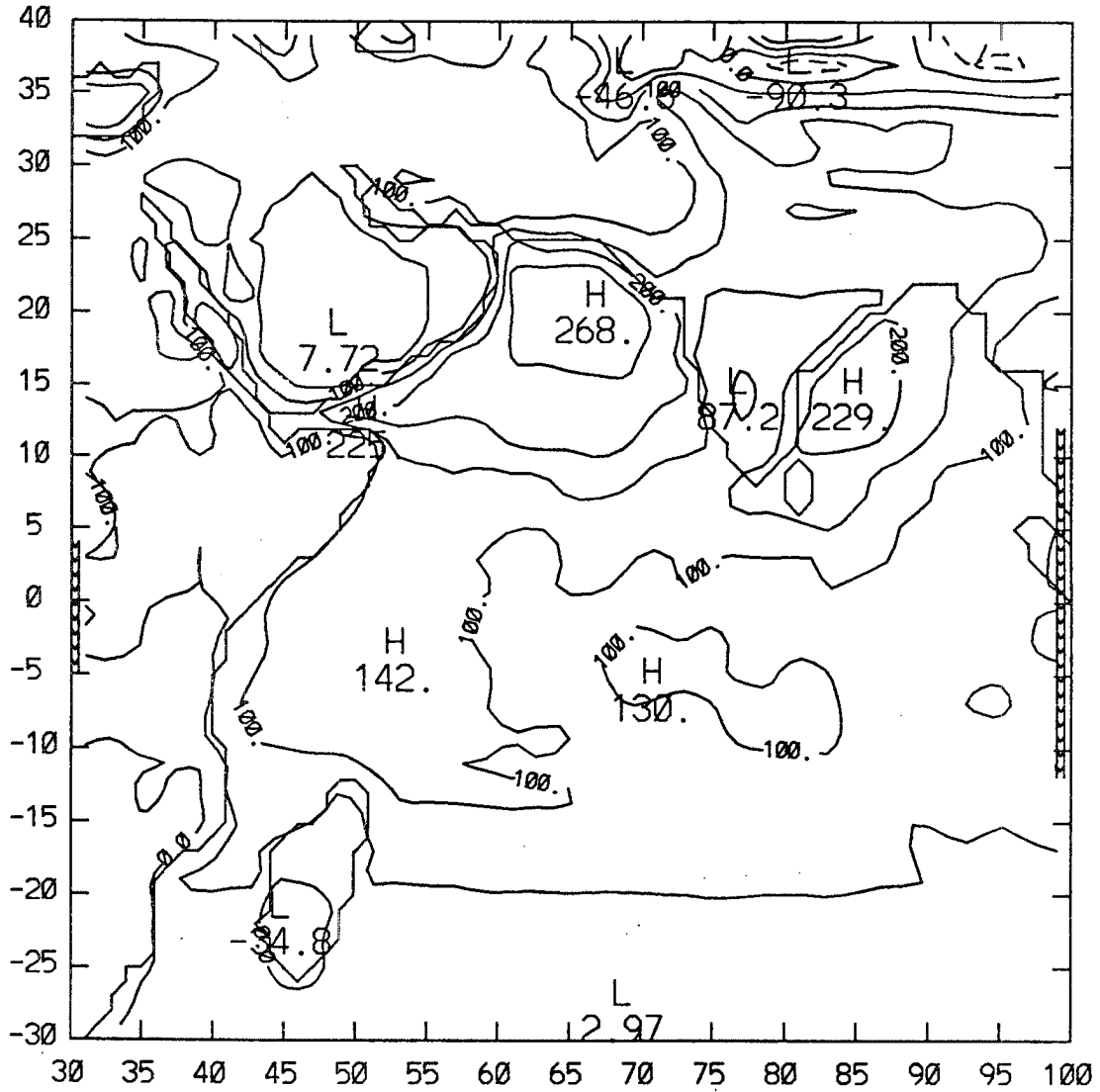


Figure 27. Continued



# SURFACE NET FLUX

POST-ONSET

GOES-1

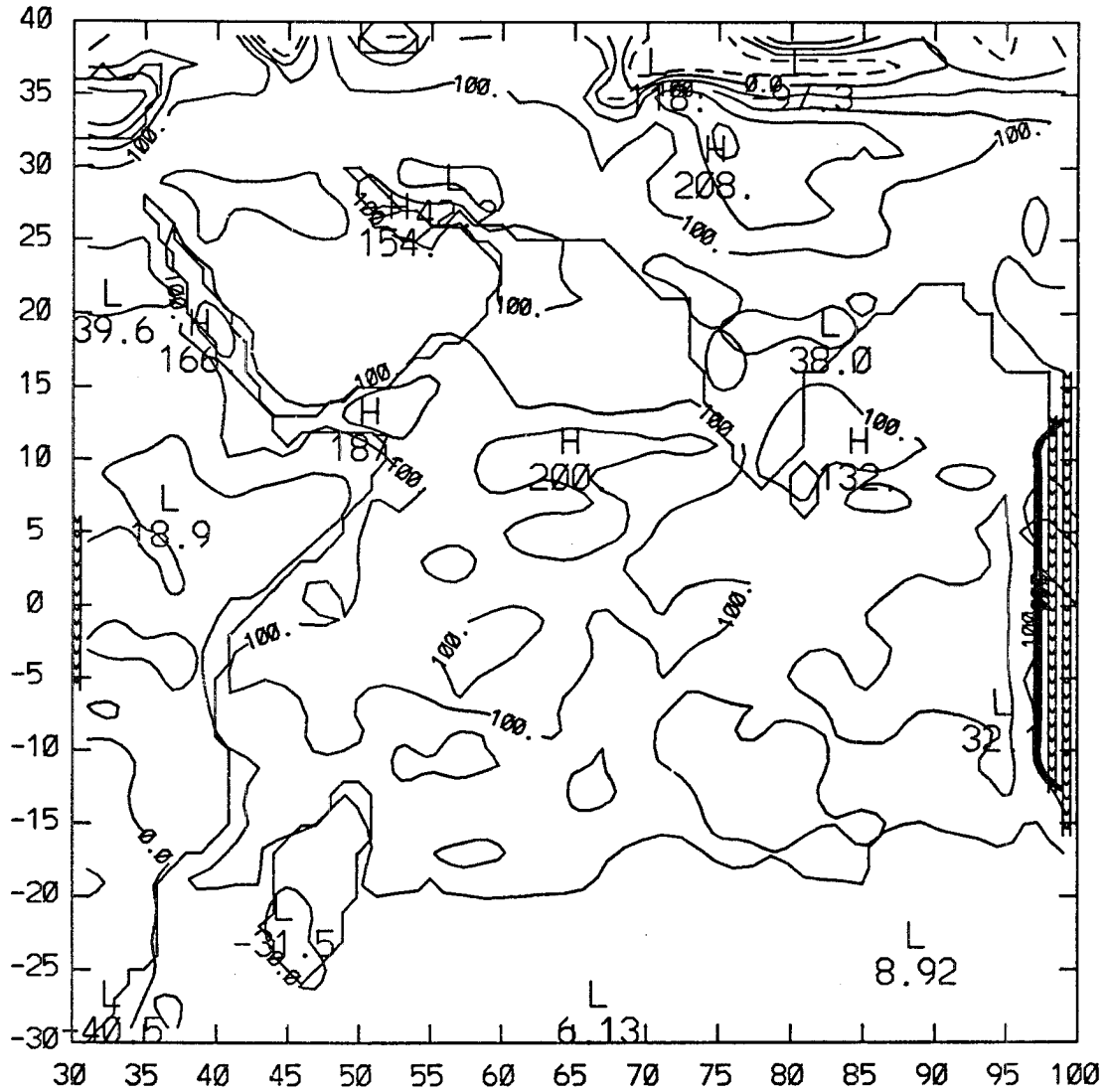


Figure 27. Continued

previous period. The Saudi Arabian peninsula still exhibits a relative minimum during this period due to the high surface albedo and high surface temperature. The northward advancement of the monsoon during the post-onset phase results in a suppression of the surface radiative gain of the northern Arabian Sea. During this period maximum surface radiative energy gains are found in the southern regions of the Arabian Sea and Bay of Bengal. There is also a relative maximum over northern India.

The surface radiation budget undergoes dramatic changes during these six periods; as shown in table 4 which lists the 5° by 5° mean radiative surface energy budget for four geographic regions: the Empty Quarter region of the Arabian peninsula; the northern Arabian Sea; central India; and the northern Bay of Bengal. The total cloud cover, in percent, is given in parenthesis. Between the pre-onset and post-onset periods the surface budget of these regions changes by a factor of two. A large amount of this variation is due to changing cloud cover, and in the case of the Empty Quarter region, changes in dust concentration.

TABLE 4. Net surface radiative energy budget for four geographic regions; Empty Quarter (20°N to 25°N and 45°E to 50°E); northern Arabian Sea (20°N to 25°N and 60°E to 65°E); central India (20°N to 25°N and 75°E to 70°E); and northern Bay of Bengal (15°N to 20°N and 85°E to 90°E). Units are  $W m^{-2}$ . Values in parenthesis are the total cloud cover in percent.

Region	January	February	Early May	Pre-Onset	Onset	Post-Onset
Empty Quarter	-2 (67)	-1 (37)	18 (25)	31 (9)	27 (3)	62 (1)
Northern Arabian Sea	51 (45)	79 (24)	191 (4)	260 (1)	225 (18)	124 (57)
Central India	52 (28)	56 (30)	125 (4)	160 (9)	151 (32)	70 (85)
Northern Bay of Bengal	91 (14)	95 (20)	141 (40)	214 (26)	103 (80)	79 (99)

#### 4. SUMMARY

A major objective of the summer monsoon experiment (SMONEX) was the determination of the heat sources and sinks associated with the southwest summer monsoon. This paper presents the radiative component. It is not possible to determine the relationship between radiative forcing and the monsoon with this single data set. However, the radiative energy budgets presented in this study can be used in conjunction with other data sets and/or models to better describe the role of radiative processes on the evolution of the southwest summer monsoon. Results that are of particular interest to the objectives of SMONEX are:

1) The vertically integrated tropospheric radiative energy budget is negative and varies significantly as a function of monsoon activity. The gradient in the latitudinal mean tropospheric cooling reverses between the winter periods and the late spring/early summer periods. However latitudinal means do not represent the total picture as longitudinal variations in

radiative cooling are as large as the latitudinal variations. In general, cloud free oceanic regions display the largest tropospheric cooling, while desert regions are areas of minimum cooling.

2) The radiative component of the vertical profile of the diabatic heating is derived. These radiative heating profiles are a strong function of the stage of the monsoon as well as the geographic region. Of particular interest are the vertical heating profiles over the deserts where the presence of dust can lead to large perturbations in the heating, resulting in a net warming near the top of the dust layer. The atmospheric response to this diabatic heat source may be more than local, as suggested by Das and Bedi (1981).

3) In general the surface is a net gain of radiative energy during the late spring and early summer periods. During the winter periods areas northward of 25°N display net surface losses, while the remaining areas exhibit net gains. Large temporal and spacial variations are observed in the surface radiative energy budget.

5. REFERENCES

- Ackerman, S. A. and S. K. Cox, 1981: Comparison of satellite and all-sky camera estimates of cloud cover during GATE. J. Appl. Meteor., 20, 581-587.
- Ackerman, S. A. and S. K. Cox, 1982: The Saudi Arabian heat low: aerosol distributions and thermodynamic structure. J. Geophys. Res., 87, 8991-9002
- Ackerman, S. A. and G. L. Stephens, 1986: On the absorption of solar radiation by cloud droplets: an application of anomalous diffraction theory. Submitted to J. Atmos. Sci.
- Aida, M., 1977: Scattering of solar radiation as a function of cloud dimensions and orientation. J. Quant. Spectrosc. Radiat. Transfer, 17, 303-310.
- Budyko, M. I., 1955: Heat balance atlas (Atlas teplovogo balansa). Leningrad.
- Chylek, P. and V. Ramaswamy, 1982: Simple approximation for infrared emissivity of water clouds. J. Atmos. Sci., 39, 171-177.
- Cox, S. K. and K. T. Griffith, 1979: Estimates of radiative divergence during Phase III of the GARP Atlantic Tropical Experiment: Part I. Methodology. J. Atmos. Sci., 36, 576-585.
- Cox, S. K., S. A. Ackerman, and T. H. Vonder Haar, 1986: Neighbor-to-Neighbor objective satellite analysis for the determination of surface and cloud mean radiative properties. Volume of extended abstracts, Second Conference on Satellite Meteorology/Remote Sensing, May 13-16, Williamsburg, VA.
- Carlson, T.N. and S.G. Benjamin, 1980: Radiative characteristics of Saharan dust. J. Atmos. Sci., 37, 193-213
- Das, P. K. and H. S. Bedi, 1981: The role of topography and heat sources on the summer monsoon. Preprint volume of the International Conference on Early Results of FGGE and Large-scale Aspects of its Monsoon Experiments., Tallahassee, FL.
- Davis, J. M., S. K. Cox, and T. B. McKee, 1979: Total shortwave radiative characteristics of absorbing finite clouds. J. Atmos. Sci., 36, 508-518.
- Davis, J. M., S. K. Cox and T. B. McKee, 1979b: Vertical and horizontal distributions of solar absorption in finite clouds. J. Atmos. Sci., 36, 1976-1984.

- DeLuisi, J. J., P. M. Furukawa, D. A. Gillette, B. G. Schuster, R. J. Charlson, W. M. Porch, R. W. Fegley, B. M. Herman, R. A. Rabinoff, J. T. Twitty and J. A. Weinman, 1976: Results of a comprehensive atmospheric aerosol-radiation experiment in the southwestern United States. Part II: Radiation flux measurements and theoretical interpretation. J. Appl. Met., 15, 455-463.
- Dopplick, T. G., 1972: Radiative heating of the global atmosphere. J. Atmos. Sci., 29, 1278-1294.
- Dopplick, T. G., 1979: Radiative heating of the global atmosphere: Corrigendum. J. Atmos. Sci., 36, 1812-1817.
- Edlin, H. L. and A. Huxley, 1973: Atlas of plant life. John Day Co., New York, 128 pp.
- Ellingson, R. G. and G. N. Serafino, 1984: Observations and calculations of aerosol heating over the Arabian Sea during MONEX. J. Atmos. Sci., 41, 575-588.
- Fein, J. S. and J. P. Kuettnner, 1980: Report of the summer MONEX field phase. Bull. mer. Meteor. Soc., 61, 461-474.
- Fouquart, Y., B. Bonnel, G. Brogniez, A. Cerf, M. Chaoui, L. Smith, and J.C. Vanhoutte, 1984: Size distribution and optical properties of Saharan aerosols during ECLATS. Aerosols and Their Climatic Effects, H. Gerber and A. Deepak (Eds.). A. Deepak Pub., 1984
- Fung, I., D.E. Harrison and A.A. Lacis, 1984: On the Variability of the net longwave radiation at the ocean surface. Rev. Geophys. Space Phys., 22, 177-193.
- Gautier, C., G. Diak and S. Masse, 1980: Simple physical model to estimate incident solar radiation at the surface from GOES satellite data. J. Appl. Meteor., 19, 1005-1012.
- Gautier, C., 1984: Surface radiation budget. Large-scale Oceanographic Experiments and Satellites. C. Gautier and M. Fieux (eds.), 185-203. D. Reidel Publishing Company.
- Gautier, C., 1986: Evolution of the net surface shortwave radiation over the Indian Ocean during summer MONEX (1979): A satellite description. Mon. Wea. Rev., 114, 525-533.
- Griffith, K. T., S. K. Cox and R. G. Knollenberg, 1980: Infrared radiative properties of tropical cirrus clouds inferred from aircraft measurements. J. Atmos. Sci., 37, 1077-1087.
- Herzogh P. H., 1981: Airborne observations of ice particles in convective and stratiform clouds associated with winter monsoon precipitation systems. Preprint volume of the International Conference on Early Results of FGGE and Large-scale Aspects of its Monsoon Experiments., Tallahassee, FL.

- Heymsfield, A. J., 1977: Precipitation development in stratiform ice clouds: a microphysical and dynamical study. J. Atmos. Sci., 34, 367-381.
- Holton, J. R., 1979: An Introduction to Dynamic Meteorology, 2nd ed. International Geophysics Series, Vol. 23, Academic Press.
- Hussey, W.J., 1979: The TIROS-N/NOAA operational satellite system. Technical report, National Environmental Satellite Service, NOAA, Dept. of Commerce, Washington, D.C., 35 pp.
- Kaneshige, T.M., 1980: The structure of FGGE data sets and the status of their availability for FGGE research. Bull. mer. Meteor. Soc., 61, 475-477.
- Katayama, A., 1967a; On the radiation budget of the troposphere over the Northern Hemisphere (II). Hemispheric distribution. Jour. Met. Soc. Japan, 45, 1-25.
- Katayama, A., 1967b; On the radiation budget of the troposphere over the Northern Hemisphere (III). Zonal cross-section and energy consideration. Jour. Met. Soc. Japan, 45, 26-39.
- Krishnamurti, T. N. and Y. Ramanathan, 1982: Sensitivity of monsoon onset to differential heating. J. Atmos. Sci., 39, 1290-1306.
- Lauritson, L., G. J. Nelson, and F. W. Portr, 1979: Data extraction and calibration of TIROS-N/NOAA radiometers. NOAA Tech. Memo. NESS 107, NOAA-NESS, Washington, DC, 58 pp.
- Liou, K. and G. D. Wittman, 1979: Parameterization of the radiative properties of clouds. J. Atmos. Sci., 36, 1261-1273.
- Manabe, S., and R. Wetherald, 1967: Thermal equilibrium of the atmosphere with a given distribution of relative humidity. J. Atmos. Sci., 24, 241-259.
- Matthews, E., 1983: Global vegetation and land use data bases for climate studies. Bull. Amer. Meteor. Soc., 64, 793.
- McKee, T. B. and S. K. Cox, 1974: Scattering of visible radiation by finite clouds. J. Atmos. Sci., 31, 1885-1892.
- McKee, T. B. and S. K. Cox, 1976: Simulated radiance patterns for finite cubic clouds. J. Atmos. Sci., 33, 2014-2020.
- Minnis, P. and E. F. Harrison, 1984: Diurnal variability of regional cloud and clear-sky radiative parameters derived from GOES data. Part I: analysis method. J. Appl. Meteor., 23, 993-1011.
- Murakami, M., 1983: Analysis of the deep convective activity over the western pacific and southeast Asia. Part I: diurnal variation. J. Meteor. Soc. Japan, 61, 60-75.

- Newiger, M. and K. Bahnke, 1981: Influence of cloud composition and cloud geometry on the absorption of solar radiation. Beitr. Phys. Atmosph., 54, 370-382.
- Patterson, E. and D. A. Gillette, 1977: Measurements of visibility vs. mass-concentration for airborne soil particles. Atmos. Envir., 11, 193-196.
- Patterson, E., G.W. Grams, and C.O. Pollard, 1983: Aircraft measurements of aerosol optical properties during the MONEX program. Technical report, School of Geophysical Sciences, Georgia Institute of Technology, Atlanta GA, 30332, 28 pp.
- Paltridge, G. W., 1974: Infrared emissivity, shortwave albedo, and the microphysics of stratiform water clouds. J. Geophys. Res., 79, 4053-4058.
- Paltridge, G. W. and C. M. Platt, 1981: Aircraft measurements of solar and infrared radiation and the microphysics of cirrus clouds. Quart. J. Roy. Meteor. Soc., 107, 367-380.
- Platt, C.M.R., 1976: Infrared absorption and liquid water content in stratocumulus clouds. Quart. J. R. Met. Soc., 102, 515-522.
- Ramage, C.S., F.R. Miller and C. Jefferies, 1972; Meteorological Atlas of the International Indian Ocean Expedition. Volume 1; The Surface Climate of 1963 and 1964. U.S. government Printing Office, Washington, D.C. 20402.
- Rockwood, A., and S. K. Cox, 1978: Satellite inferred surface albedo over northwestern Africa. J. Appl. Meteor., 35, 513-522.
- Rosinski, J., C. T. Nagamoto, G. Langer, and F. Parungo, 1970: Cirrus Clouds as Collectors of Aerosol Particles. J. Geophys. Res., 75, 2961-2973.
- Rossow, W. B., F. Mosher, E. Kinsella, A. Arking, M. Desbois, E. Harrison, P. Minnis, E. Ruprecht, G. Seze, C. Simmer, and E. Smith, 1985: ISCCP cloud algorithm intercomparison. J. Appl. Meteor., 24, 877-903.
- Saha K., 1974: Some aspects of the Arabian sea summer monsoon. Tellus, 26, 464-476.
- Schwalb, A., 1978: The TIROS-N/NOAA A-G satellite series. NOAA tech. memo, NES 95, NOAA-NESS, Washington, DC, 75 pp
- Sikka D.R. and S. Gadgil, 1980: On the maximum cloud zone and the ITCZ over Indian longitudes during the southwest monsoon. Mon. Wea. Rev., 108, 1840-1853.
- Smith, E. A., 1984: Radiative forcing of the southwest summer monsoon; A satellite perspective. Ph. D. dissertation, Dept. Atmos. Sci., Colorado State University, Fort Collins, CO, 80523.

- Smith, E. A. and J. Graffy, 1982: A TIROS-N AVHRR digital data set for analysis of the 1979 southwest summer monsoon. Special Report, Dept. Atmos. Sci., Colorado State University, Fort Collins, CO.
- Smith, E. A., S. A. Ackerman, S. K. Cox, and T. H. Vonder Haar, 1980: Summer MONEX high altitude aircraft radiation measurements. Atlas of MONEX aircraft measurements, Dept. Atmos. Sci., Colo. State Univ., Fort Collins, CO, 84 pp.
- Smith, E. A., T. H. Vonder Haar, R. M. Welch, W. J. Wiscombe, 1980: The development of a multispectral radiative signature technique for estimation of rainfall from satellites - Radiation models. Tech. Report, Cooperative Institute for Research in the Atmosphere, Colorado State University, Fort Collins, CO.
- Stephens, G. L., 1978a: Radiation profiles in extended water clouds. Part I. Theory. J. Atmos. Sci., 35, 211-2122.
- Stephens, G. L., 1978b: Radiation profiles in extended water clouds. Part II. Parameterization schemes. J. Atmos. Sci., 35, 211-2122.
- Stephens, G. L., S. A. Ackerman and E. A. Smith, 1984: A shortwave parameterization revised to improve cloud absorption. J. Atmos. Sci., 41, 687-690.
- Tampieri, F. and C. Tomasi, 1976: Size distribution models of fog and cloud droplets in terms of the modified gamma function. Tellus, 28, 333-347.
- Tarpley, J.D., 1979: Estimating incident solar radiation at the surface from geostationary satellite data. J. Appl. Meteor., 18, 1172-1181.
- Webster, P.J., 1983: Mechanisms of monsoon low-frequency variability: Surface hydrological effects. J. Atmos. Sci., 40, 2110-2124.
- Welch, R. M., S. K. Cox and J. M. Davis, 1980: Solar radiation and clouds. Meteor. Monog., Vol. 39, Amer. Meteor. Soc., 93 pp.
- Welch, R. M., S. K. Cox and W. G. Zdunkowski, 1980: Calculations of the variability of ice cloud radiative properties at selected solar wavelengths. Appl. Opt., 19, 3057-3067.
- Welch, R. M. and W. G. Zdunkowski, 1981a: The radiative characteristics of noninteracting cumulus cloud fields. Part I: Parameterization for finite clouds. Beitr. Phys. Atmosph., 54, 258-272.
- Welch, R. M. and W. G. Zdunkowski, 1981a: The radiative characteristics of noninteracting cumulus cloud fields. Part II: Calculations for clouds fields. Beitr. Phys. Atmosph., 54, 273-285.
- Welch, R. M. and W. G. Zdunkowski, 1981c: The effect of cloud shape on radiative characteristics. Beitr. Phys. Atmosph., 54, 482-491.

## APPENDIX

This appendix presents analysis of the cloud top distributions derived from the TIROS-N multichannel Advanced Very High Resolution Radiometer (AVHRR) and GOES-1 Visible-Infrared Spin Scan Radiometer (VISSR). The TIROS-N is a sun synchronous, polar orbiting satellite with equatorial crossing times of 0300 (desending) and 1500 (ascending) mean solar time. Channel 1 (.552-.904  $\mu\text{m}$ ) and channel 4 (10.52-11.45  $\mu\text{m}$ ) Global Area Coverage (GAC) data were used in the cloud retrieval technique. The resolution of the GAC data is approximately 8 km at nadir. Data was analyzed for the day and night passes for the period May 1, 1979 to August 30, 1979 for the region  $0^{\circ}$  to  $35^{\circ}$  N latitude and  $30^{\circ}$  E to  $100^{\circ}$  E longitude (figure 1). Several days have no GAC data, including a 13 day gap from 6-13 August. The GAC data were mapped by Smith and Graffy (1982) onto a uniform grid with a resolution of 15 points per degree latitude or longitude. The scheme of Lauritson et al. (1979) was used to convert raw digital data to window temperatures. Additional information on the TIROS-N and the AVHRR imager can be found in Hussey (1977, 1979) and Schwalb (1978).

The Visible-Infrared Spin Scan Radiometer (VISSR) from the geostationary satellite GOES-1, which was positioned at approximately  $57^{\circ}$  E longitude during FGGE, provided the second satellite data set. The visible (.5-.85  $\mu\text{m}$ ) and IR (10.0-12.5  $\mu\text{m}$ ) channels were used to determine the cloud top distributions. The data were mapped to the same resolution as the TIROS-N, yet covered a larger north-south region ( $30^{\circ}$ S- $40^{\circ}$ N latitude). Eight time periods per day were used to estimate diurnal fluctuations (2, 5, 8, 11, 14, 17, 20 and 23 GMT). There were problems with the GOES-1 VISSR IR sensor during 1979 so that a consistent day to day evolution of the southwest summer monsoon was unavailable. The transformation of the VISSR IR raw counts to equivalent

blackbody temperatures was accomplished using the Standard National Environmental Satellite Service (NESS) lookup table. Since no checks were made to update the GOES-1 calibration table, a re-calibration of the GOES-1 IR sensor was made by comparing  $1^\circ \times 1^\circ$  mean temperature from the GOES-1 with AVHRR derived temperatures at coincident time periods. The results are shown in figure 9 along with a least squares fit to the data. The major discrepancy was at the colder temperature where the GOES-1 was several degrees warmer. There is excellent agreement at the higher temperatures.

Two corrections were applied to the satellite derived apparent cloud top temperature (Cox and Griffith, 1979). The first correction accounts for water vapor emission in the window channel of the satellite detector. This correction term was represented as a function of the precipitable water above cloud top determined from FGGE IIIb moisture profiles. Figure 10 depicts this temperature correction where the circles depict calculations using various FGGE IIIb temperature and moisture profiles and the solid line is the function used in this study. The second correction accounts for the penetration distance into the cloud before radiative blackness is achieved, and is a function of cloud water content and the mass absorption coefficient. Cloud water content was assigned according to figure 3 along with a mass absorption coefficient of  $0.045 \text{ m g}^{-1}$ . The penetration distance was then converted to a temperature correction using the lapse rate of the given region. Once the cloud top temperature is determined, cloud top pressure is located using the temperature profile of the appropriate region. Satellite measurements in the visible were used to tune the clear sky IR threshold over the ocean in a manner similar to that used by Cox and Griffith (1979). Comparisons of the GOES-1 VISSR derived cloud amount with that of the TIROS-N AVHRR retrieval are discussed in Section 3.

Due to the more continuous coverage of the SMONEX region by the TIROS-N satellite this data is analyzed to present an estimate of the day to day changes in cloud cover. As a result of the better diurnal coverage of the GOES-1, this data is analysed to describe the diurnal fluctuations in cloud cover as well as to compare changes in cloud cover during several 10 day periods of 1979 (see Table 1).

#### A.1 Cloud cover analysis of TIROS-N AVHRR data

The onset of the southwest summer monsoon is often described in terms of the northward advancement of various cloud systems. In the present study the onset is best seen in a cross sectional analysis of  $1^{\circ}$  latitude by  $10^{\circ}$  longitude mean percent high cloud, defined as cloud tops with pressures less than 400 mb. Regions with large amounts of high clouds are considered to be regions that are, or recently were, convectively active. Figure A1 is the cross-sectional analysis for four longitude belts:  $55^{\circ}$  E to  $65^{\circ}$  E (western Arabian Sea),  $65^{\circ}$  E to  $75^{\circ}$  E (eastern Arabian Sea),  $75^{\circ}$  E to  $85^{\circ}$  E (India) and  $85^{\circ}$  E to  $95^{\circ}$  E (Bay of Bengal), derived from the TIROS-N data set. Shaded regions depict percentage of high cloud cover greater than 50 percent. The convective activity in the beginning of the month of May over the Bay of Bengal and India is associated with a tropical disturbance. After the dissipation of this storm there is little convective activity for the rest of the month. Most convective activity occurs south of  $10^{\circ}$ N. Prior to the monsoon onset the major convective activity is below  $3^{\circ}$  N. The increase in high clouds in the eastern Arabian sea on June 12 (JD 163) is associated with the onset vortex as it moves westward, the northward movement of the onset vortex is better seen in the cross-sectional analysis of the eastern Arabian Sea region ( $65^{\circ}$ E- $75^{\circ}$ E). After the onset vortex dissipates over the coast of

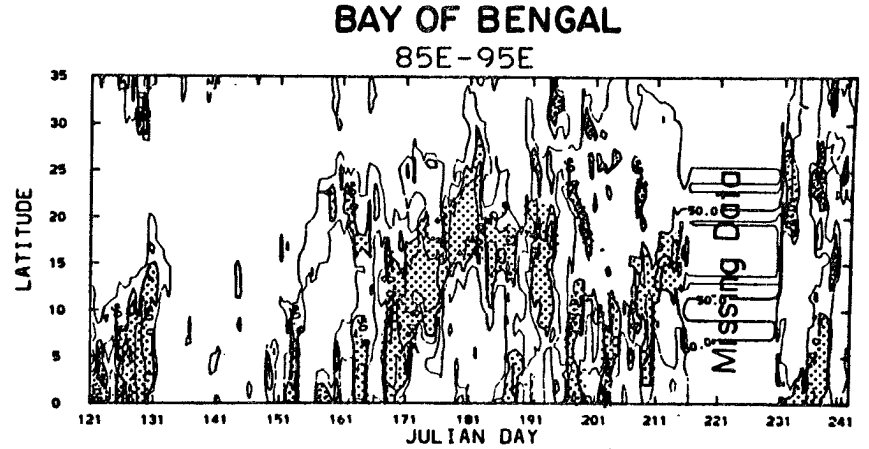
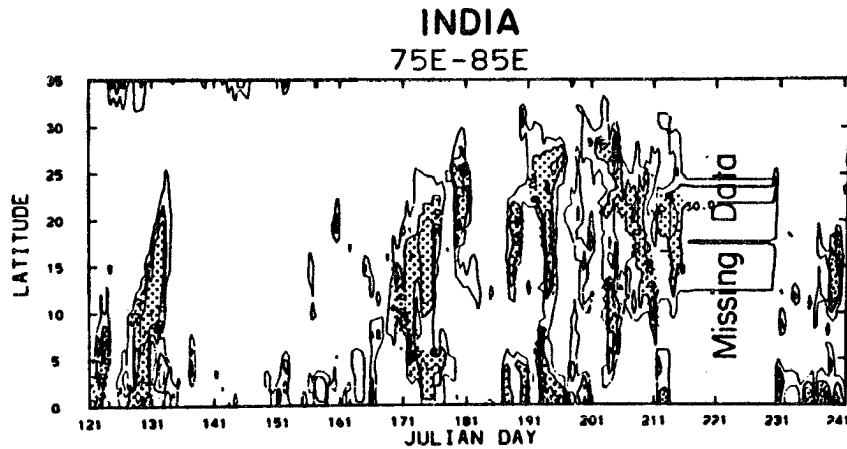
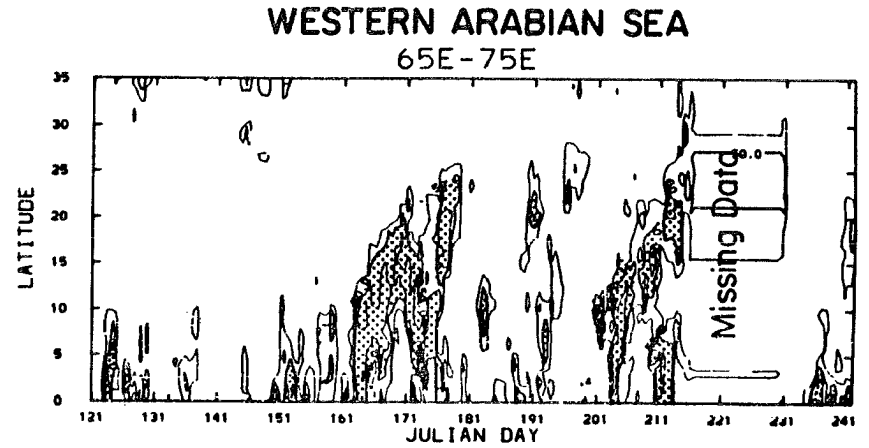
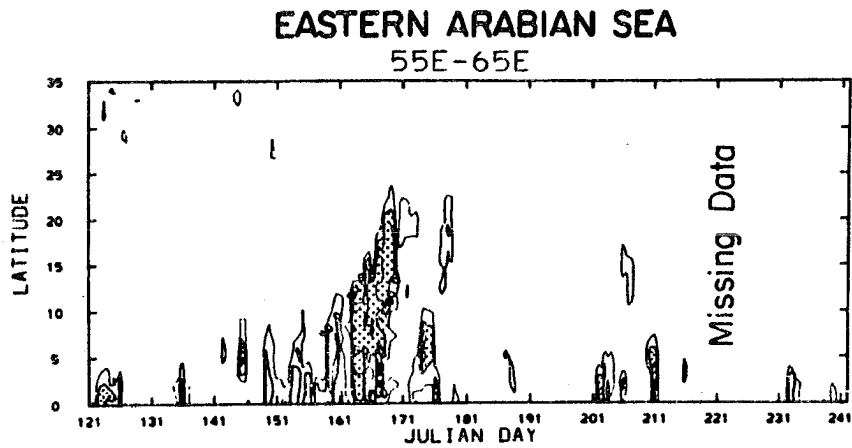


Figure A1. Cross-sectional analysis of the areal percentage of high cloud (cloud tops with pressures less than 400 mb) for four longitude belts : 55°E to 65°E (eastern Arabian Sea), 65°E to 75°E (western Arabian Sea), 75°E to 85°E (India) and 85°E to 95°E (Bay of Bengal). Shaded regions depict cases for which the percentage of high cloud is greater than 50%.

Oman there is little convective activity in the western Arabian Sea. Similarly, after the monsoon onset convective activity over the eastern Arabian Sea is considerably reduced until late July when there is a revival in the monsoon and a corresponding northward propagation of a major convective region. In contrast the Bay of Bengal is convectively active during the entire period except for mid and late May. The maximum areal extent of convective activity over the Bay occurs during the active periods of the monsoon. During this period a northward propagation of the convective region is evident. While convective activity increases over the Arabian Sea and the Bay of Bengal on 10 June (JD 161), an increase in convective activity is not seen over the Indian peninsula ( $75^{\circ}\text{E}-85^{\circ}\text{E}$ ) until approximately 19 June (JD 170), with a break in convective activity in the first week of July. An increase in high clouds over the Indian Peninsula from approximately 7-10 July (JD 188-191) is associated with the landfall and westward propagation of a Bay of Bengal depression. This depression rapidly dissipates as it moves westward and is followed by major convective activity over India for the period 12-15 July (JD 193-196). The monsoon break, beginning approximately 16 July (JD 197), also displays a lack of convective activity over India. The regions of persistent convective activity during the break period are the southern Bay of Bengal and the northern Bay and Bangladesh region. On 20 July (JD 201) a system develops in the eastern Arabian Sea at approximately  $10^{\circ}\text{N}$  and moves northward to  $22^{\circ}\text{N}$  by 31 July (JD 212). On 23 July (JD 204) this system is a band structure extending from  $65^{\circ}\text{E}$  to  $100^{\circ}\text{E}$  centered at approximately  $10^{\circ}\text{N}$  and then propagates northward. On the 25 July (JD 206) there appears to be two separate systems with a minimum in convective activity over the Indian Peninsula, while there is still convective activity over India between approximately  $20^{\circ}-30^{\circ}\text{N}$ . With a revitalization of the monsoon (28 July, JD

209 comes an increase in the convective activity over India. The Bay of Bengal still displays convective activity. Two regions of high cloud are also observed over the region  $75^{\circ}$  E -  $85^{\circ}$  E during late August, one between  $10^{\circ}$  and  $15^{\circ}$  N and one below  $5^{\circ}$ .

Large scale chronological changes in total cloud cover for May-July 1979 are seen better when a spatial average is made over four geographical regions: Bay of Bengal, Arabian Sea, India and Saudi Arabian Peninsula (figure A2). The Bay of Bengal has the largest cloud amount of the four regions. The large cloud cover amounts in the Bay of Bengal in the beginning of May is associated with a tropical depression which land falls on 12 May at approximately  $15^{\circ}$ N  $82^{\circ}$ E resulting in the large increase in cloudiness over India. Evidence of the tropical depression is also seen in the time series of percentage high cloud, figure A3. Prior to the onset of the monsoon, total cloudiness over the Bay of Bengal exhibits an approximate 11 day cycle in peak to peak maximum cloud cover. A similar periodicity is seen in the high cloud cover over the Bay of Bengal, and the total cloud cover over the Arabian Sea. After the monsoon is established, a distinct 5-7 day period is observed in the high cloud amount over the Bay of Bengal. During May the increases in cloud cover over the Saudi Arabian peninsula is a reflection of disturbances in the northern region of the peninsula, as opposed to the increase in cloudiness in mid-June which results from the onset vortex which approaches the peninsula from the Arabian Sea. As expected the Saudi Arabian Peninsula generally has the smallest amount of cloud cover. In May the convective activity of the Indian subcontinent is generally small except for the tropical disturbance discussed previously. The large increase in total cloudiness in June is associated with the onset of the monsoon, as is the increase in the high cloud amount. Both the total cloud cover and high cloud amount reach a relative

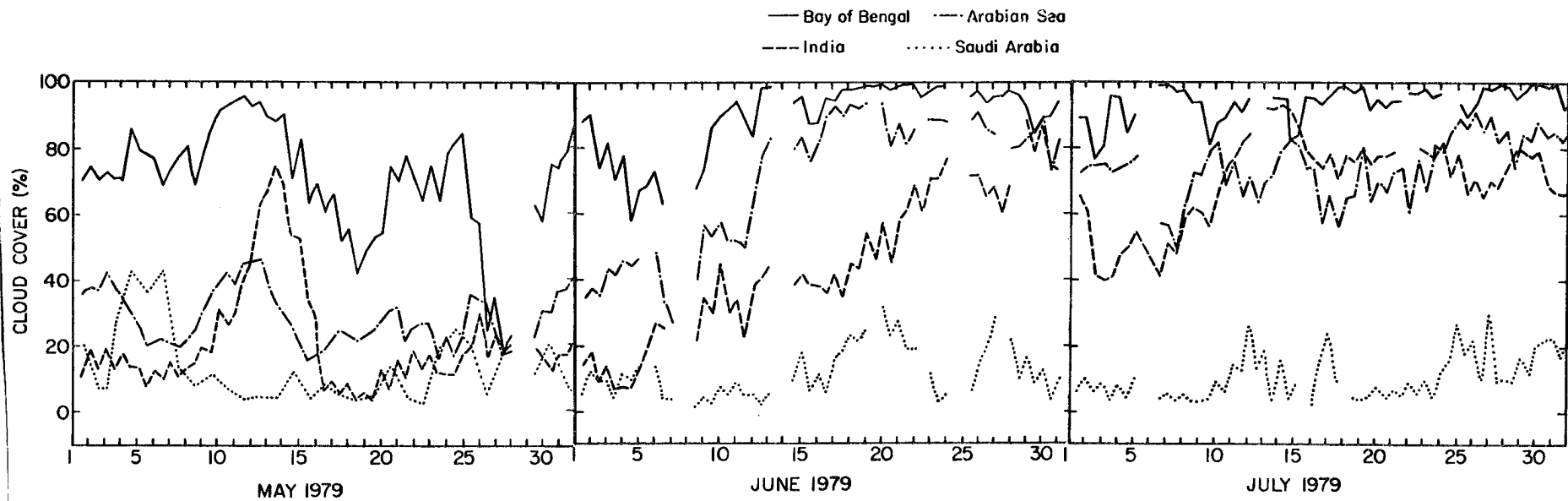


Figure A2. Areal coverage of total cloud amount for four geographical regions, as derived from analysis of the TIROS-N AVHRR data.

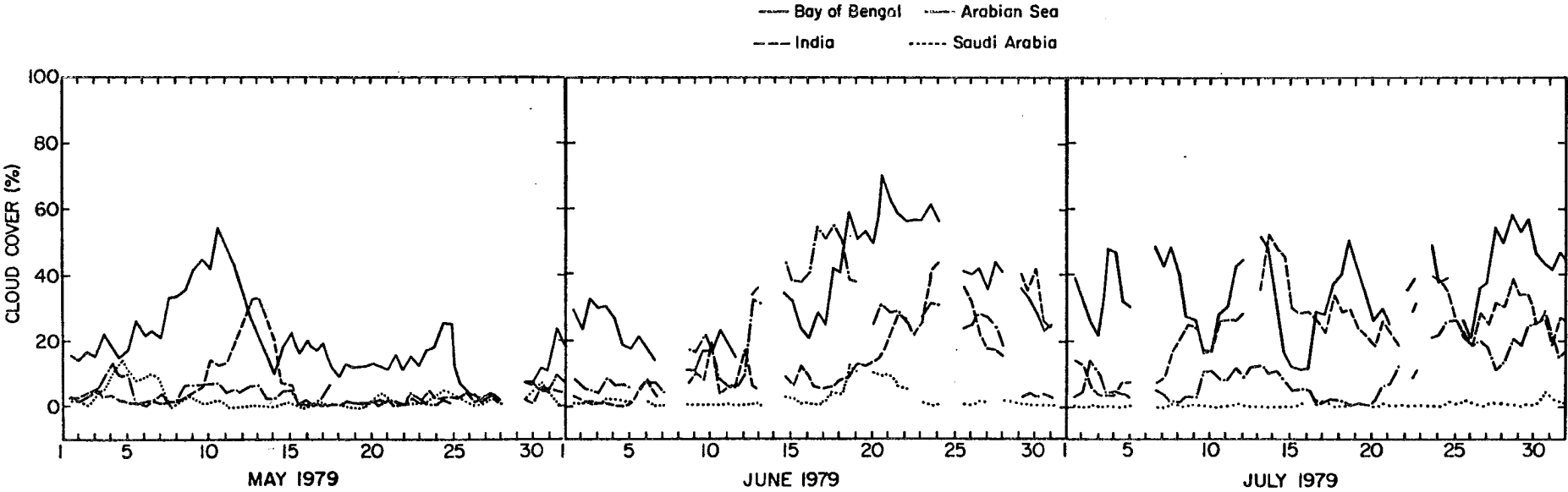


Figure A3. Areal coverage of high cloud for four geographical regions, as derived from analysis of the TIROS-N AVHRR data.

minimum on 3 July and then increase to a maximum on 14 July. The beginning of the monsoon break (approximately 16 July) is associated with a reduced amount of clouds over the Indian Peninsula and the Arabian Sea. The increase in cloudiness over the Arabian Sea on 20 July is associated with a disturbance which propagates northward and marks the revitalization of the monsoon.

#### A.2 Cloud cover analysis of GOES-1 VISSR data

The daytime and nighttime percent high cloud amount and percent clear determined from the GOES-1 analysis for the six phases of the 1979 southwest summer monsoon season are depicted in figures A4-A9. Also shown are day-night differences, where shaded regions depict nighttime maximums of total cloud or high cloud.

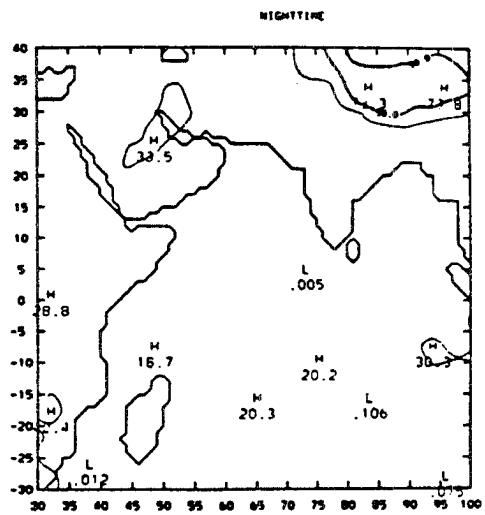
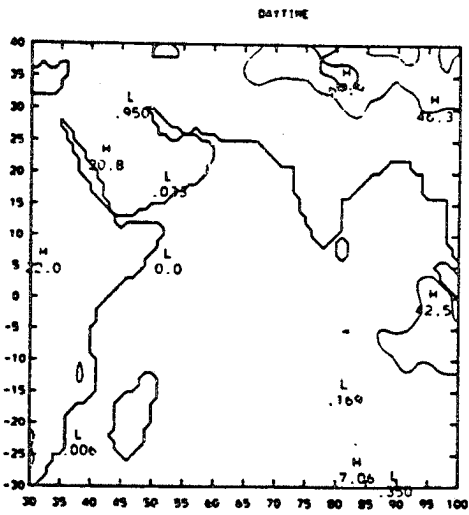
During the January phase large amounts of high cloud cover and total cloud cover are observed over the eastern section of Indian ocean. This region also has a strong diurnal (day-night) variation. The nighttime maximum in high cloud over the Saudi Arabian Peninsula is cirrus. The large cloud amounts over the Himalayas are likely a result of the inability of the satellite retrieval technique to separate cloud from the snow covered surface. The Indian Peninsula, the eastern Arabian Sea and Bay of Bengal are largely cloud free during this period.

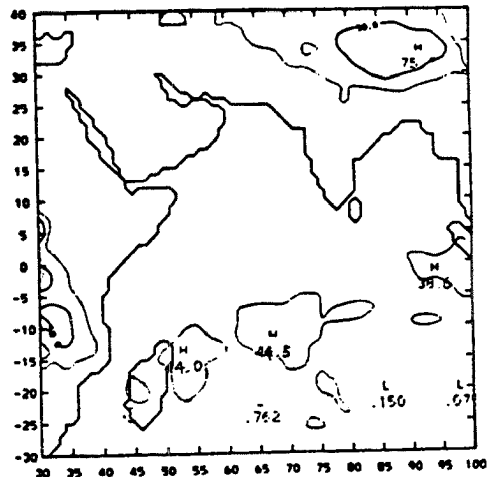
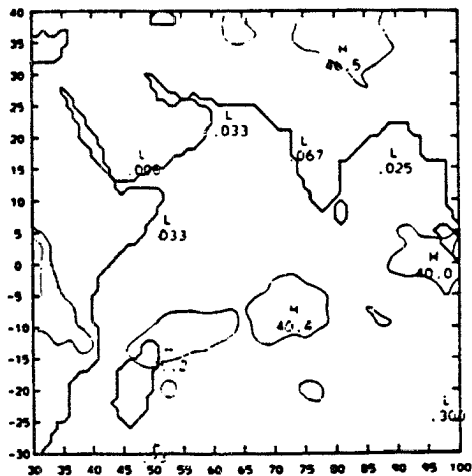
The oceanic convection seen in the January period is still evident in the daytime and nighttime distributions of high cloud for the February phase, which now appears as a line oriented WSW to ENE. This convective line is shifted slightly to the south in the nighttime hours, resulting in the daytime-nighttime patterns displayed in figure A5. There are also large amounts of high cloud near Tanzania, which exhibit a maximum during the night.

HIGH CLOUDS  
JANUARY PHASE

A-10

HIGH CLOUDS  
JANUARY PHASE

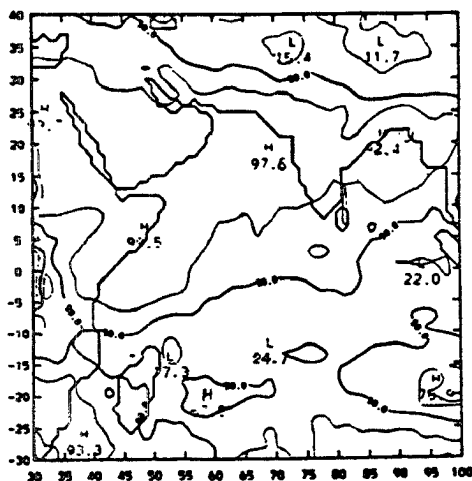




## PERCENT CLEAR

FEBRUARY PHASE

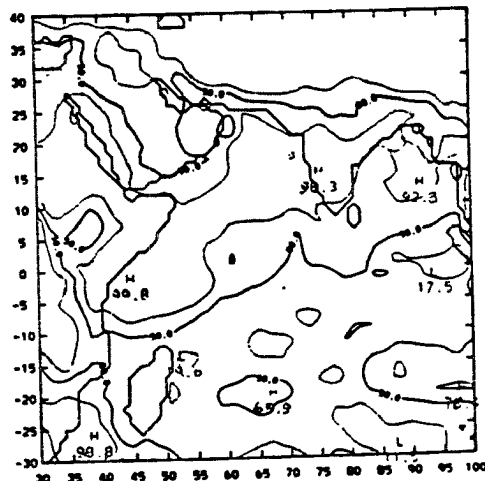
DAYTIME



## PERCENT CLEAR

FEBRUARY PHASE

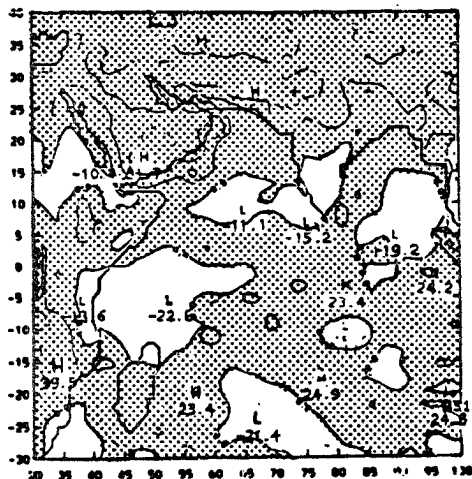
NIGHTTIME



## PERCENT CLEAR

FEBRUARY PHASE

DAY-NIGHT



## HIGH CLOUDS

FEBRUARY PHASE

DAY-NIGHT

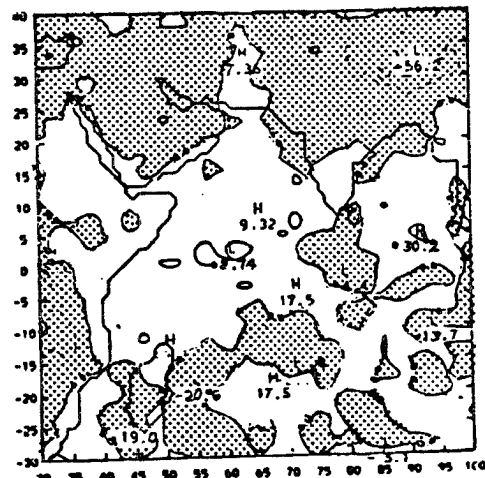
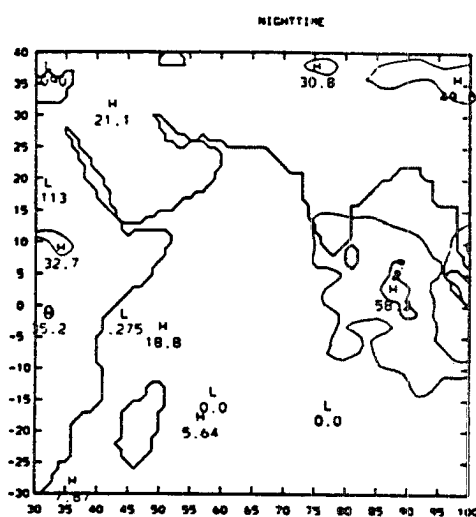
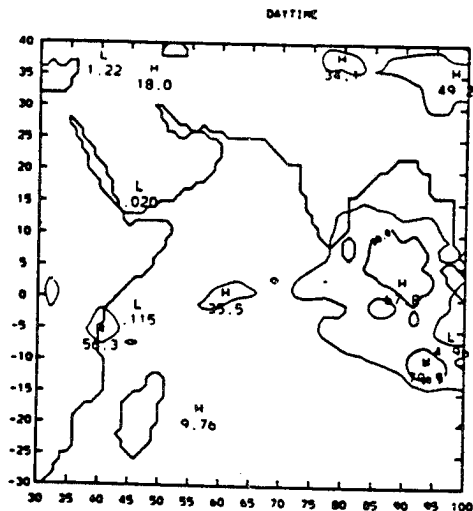


Figure A5. Spatial distribution of clouds derived from analysis of GOES-1 VISSR data, for the February phase of the 1979 summer monsoon. The panels are a) Daytime high cloud amount; b) Nighttime high cloud amount; c) Daytime total cloud amount; d) Nighttime total cloud amount; e) Day-night difference in clear regions (shaded regions depict regions of nighttime maximae in total cloud cover) f) Day-night difference in high cloud amount (shaded regions depict regions of nighttime maximae in high cloud amount).

HIGH CLOUDS  
EARLY MAY PHASE

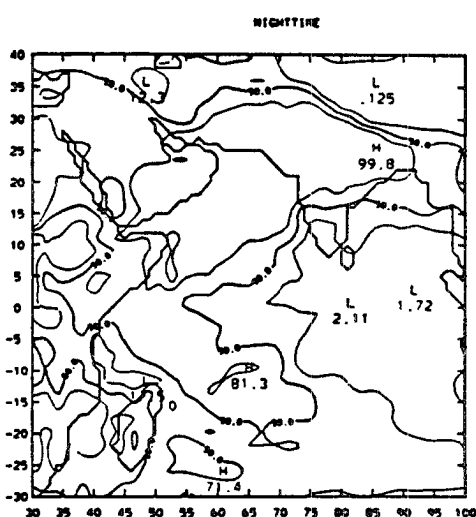
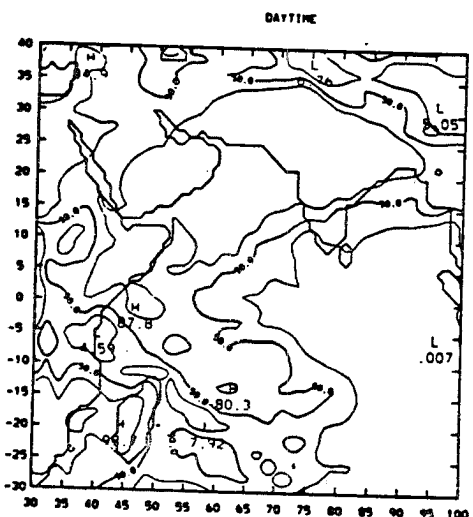
A-12

HIGH CLOUDS  
EARLY MAY PHASE



PERCENT CLEAR  
EARLY MAY PHASE

PERCENT CLEAR  
EARLY MAY PHASE



PERCENT CLEAR  
EARLY MAY PHASE

HIGH CLOUDS  
EARLY MAY PHASE

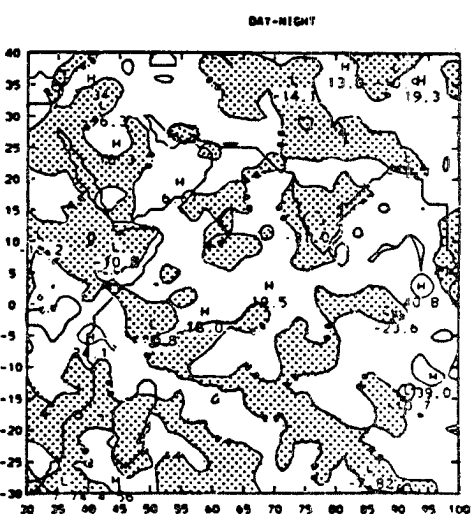
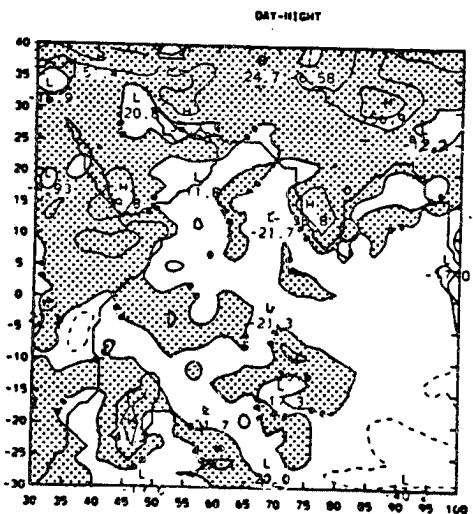


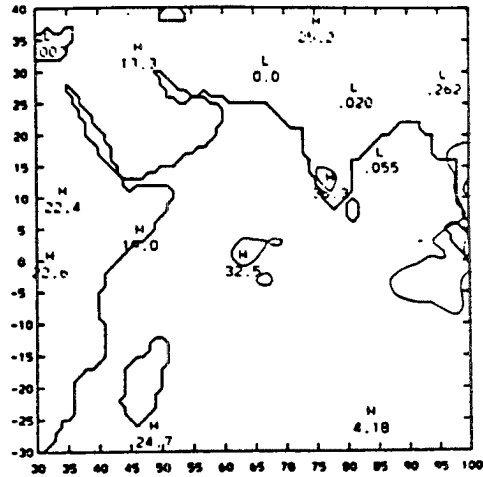
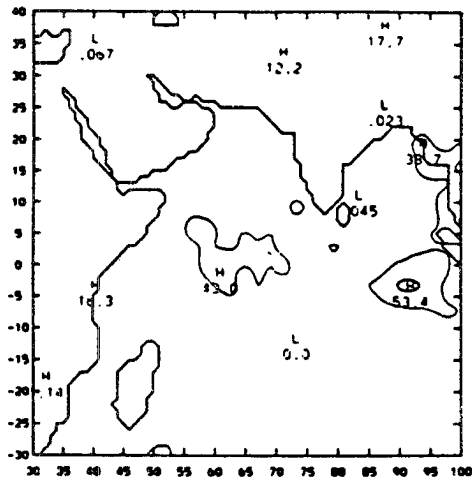
Figure A6. Spatial distribution of clouds derived from analysis of GOES-1 VISSR data, for the Early May phase of the 1979 summer monsoon. The panels are a) Daytime high cloud amount; b) Nighttime high cloud amount; c) Daytime total cloud amount; d) Nighttime total cloud amount; e) Day-night difference in clear regions (shaded regions depict regions of nighttime maxima in total cloud cover) f) Day-night difference in high cloud amount (shaded regions depict regions of nighttime maxima in high cloud amount).

PRE-ONSET PHASE

PRE-ONSET PHASE

DAYTIME

NIGHTTIME



PERCENT CLEAR

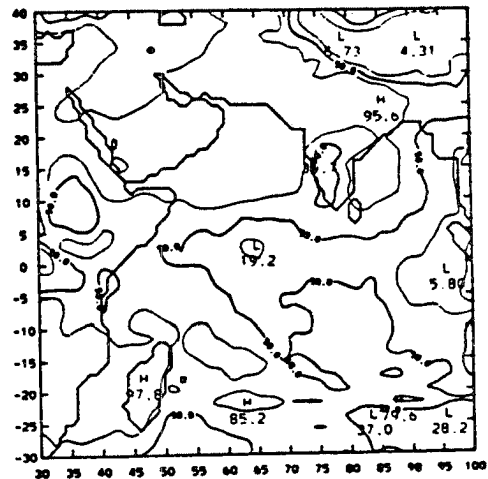
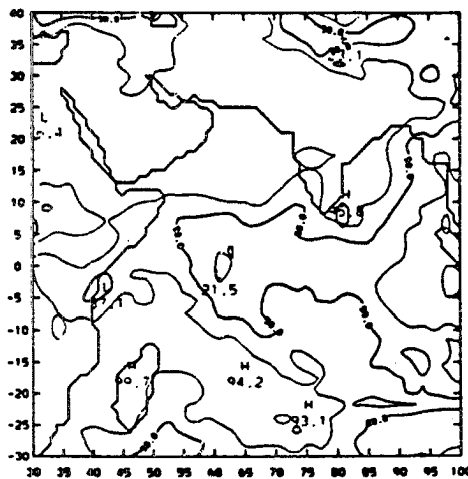
PERCENT CLEAR

PRE-ONSET PHASE

PRE-ONSET PHASE

DAYTIME

NIGHTTIME



PERCENT CLEAR

HIGH CLOUDS

PRE-ONSET PHASE

PRE-ONSET PHASE

DAY-NIGHT

DAY-NIGHT

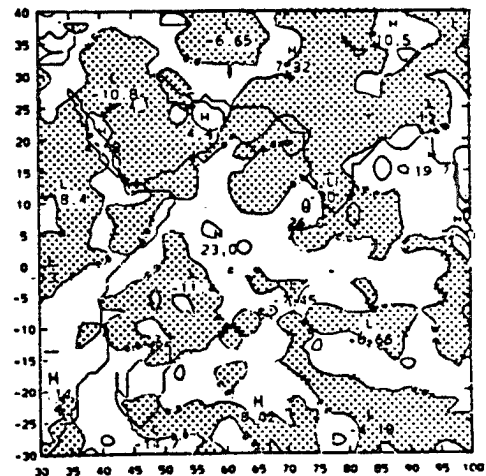
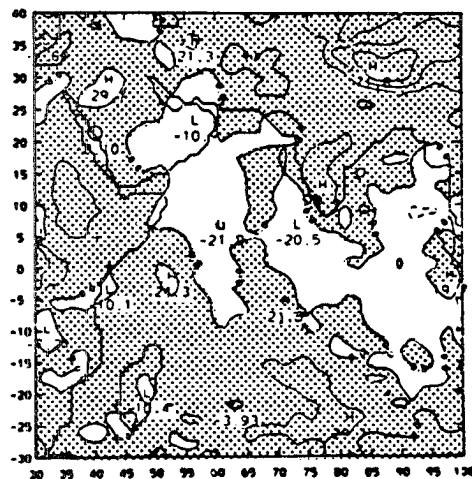


Figure A7. Spatial distribution of clouds derived from analysis of GOES-1 VISSR data, for the Pre-onset phase of the 1979 summer monsoon. The panels are a) Daytime high cloud amount; b) Nighttime high cloud amount; c) Daytime total cloud amount; d) Nighttime total cloud amount; e) Day-night difference in clear regions (shaded regions depict regions of nighttime maxima in total cloud cover) f) Day-night difference in high cloud amount (shaded regions depict regions of nighttime maxima in high cloud amount).

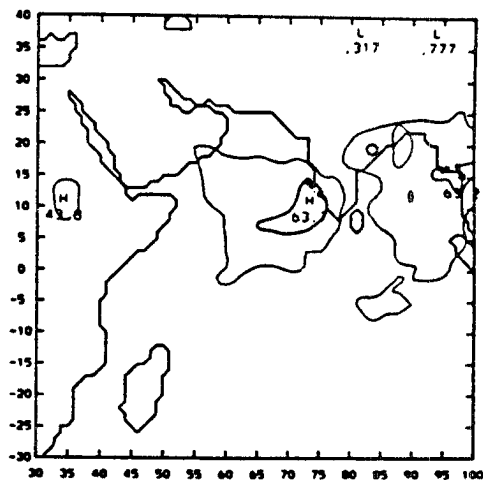
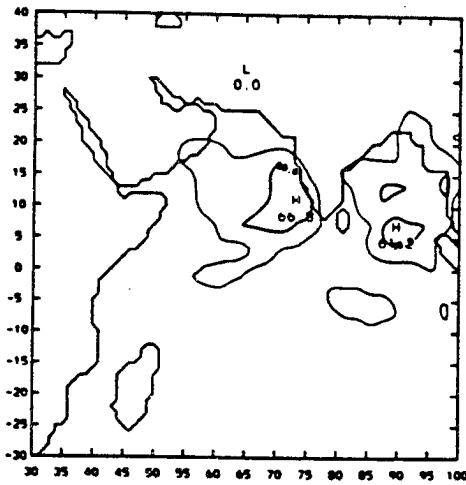
HIGH CLOUDS

ONSET PHASE

A-14

HIGH CLOUDS

ONSET PHASE



PERCENT CLEAR

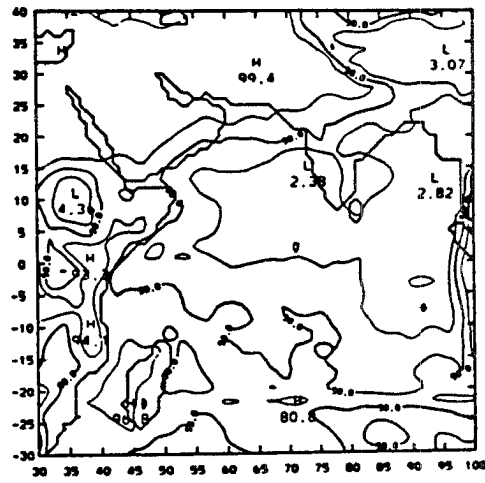
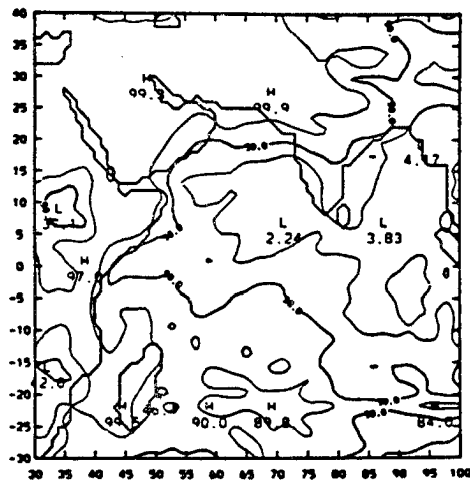
ONSET PHASE

DAYTIME

PERCENT CLEAR

ONSET PHASE

NIGHTTIME



PERCENT CLEAR

ONSET PHASE

DAY-NIGHT

HIGH CLOUDS

ONSET PHASE

DAY-NIGHT

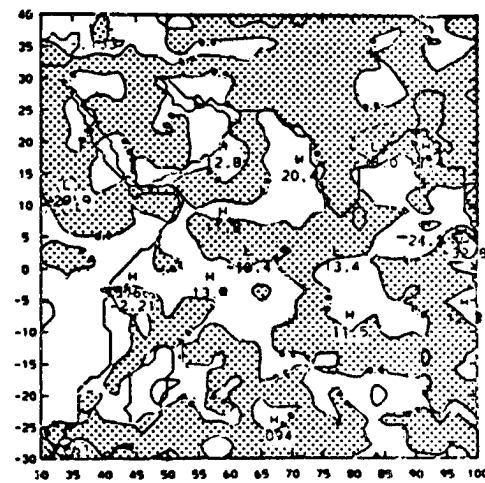
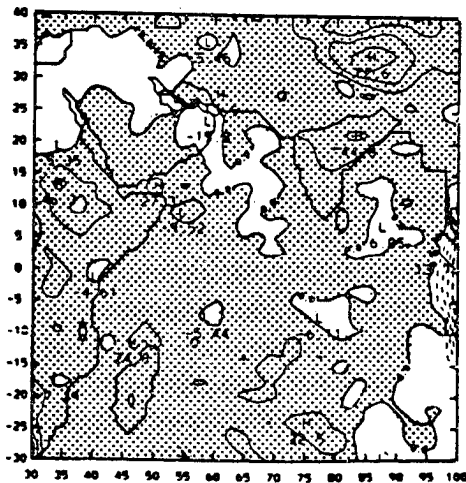
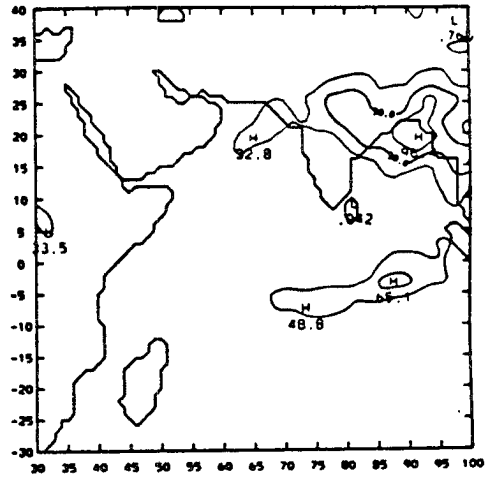
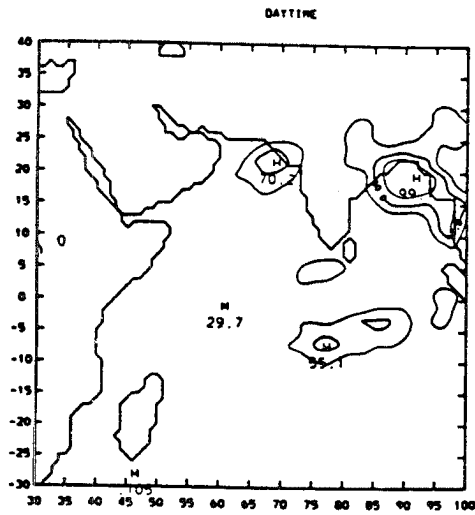
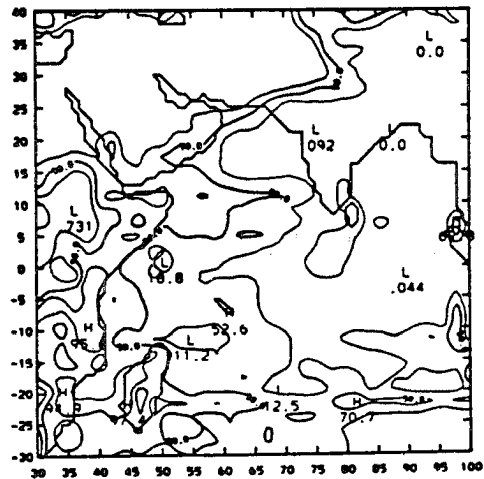
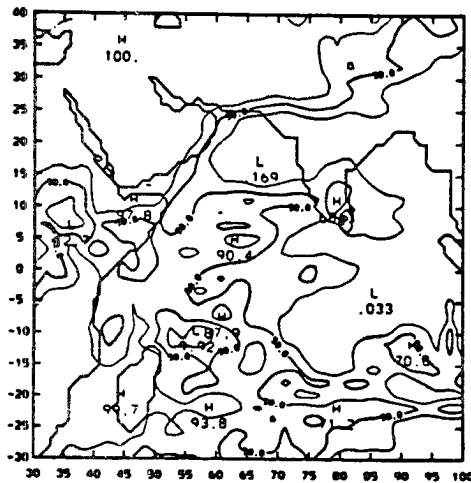


Figure A8. Spatial distribution of clouds derived from analysis of GOES-1 VISSR data, for the Onset phase of the 1979 summer monsoon. The panels are a) Daytime high cloud amount; b) Nighttime high cloud amount; c) Daytime total cloud amount; d) Nighttime total cloud amount; e) Day-night difference in clear regions (shaded regions depict regions of nighttime maximae in total cloud cover) f) Day-night difference in high cloud amount (shaded regions depict regions of nighttime maximae in high cloud amount).



PERCENT CLEAR  
POST-ONSET PHASE  
DAYTIME

PERCENT CLEAR  
POST-ONSET PHASE  
NIGHTTIME



PERCENT CLEAR  
POST-ONSET PHASE  
DAY-NIGHT

HIGH CLOUDS  
POST-ONSET PHASE  
DAY-NIGHT

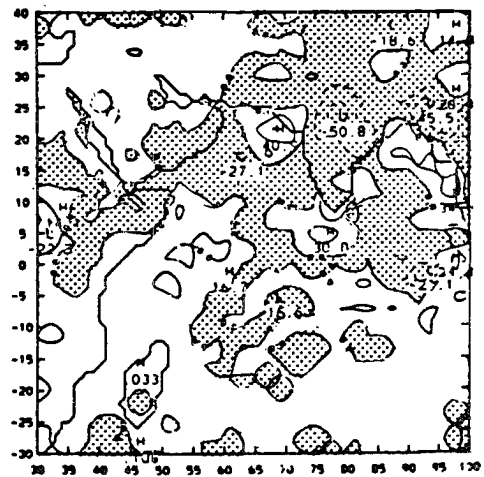
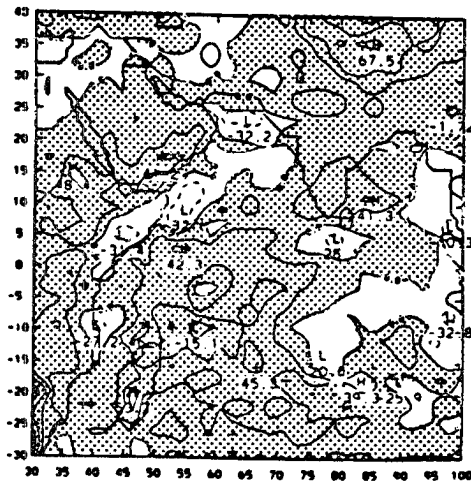


Figure A9. Spatial distribution of clouds derived from analysis of GOES-1 VISSR data, for the Post-onset phase of the 1979 summer monsoon. The panels are a) Daytime high cloud amount; b) Nighttime high cloud amount; c) Daytime total cloud amount; d) Nighttime total cloud amount; e) Day-night difference in clear regions (shaded regions depict regions of nighttime maxima in total cloud cover) f) Day-night difference in high cloud amount (shaded regions depict regions of nighttime maxima in high cloud amount).

The Arabian Sea, Indian peninsula and the Bay of Bengal are still largely cloud free.

Results for the early May phase indicate that convective activity is a maximum in the southern Bay of Bengal and the eastern Indian Ocean, this is in association with a tropical depression that formed on approximately 5 May. These regions have a strong daytime maximum in high cloud amount (figure A6) over the ocean. In contrast, the southern Indian peninsula exhibits a nighttime maximum in high and total cloud amounts. The Arabian Sea, southern Arabian peninsula, Pakistan and Northern India are regions of minimum cloudiness. As in the previous two periods, the land regions display a nighttime maximum in total cloud cover.

The pre-onset phase depicts four regions of major convective activity (figure A7): northwest Bay of Bengal;  $65^{\circ}$  E and  $2^{\circ}$  N;  $91^{\circ}$  E and  $4^{\circ}$  S; and the southwest tip of the Indian peninsula. Regions of large amounts of total cloud cover (minimum clear) include the Southern Indian Ocean, East Africa, and the Himalayas, though the latter may result from cloud retrieval problems over the high mountains. The Arabian peninsula, Iran, Pakistan and central and northern India are largely cloud free. The day-night difference maps depict interesting diurnal differences of high cloud over the MONEX region. The convective oceanic regions tend to have a daytime maximum in high cloud amount. Similar results were observed in GATE studies (e.g. Cox and Griffith 1979; Ackerman and Cox, 1980). Radiative forcing associated with this typical diurnal variation is likely to be that described by McBride and Gray (1979); during the evening hours, subsidence in the clearer regions results in an adiabatic warming that is required to balance the radiative cooling. Mass balance requires increased upward vertical velocities in the already active convective regions where the radiative cooling is suppressed. The time lags

between the mass convergence and maximum areal extent of high clouds accounts for the daytime maximum. On the other hand, over the continental regions the high clouds tend to have a nighttime maximum. Here the likely mechanism for this observed diurnal variation is a boundary layer effect. During the day the boundary layer is destabilized due to the SW heating of the surface, leading to enhanced convective activity during the late day and early morning, again a phase lag between maximum mass convergence and maximum high cloud is needed to explain the nighttime maximum. An interesting pattern of diurnal variations is observed over the southern tip of India, where inland there is a nighttime maximum (in both high cloud and total cloud amounts), while over the ocean there is a daytime maximum. Another interesting region of diurnal variation in total cloud is over the NW Arabian Peninsula where there is a nighttime maximum in total cloud amount. The observed cloud cover over this region is likely to be either a cloud layer capping the top of the dust layer, or a thin cirrus shield associated with the subtropical jet stream. In either case, SW heating is likely to "burn off" the cloud during the day resulting in a nighttime maximum.

During the onset phase there is a large increase in the areal extent of high clouds which appear further north. The major convective activity is primarily confined to the eastern Arabian Sea and the Bay of Bengal. These regions have a daytime maximum in high clouds while the NE coast of India exhibits a nighttime maximum. Total cloudiness extended further northward during the nighttime hours, and is likely a result of the destabilization of the boundary layer during the day. Only the most northern regions of the Arabian Sea are still largely cloud free, as is the NW section of the region of study. There is a large day-night difference in both total cloud cover and high cloud cover near Ethiopia. The Himalayan region also exhibits large

diurnal fluctuation in total cloudiness, while only a small nighttime maximum in high clouds is observed. This result may reflect the inability to separate snow cover from clouds using a single IR measurement during the night.

Analysis of the post-onset phase (figure A9) depict major regions of convection over the NE Arabian Sea, Northern Bay of Bengal region, as well as a band located near 5°S. This double cloud band structure in convective type clouds has been observed in previous studies of cloud distributions associated with the monsoon (Saha, 1974; Sikka and Gadgil, 1980). The areal extent of the high clouds over the Arabian Sea is considerably smaller than the previous period. With the exception of the Ethiopia and Somalia regions, the arid and semi-arid regions are nearly cloud free. The analysis of the diurnal difference again displays a daytime maximum in high clouds over the ocean, and nighttime maximums over the Indian Subcontinent. Similar differences in continental and oceanic high cloud amounts were observed over the Western Pacific and southeast Asia by Murakami (1983). The actual cellular pattern in the high cloud diurnal difference suggests interactions between continental and oceanic convection. The oceanic convective regions also exhibit a daytime maximum in total cloud cover, as does the Somalia coast.

### A.3 SUMMARY

GOES-1 VISSR and TIROS-N AVHRR data are employed to derive estimates of cloud cover over a region associated with the southwest summer monsoon. Day to day changes in cloud cover for the period May-July 1979 are described using observations of the sun-synchronous TIROS-N satellite. The advancement of the monsoon is clearly seen in a cross-sectional analysis of high cloud amount over four longitude belts. Large scale chronological changes in cloud cover are presented for the Bay of Bengal, Arabian Sea, India and Saudi Arabian

Peninsula. Prior to the onset of the monsoon, total cloudiness over the Bay of Bengal and the Arabian Sea exhibits an approximate 11 day cycle in peak to peak maximum cloud cover. With the establishment of the monsoon a 5-7 day periodicity in the high cloud amount is observed over the Bay of Bengal.

Analysis of the GOES-1 data is presented for six 10 day periods of 1979 (see Table 1). The distribution of clouds are discussed in relation to monsoon activity. Daytime-nighttime differences in high cloud analyses depict diurnal patterns with daytime maximae over the oceanic regions and nighttime maximae over continental regions.

LIST OF APPENDIX FIGURES

Figure A1. Cross-sectional analysis of the areal percentage of high cloud (cloud tops with pressures less than 400 mb) for four longitude belts : 55°E to 65°E (eastern Arabian Sea), 65°E to 75°E (western Arabian Sea), 75°E to 85°E (India) and 85°E to 95°E (Bay of Bengal). Shaded regions depict cases for which the percentage of high cloud is greater than 50%.

Figure A2. Areal coverage of total cloud amount for four geographical regions, as derived from analysis of the TIROS-N AVHRR data.

Figure A3. Areal coverage of high cloud for four geographical regions, as derived from analysis of the TIROS-N AVHRR data.

Figure A4. Spatial distribution of clouds derived from analysis of GOES-1 VISSR data, for the January phase of the 1979 summer monsoon. The panels are a) Daytime high cloud amount; b) Nighttime high cloud amount; c) Daytime total cloud amount; d) Nighttime total cloud amount; e) Day-night difference in clear regions (shaded regions depict regions of nighttime maximae in total cloud cover) f) Day-night difference in high cloud amount (shaded regions depict regions of nighttime maximae in high cloud amount).

Figure A5. Spatial distribution of clouds derived from analysis of GOES-1 VISSR data, for the February phase of the 1979 summer monsoon. The panels are a) Daytime high cloud amount; b) Nighttime high cloud amount; c) Daytime total cloud amount; d) Nighttime total cloud amount; e) Day-night difference in clear regions (shaded regions depict regions of nighttime maximae in total cloud cover) f) Day-night difference in high cloud amount (shaded regions depict regions of nighttime maximae in high cloud amount).

Figure A6. Spatial distribution of clouds derived from analysis of GOES-1 VISSR data, for the Early May phase of the 1979 summer monsoon. The panels are a) Daytime high cloud amount; b) Nighttime high cloud amount; c) Daytime total cloud amount; d) Nighttime total cloud amount; e) Day-night difference in clear regions (shaded regions depict regions of nighttime maximae in total cloud cover) f) Day-night difference in high cloud amount (shaded regions depict regions of nighttime maximae in high cloud amount).

Figure A7. Spatial distribution of clouds derived from analysis of GOES-1 VISSR data, for the Pre-onset phase of the 1979 summer monsoon. The panels are a) Daytime high cloud amount; b) Nighttime high cloud amount; c) Daytime total cloud amount; d) Nighttime total cloud amount; e) Day-night difference in clear regions (shaded regions depict regions of nighttime maximae in total cloud cover) f) Day-night difference in high cloud amount (shaded regions depict regions of nighttime maximae in high cloud amount).

Figure A8. Spatial distribution of clouds derived from analysis of GOES-1 VISSR data, for the Onset phase of the 1979 summer monsoon. The panels are a) Daytime high cloud amount; b) Nighttime high cloud amount; c) Daytime total cloud amount; d) Nighttime total cloud amount; e) Day-night difference in clear regions (shaded regions depict regions of nighttime maximae in total cloud cover) f) Day-night difference in high cloud amount (shaded regions depict regions of nighttime maximae in high cloud amount).

Figure A9. Spatial distribution of clouds derived from analysis of GOES-1 VISSR data, for the Post-onset phase of the 1979 summer monsoon. The panels are a) Daytime high cloud amount; b) Nighttime high cloud amount; c) Daytime total cloud amount; d) Nighttime total cloud amount; e) Day-night difference in clear regions (shaded regions depict regions of nighttime maximae in total cloud cover) f) Day-night difference in high cloud amount (shaded regions depict regions of nighttime maximae in high cloud amount).